Vertically Aligned Silicon Nanowires Synthesised by Metal Assisted Chemical Etching for Photovoltaic Applications

By

Siphelo Ngqoloda

A thesis submitted in fulfilment of the requirements for the degree of Magister Scientiae in the Department of Physics, University of the Western Cape (UWC)

Supervisor	**:**	**Dr F. R. Cummings, UWC**
Co-Supervisors	**:**	**Prof C. J. Arendse, UWC**
	:	**Dr D. E. Motaung, Council for Scientific and Industrial Research (CSIR)**

November 2015

DEDICATION

To my late Father and brother:

Mhatu and Sindile Ngqoloda

UNIVERSITY of the
WESTERN CAPE

ACKNOWLEDGEMENT

I am grateful to the following people and organisation without whose assistance, advice and guidance the completion of this thesis would not be possible

Dr Franscious Cummings (Department of Physics, UWC) for the excellent supervision of this thesis, his guidance, encouragement, friendship and for the many stimulating discussions.

Prof Christopher Arendse (Department of Physics, UWC), who acted as co-supervisor, for his constant encouragement and interest in my progress.

Dr David Motaung (Nano Research Group, CSIR), who also acted as co-supervisor, for his guidance, friendship and many fruitful discussions.

Prof Nico Orce for his motivation, encouragement and showing his belief in me even though he always said I have betrayed him by choosing materials science over nuclear physics as a career, Thanks Sir.

Dr Theo Muller and Dr Gerald Malgas for their motivation and encouragement accompanied by advices and interesting discussions.

UNIVERSITY of the
WESTERN CAPE

The staff of the Physics Department, UWC, for their support, to mention few: Prof R. Lindsay, Prof R. Madjoe, Mrs. A. Adams, Mrs. N. Kenseley, Miss. S. Spannenberg, and Mr. M Paradza for the administration and encouragements.

To my immediate family: my mother and all my siblings, and not to forget my extended families and friends, for their encouragement and support.

My colleagues, friends and fellow MANUS/MATSCI colleagues at UWC for their support and encouragement, Lutendo Phuthu, Sive Mazwi, Anele Tshaka, Sivuyile Xabanisa, Craig Mehl, Bhivek Singh, Rendani Lukhwa, Sino Tanci, Jane Slinger and not forgetting Sfiso Khanyile, Albert Ramashia and Venita Petersen for their advices and assistance with the analysis software during my first year of MSc.

The National Research Foundation (NRF), iThemba Labs, and University of the Western Cape for the financial support during this study. Council for Scientific and Industrial Research for allowing me to use their instruments.

DECLARATION

I declare that

"Vertically Aligned Silicon Nanowires Synthesised by Metal Assisted Chemical Etching for Photovoltaic Applications"

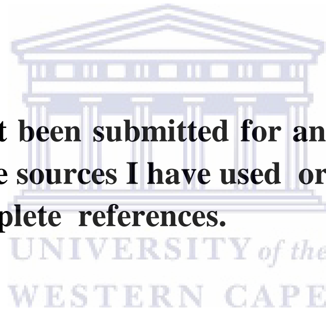

is my own work, that it has not been submitted for any degree or examination in any other university, and that all the sources I have used or quoted have been indicated and acknowledged by means of complete references.

Siphelo Ngqoloda **November 2015**

Signature: …………………………….

KEY WORDS

Vertically Aligned Silicon Nanowires Synthesised by Metal Assisted Chemical Etching for Photovoltaic Applications

Siphelo Ngqoloda

Silicon Nanowires

Silver Nanoparticles

Nanostructures

Antireflective Properties

Photovoltaics

Metal Assisted Chemical Etching

Top Down Approach

Oxidation-Dissolution

Electron Microscopy

Optical Reflectivity

Raman Spectroscopy

Single Crystallinity

Surface Passivation

ABSTRACT

'Vertically Aligned Silicon Nanowires Synthesised by Metal Assisted Chemical Etching for Photovoltaic Applications'

Siphelo Ngqoloda

MSc. Thesis, Department of Physics, University of the Western Cape

UNIVERSITY of the WESTERN CAPE

One-dimensional silicon nanowires (SiNWs) are promising building blocks for solar cells as they provide a controlled, vectorial transport route for photo-generated charge carriers in the device as well as providing anti-reflection for incoming light. Two major approaches are followed to synthesise SiNWs, namely the bottom-up approach during vapour-liquid-solid mechanism which employs chemical vapour deposition techniques. The other method is the top-down approach via metal assisted chemical etching (MaCE). MaCE provides a simple, inexpensive and repeatable process that yields radially and vertically aligned SiNWs in which the structure is easily controlled by changing the etching time or chemical concentrations. During MaCE synthesis, a crystalline silicon (c-Si) substrate covered with metal nanoparticles (catalyst) is etched in a diluted hydrofluoric acid solution containing oxidising agents.

Since the first report on SiNWs synthesised via MaCE, various publications have described the growth during the MaCE process. However lingering questions around the role of the catalyst during formation, dispersion and the eventual diameter of the nanowires remain. In addition, very little information pertaining to the changes in crystallinity and atomic bonding properties of the nanowires post synthesis is known. As such, this study investigates the evolution of vertical SiNWs from deposited silver nanoparticles by means of in-depth electron microscopy analyses. Changes in crystallinity during synthesis of the nanowires are

probed using x-ray diffraction (XRD) and transmission electron microscopy (TEM). Deviations in the optical properties are quantified using optical reflectivity measurements by employing ultraviolet-visible (UV-Vis) spectroscopy, whereas the bonding configurations of the nanowires are probed by Raman and Fourier transforms infrared spectroscopy.

Diameters of 50 – 200 nm vertical SiNWs were obtained from scanning electron micrographs and nanowires lengths linearly increased with etching time duration from about 130 nm after 30 seconds to over 15 µm after 80 minutes. No diameter modulations along nanowires axial direction and rough nanowires apexes were observed for nanowires obtained at longer etching times. These SiNWs remained crystalline as their bulk single crystalline Si wafers but had a thin amorphous layer on the surface, findings confirmed by TEM, XRD and Raman analysis. Nanowires were found to be partially passivated with oxygen with small traces of hydrogen termination, confirmed with infrared absorption studies. Finally, low optical reflection of less than 10% over visible range compared to an average of 30% for bulk Si were measured depicting an antireflective ability required in silicon solar cells.

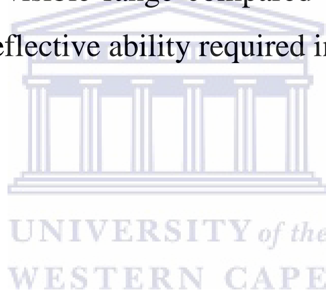

November 2015

LIST OF FIGURES

Vertically Aligned Silicon Nanowires Synthesised by Metal Assisted Chemical Etching for Photovoltaic Applications

Siphelo Ngqoloda

Figure 1.1: World energy consumption showing the dominating use of oil [1.3]..................2

Figure 1.2: Energy consumption in South Africa as in 2012, mostly dominated by coal use and little use of natural gas, BP statistics 2013 [1.3]..3

Figure 1.3: Use of renewable energy by region, showing a fast growth in Europe and East Asia (China) [1.3]. 4

Figure 1.4: Annual solar radiation in South Africa [1.10]. 6

Figure 1.5: World annual solar PV increase in production over the past 30 years (x-axis scale) [1.4]..7

Figure 1.6: Schematic of a semiconductor band structure showing partially full E_V below E_F and partially empty E_C above E_F level. Reproduced as in [1.13 – 1.15].........8

Figure 1.7: Schematic representation of (a) direct and (b) indirect semiconductor materials depicting the valence and conduction band edges [1.15]. 11

Figure 1.8: Schematic illustration of amorphous silicon PV cell depicting the p-i-n junction [1.13]...12

Figure 1.9: Schematic showing the process of VLS mechanism from patterned catalyst to the final SiNWs [1.26]...16

Figure 1.10: In-situ TEM images showing the evolution of the Ge nanowire grown via VLS mechanism from the Au nanoparticle (a) to actual nanowire (f) [1.18]. 18

Figure 1.11: Size selection from deposited Au nanoparticle to a relative SiNWs [1.28].......19

Figure 1.12: Quartz furnace for laser ablation setup with all the important components [1.31]...20

UNIVERSITY of the
WESTERN CAPE

Figure 1.13: TEM micrographs of silicon nanowires synthesised by laser ablation, scale bar 100 nm, [1.30]..21

Figure 1.14: Growth mechanism during laser ablation for silicon nanowires growth [1.30].22

Figure 1.15: Schematic presentation of synthesis during lithography using PS spheres combined with MaCE [1.42]...24

Figure 2.1: Schematic representation of silver nanoparticle formation mechanism [2.12]..35

Figure 2.2: Scanning electron micrograph (SEM) of AgNPs deposited at different times with concentration of 5 mM $AgNO_3$ where images (b) – (d) shows the formation of dendrite structures [2.10]. 36

Figure 2.3: SEM micrographs of AgNPs deposited at different doping levels of Si piece. (a) 1 – 5 Ω·cm; (b). 0.3 – 0.8 Ω·cm and (c) 0.008 – 0.02 Ω·cm. Deposition time was 1 minute using 5 mM $AgNO_3$ concentration and the scale bar is 500 nm [2.20]...37

Figure 2.4: Mechanism formation of SiNWs in two-step synthesis showing how nanowires develop from deposited AgNPs [2.12]..39

Figure 2.5: Cross sectional SEM micrograph of vertical SiNWs synthesised from an aqueous solution of HF/H_2O_2 with an insert showing the top view of the nanowires [2.18]. 40

Figure 2.6: Schematic illustration of SiNWs synthesis steps. 50

Figure 3.1: Schematic representation of scanning electron microscope diagram [3.2]........55

Figure 3.2: Schematic representation for the relation between depth of field, working distance and aperture [3.2]. 57

Figure 3.3: Schematic illustration of different signals produced during electron beam – specimen interaction [3.1]...58

Figure 3.4: Schematic representation of different signals as they originate within the interaction volume [3.1]..59

Figure 3.5: Schematic illustration of the emitted characteristic x-ray with an atom [3.1]. ..61

Figure 3.6: Schematic illustration of TEM column and its important parts [3.4]. 64

UNIVERSITY of the
WESTERN CAPE

Figure 3.7: Schematic illustration of an incident electron beam (I) on an array of atoms separated by *d*, the beam may be diffracted (D and N) or not diffracted (T) [3.1]. 67

Figure 3.8: Schematic representation of diffraction pattern formation in TEM [3.1]. 68

Figure 3.9: Schematic illustration of diffraction pattern formation in positions DD' and EE' or formation of a micrograph in CC' [3.1]. 69

Figure 3.10: Schematic illustration of (a) point lattice and (b) the unit cell [3.5]. 72

Figure 3.11: Schematic of Bragg's interpretation for the interaction of x-rays with atomic planes in a crystal [3.5]. 75

Figure 3.12: Schematic representation of x-ray diffractometer operational principles [3.5]. 76

Figure 3.13: Illustration of the scattering events, Rayleigh, Stokes and anti-Stokes [3.6]. ...78

Figure 3.14: Representation of a ball-and-spring model for diatomic molecule [3.7] 79

Figure 3.15: A typical Raman spectrum of bulk Si illustrating main peaks [3.9] 80

Figure 3.16: First order Raman peak of SiNWs showing a downshift and asymmetric broadening as compared to the bulk Si [3.10]. 81

Figure 3.17: Schematic illustration of Raman spectrometer [3.6] 82

Figure 3.18: Schematic of FTIR spectrometer with Michelson interferometer [3.12]. 85

Figure 3.19: Schematic illustration of transmitted light through a sample [3.12] 87

Figure 3.20: Schematic representation of specular and diffuse reflections [3.13]. 88

Figure 3.21: Light refraction between two mediums of different refractive indices [3.13]...89

Figure 3.22: Schematic illustration of a UV-Vis spectrometer [3.12]. 90

Figure 4.1: Silver nanoparticles deposited at different times using low $AgNO_3$ concentration (5mM). (a) for 15 seconds, (b) for 60 seconds, and (c) for 300 seconds. 95

Figure 4.2: AgNPs obtained from the AgNO3 concentration of 20 mM, deposited from different immersion times. (a) deposited for 15 seconds, (b) 60 seconds, (c) for 300 seconds and (d) is the low magnification of the image in (c). 96

UNIVERSITY of the
WESTERN CAPE

Figure 4.3: AgNPs obtained from the highest silver salt concentration of 50 mM. (a), (b), and (c) from deposition times of 15, 60, and 300 seconds, respectively, (d) and (e) are the lower magnification of dendrite structures. 97

Figure 4.4: Nanoparticles obtained from 30 seconds deposition time from 20 mM $AgNO_3$ concentration (a), lower magnification in (b). 98

Figure 4.5: EDS measurements for AgNPs. EDS spectrum in (a) and (b) is the image showing the position in which the EDS measurements were taken..................98

Figure 4.6: SEM cross section (a) and top view (b) of SiNWs after 30 seconds of etching showing the presence of Ag. 100

Figure 4.7: SiNWs with and without AgNPs in their bottoms, accompanied by EDS measurements. (a), (c) and (e) are the SEM micrograph, the EDS spot and the EDS pattern all depicting the presence of AgNPs, respectively. In (b), (d) and (f) are the results showing the absence of AgNPs. 102

Figure 4.8: SEM micrographs of SiNWs synthesised for different times. (a) and (b) are the cross section views of the nanowires obtained after 3 and 5 minutes with their corresponding top view images (c) and (d), respectively. 103

Figure 4.9: SEM micrographs of longer SiNWs after longer etching time durations. (a) after 15 minutes etching time, and (b) after 30 minutes cross sectional views, with (c) and (d) the corresponding top view images, respectively, with their low magnification as insets. 104

Figure 4.10: SEM cross section micrographs for longer SiNWs obtained after (a) 50 minutes and (b) 80 minutes etching time durations..105

Figure 4.11: Relation between silicon nanowires length and etching time from 30 seconds to 80 minutes, the insert shows the confined points from shorter etching time durations...106

Figure 4. 12: SEM micrographs of rough SiNWs tips, (a) after 30 minutes etching and (b) 60 minutes of etching time duration. 107

Figure 4.13: TEM micrographs for rough nanowires obtained after 60 minutes of etching, low magnification (a) and higher magnification (b). 108

Figure 4.14: SEM micrographs of silicon nanowires synthesised from different oxidant (H_2O_2) concentration. From (a) – (f) are the concentrations 0.1, 0.5, 1.5, 2.5, 3.5 and 5 M. 109

Figure 4.15: Relationship between silicon nanowires length and the oxidant concentration. ... .110

UNIVERSITY of the
WESTERN CAPE

Figure 4.16: Single crystal silicon nanowire with planes along ⟨111⟩ in (a) and SAED pattern with zone axis along [011] direction (b)...112

Figure 4.17: X-ray diffraction patterns for silicon nanowires and bulk Si. At (a) is the intense Si peak and (b) are other low intense peaks depicting a varying intensity from the Si (200) diffraction peak. 113

Figure 4.18: Raman scattering spectra of SiNWs as compared to that of bulk Si. (a) shows a c-Si peak at 520 cm^{-1} for SiNWs and bulk Si and (b) shows an amorphous SiO_x present on the nanowires, sample (iii). 114

Figure 4.19: FTIR spectra of SiNWs together with bulk Si. (a) shows full spectra with intense peaks assigned to the labelled vibrations, (b) shows a deconvolution of the Si-O-Si asymmetric stretching vibration peak. 116

Figure 4.20: EDS results showing varying amount of oxygen with SiNWs. (a) and (b) are the SEM micrographs with EDS spots and (c) and (d) are the corresponding spectra. 118

Figure 4.21: Element mapping of an individual nanowire. (a) is the STEM-HAADF micrograph, (b) silicon map, (c) oxygen map, and (d) is the fluoride map, all showing elementary variation within the nanowire. 119

Figure 4.22: Specular reflection for SiNWs compared to that from bulk silicon over the visible wavelength range...121

Figure 4.23: Diffuse reflection measurements taken for SiNWs synthesised from 15 and 30 minutes etching. 122

UNIVERSITY of the
WESTERN CAPE

TABLE OF CONTENTS

Title Page .... **i**

Dedication .... **ii**

Acknowledgement .... **iii**

Declaration .... **iv**

Key Words .... **v**

Abstract .... **vi**

List of Figures .... **viii**

CHAPTER ONE 1

Introduction 1

1.1 Energy Mix 1

1.2 Renewable Energy 3

1.3 Solar Energy 5

1.4 Photovoltaic Solar Energy 6

1.4.1 Background 6

1.4.2 Basic Principles of Photovoltaics 7

1.4.3 Extrinsic Material 9

1.4.4 Generation and Recombination of Charge 10

1.4.5 Basic Operating Principle of a Traditional Photovoltaic Cell 11

1.5 Generations of Solar Cells 12

1.5.1 First Generation Solar Cells 12

1.5.2 Second Generation Solar Cells 13

1.6 Nanostructures for Photovoltaic Application 14

1.7 Techniques of Silicon Nanowires Synthesis 15

1.7.1 Background 15

1.7.2 Vapour-Liquid-Solid Mechanism 15

1.7.3 Laser Ablation 19

1.7.4 Thermal Evaporation 22

UNIVERSITY of the
WESTERN CAPE

1.7.5 Nanoimprint Lithography 23
1.8 Aims and Outline of Thesis 25
References 28

CHAPTER TWO 31
Metal Assisted Chemical Etching 31
2.1 Introduction 31
2.2 Background of Metal Assisted Chemical Etching 31
2.3 Formation Mechanism of Silver Nanoparticles 33
2.4 Formation Mechanism of Silicon Nanowires 37
2.5 Silicon Nanowires Synthesis Parameters 40
2.6 Preferred Etching Directions 42
2.7 Properties of SiNWs Synthesised via MaCE 43
2.7.1 Structural Properties 44
2.7.2 Raman Scattering 44
2.7.3 Surface Passivation 46
2.7.4 Optical Reflectance 46
2.8 Experimental Procedure 47
2.8.1 Solution Preparation 47
2.8.2 Sample Preparation and Synthesis 49
References 51

CHAPTER THREE 54
Analytical Techniques 54
3.1 Introduction 54
3.2 Scanning Electron Microscopy 54
3.2.1 Introduction 54
3.2.2 Resolution 56
3.2.3 Depth of Field and Working Distance 56
3.2.4 Electron Beam-Specimen Interaction: Signals Produced 57
3.2.5 Detecting Secondary and Backscattering Electrons 59
3.2.6 Characteristic X-ray and Energy Dispersive Spectroscopy 60
3.2.7 Sample Preparation and Data Acquisition 62
3.3 Transmission Electron Microscopy 62

UNIVERSITY of the
WESTERN CAPE

3.3.1 Introduction 62
3.3.2 Electron Beam-Specimen Interaction in Transmission Electron Microscopy 64
3.3.3 Electron Diffraction 65
3.3.4 Electron Diffraction in the Transmission Electron Microscope 67
3.3.5 Structure Factor 70
3.3.6 Sample Preparation and Data Acquisition 71
3.4 X-ray Diffraction 71
3.4.1 Introduction 71
3.4.2 Crystal Structure and Bravais Lattices 72
3.4.3 Bragg's Law of Diffraction by Crystals 74
3.4.4 The X-ray Diffractometer 75
3.4.5 Data Acquisition and Sample Preparation 77
3.5 Raman Spectroscopy 77
3.5.1 Introduction 77
3.5.2 Theory of Raman Spectroscopy 77
3.5.3 Raman Characterisation of Silicon Nanowires 80
3.5.4 Experimental Set-up and Data Acquisition 82
3.6 Fourier Transform Infrared Spectroscopy 83
3.6.1 Introduction 83
3.6.2 Theory of FTIR 83
3.6.3 Experimental Set-up and Data Acquisition 84
3.7 Ultraviolet-Visible Spectroscopy 85
3.7.1 Introduction 85
3.7.2 Theory of UV-Vis Spectroscopy 86
3.7.3 Reflectance 87
3.7.4 Experimental Set-up and Data Acquisition 89
References 91

CHAPTER FOUR 93
Results and Discussions 93
4.1 Introduction 93
4.2 Deposition of Silver Nanoparticles and their Morphology 94
4.3 Synthesis of Vertically Aligned Silicon Nanowires and their Properties 99
4.3.1 Investigation of the Morphology of SiNWs 99

UNIVERSITY of the
WESTERN CAPE

4.3.1.1 Effect of Etching Time on SiNW Formation 99
4.3.1.2 Effect of Oxidant Concentration on SiNW Formation 108
4.3.2 Crystal Structure of MaCE Synthesised SiNWs 111
4.3.3 Surface Passivation of MaCE Synthesised SiNWs 115
4.3.1 Optical Reflectance of MaCE Synthesised SiNWs 120
4.4 Conclusion 123
Reference 125

CHAPTER FIVE 128
Conclusion and Recommendations 128

CHAPTER ONE

Introduction

1.1 Energy Mix

Energy is the main source of life on earth, as it supports human welfare, health, sustainability and socialism. However, energy conversion into feasible forms, such as electrical energy, is currently a highly debated topic, due to its effects on the earth's climate. In particular, electrical energy generated from the burning of fossil fuels (coal, natural gas and oil) results in global warming, which is believed to be the result of carbon dioxide (CO_2) emission into the earth's atmosphere, ultimately resulting in the rise of the earth surface temperature [1.1, 1.2].

Global warming is not the only concern for electricity generated from the combustion of fossil fuels. In the last decade greater energy demand has seen a rapid decline in the globally available reserves. Needless to say, this had a major impact on the ever-growing global economy. Figure 1.1 shows the use of fossil fuels around the world. Since fossil fuels are the result of old material such as plants and animals buried underground millions of years ago, the current trend in high consumption will result in a rapid depletion of available reserves, which will take a very long time to recover. As a result, there is a high competition for fossil fuel use, to the detriment of developing regions such as Africa and the Middle East [1.3].

UNIVERSITY of the
WESTERN CAPE

South Africa is the highest consumer of electricity in Africa even though more than half the population did not have access to electricity 20 years ago. This can largely be attributed to the greater industrial development in South Africa compared to the rest of Africa. As shown in Figure 1.2, the major source of electricity in South Africa is fossil fuels, in particular coal. In the last decade, the high electricity demand in South Africa has seen a sharp annual increase in the electricity price, subsequently leading to an increase in the source of electricity, i.e. coal. The increase in coal price is further fuelled by competition between South Africa and developed countries like China, which imports coal from South Africa. That competition results into South Africa exporting high quality coal and using the remains for the country's

electricity generation, which negatively affects energy consumers in South Africa when it comes to buying electricity [1.1 – 1.3].

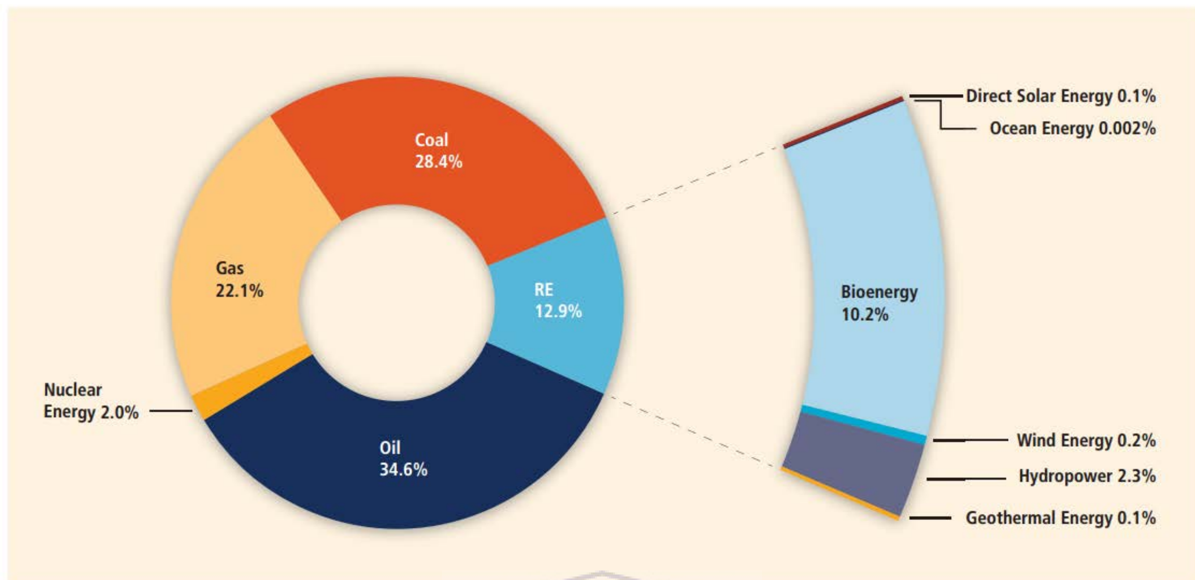

Figure 1.1: World energy consumption showing the dominating use of oil [1.3].

UNIVERSITY of the
WESTERN CAPE

Based on the rising issue of global warming and the depletion of current energy resources, there exists a global effort in focusing on possible alternative energy sources. Answers lie in the use of renewable sources, which can withstand their use over a long term basis without depletion.

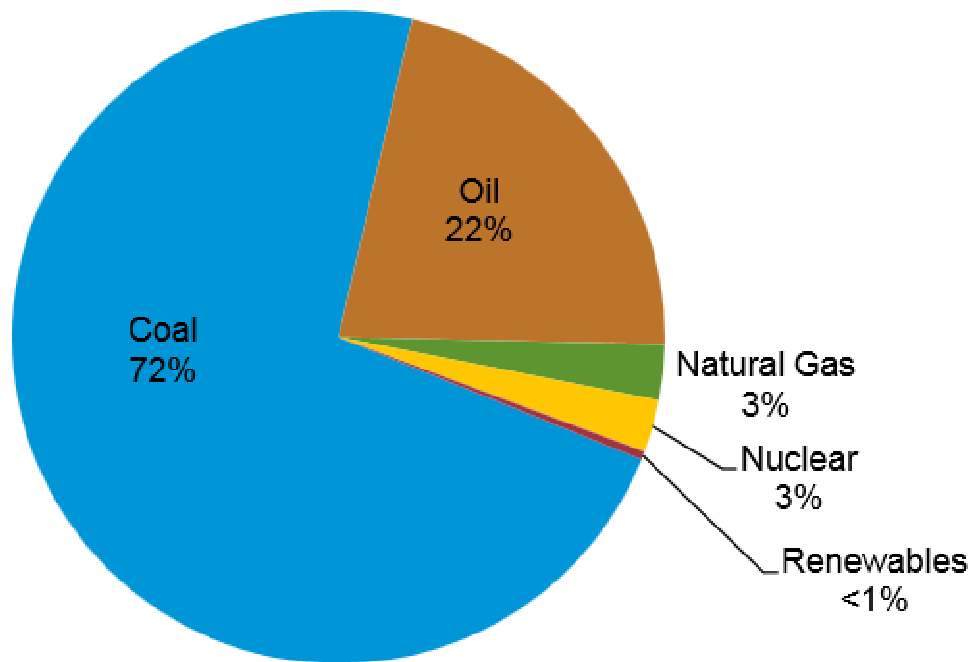

Figure 1.2: Energy consumption in South Africa as in 2012, mostly dominated by coal use and little use of natural gas, BP statistics 2013 [1.3].

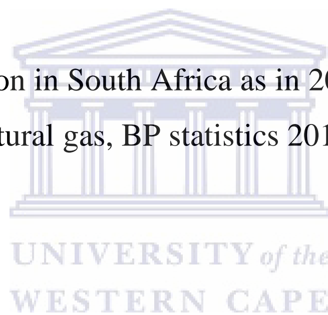
UNIVERSITY of the
WESTERN CAPE

1.2 Renewable Energy

As can be seen in Figure 1.1 only about thirteen percent (13%) of the global energy consumption results from the use of renewable energy. These include: biomass or bioenergy, geothermal energy, wind energy, hydropower, solar energy and oceanic energy. There has been a slight increase over the past 20 years in the application of renewable energy technology, especially in developed countries with larger energy needs. These regions include North America, Europe and East Asia (China specifically) as shown in Figure 1.3. Africa and The Middle East are almost insignificant in Figure 1.3, largely as a result of a lack of funds required to implement such technologies. The small percentage of renewable energy uses in these countries predominantly stems from the inefficient use of bio-energy for cooking purposes. Renewable energy beneficiation varies from region to region. Depending on the region, the available energy conversion options are limited to technologies that can be implemented in that region, depending on the stability of the country's economy. This largely

explains the rapid growth of renewable energy use in developed countries compared to the poor application in developing countries [1.1, 1.2, 1.4].

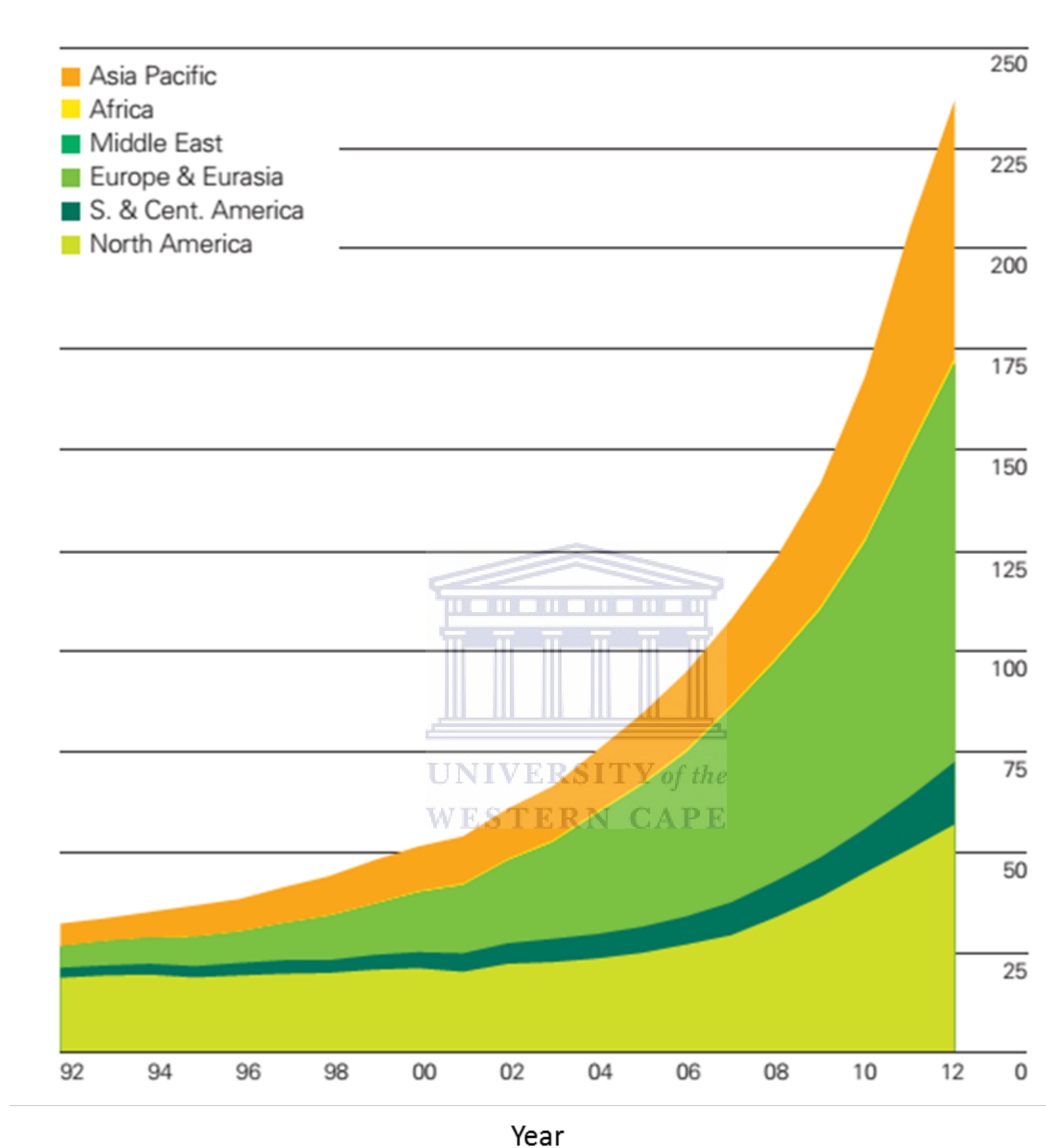

UNIVERSITY of the
WESTERN CAPE

Figure 1.3: Use of renewable energy by region, showing a fast growth in Europe and East Asia (China) [1.3].

1.3 Solar Energy

The sun provides about ten thousand times the required energy on earth, through direct use of heat and light. Most renewable energy systems, including hydropower, bio-energy and wind energy, result from radiant energy provided by the sun. Current global research and development aims at directly and indirectly convert solar energy into electricity and heat. As shown in Figure 1.4, for South Africa solar energy is a good candidate as a renewable energy source, as the country receives favourable annual solar radiation per area. These flux levels are greater than most countries in Europe, Asia and parts of Northern America, which currently employ large scale solar energy technologies [1.4 - 1.10].

Solar energy is directly converted into electricity by using photovoltaic (PV) technology. Indirect methods employ technology known as concentrating solar power (CSP) conversion. This method focuses rays of sunlight onto one point and delivers that into a generator to generate electricity. Both methods can be used to produce electricity and heat. CSP is further subdivided into three different ways of production, namely parabolic trough, central receiver and parabolic dish in order of increasing conversion efficiency and cost. CSP system is more costly than PV technology thus for developing countries like South Africa it is most effective to look at PV system for solar energy [1.2, 1.4, 1.9].

UNIVERSITY of the
WESTERN CAPE

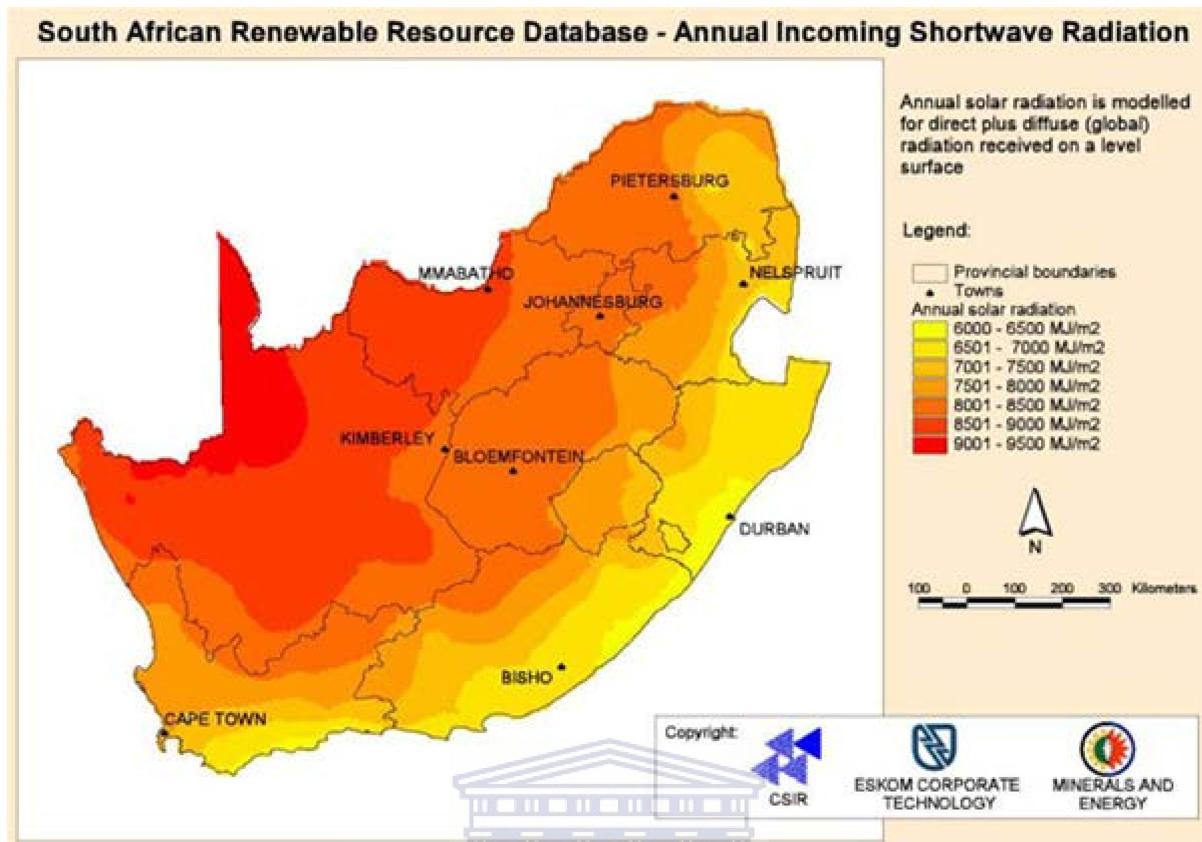

Figure 1.4: Annual solar radiation in South Africa [1.10].

UNIVERSITY of the
WESTERN CAPE

1.4 Photovoltaic Solar Energy

1.4.1 Background

The PV effect dates back to 1839, first recognised by E. Becquerel. He noticed that when light or photons hit a flat metal plate their energy is converted into electrical energy. It was not until almost a century later that this theory was put into real physics application when researchers manufactured the first crystalline silicon solar cell, with an efficiency of 5%, in the 1950s. PV converted electrical energy has increased since, as shown by Figure 1.5. This increase is due to the development of more efficient and inexpensive renewable energy technologies [1.4, 1.5, 1.11 - 1.13].

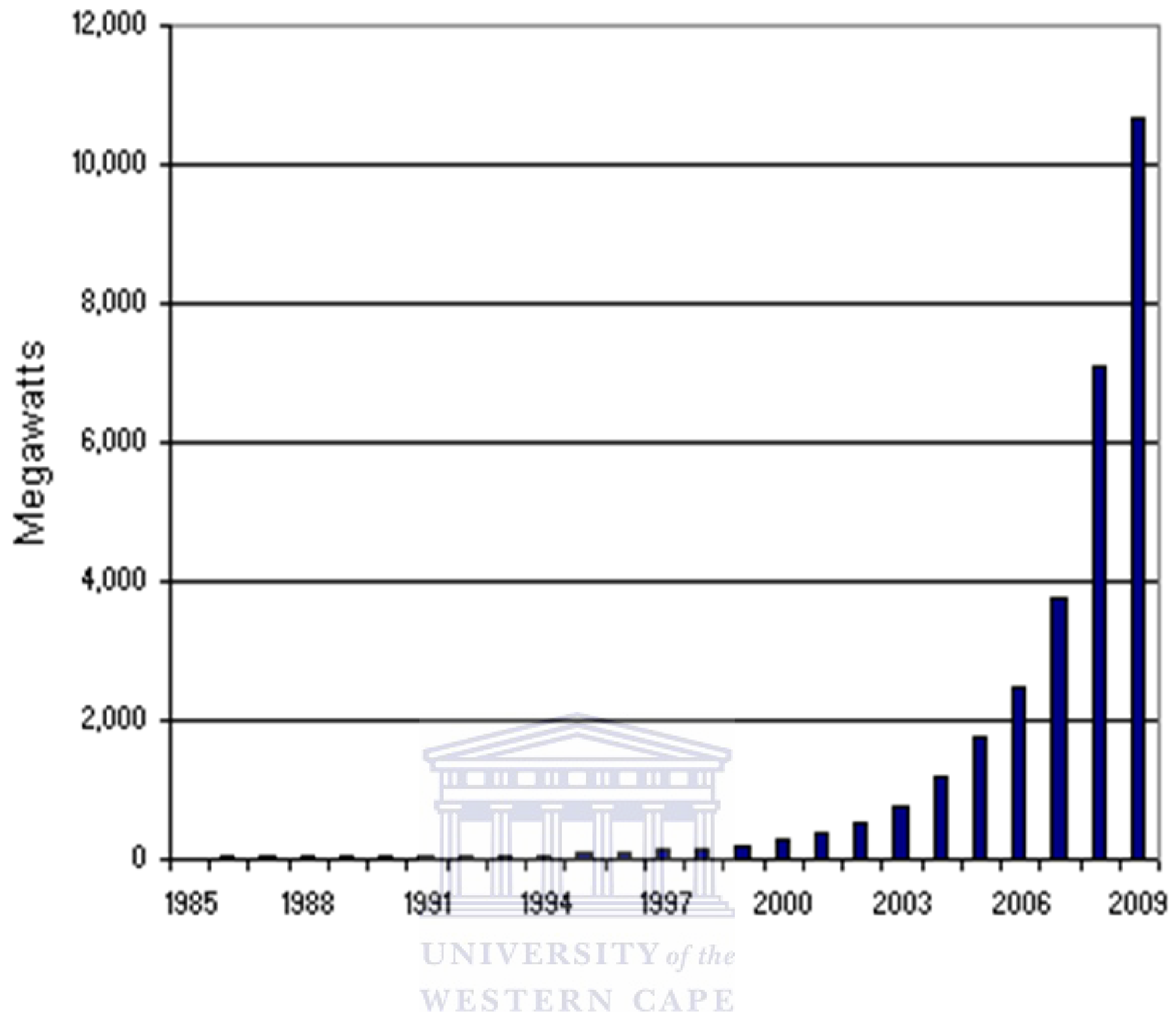

UNIVERSITY of the
WESTERN CAPE

Figure 1.5: World annual solar PV increase in production over the past 30 years (x-axis scale) [1.4].

1.4.2 Basic Principles of Photovoltaics

Photovoltaic technology is based on semiconductor materials. These materials differ from conductors and insulators by a special characteristic called the band-gap of the material. Conductors or metals have overlapping band-gaps while insulators (and glasses) have a wide gap, which is roughly more than two electron volt (2 eV), a unit of energy preferred for low energy calculations, where 1 eV is equivalent to 1.602×10^{-19} J. In between these two materials lies an important material in the field of PVs, namely semiconductors, which have a band-gap ranging from 0.5 to 3 eV. The band-gap is an important property as it determines the functionality of a solar cell [1.4, 1.11, 1.12].

Atoms contain electron shells (or orbitals) positioned at increasing energy levels from the atomic nucleus. In the absence of external excitation factors, only two electrons are allowed in any level, in agreement with the Pauli Exclusion Principle. These electrons have different "spin" (self-angular momentum), where one is facing down and the other facing up [1.4]. Energy levels in a material combines to form energy bands. There are two important energy bands in a semiconductor material, with one energy band being the highest filled valence band (E_V) at very low temperatures and the other the partially filled conduction band (E_C), shown in Figure 1.6. The gap between these bands is the band-gap (E_G) and is one of the main properties that determine if the incident photon will be absorbed or not. The absorption of an incident photon is possible only if the energy of that photon is greater than or equal to the energy of the semiconductor band-gap i.e. $h\nu \geq E_G$, where $h\nu$ is the incoming photon energy, h is the Plank's constant given by a numerical value of 6.64×10^{-34}J. s and ν is the frequency of the photon [1.4, 1.13, 1.14].

If a photon of enough energy (energy greater than E_G) hit the valence band, one or more electrons will be excited to the conduction band in a semiconductor material. This happens because the photon energy is transferred to the electron giving it potential and kinetic energy for it to be excited to the conduction band. One other requirement is that the energy of the incoming photon has to overcome the work function of the material. But once again the electrons in the outer shell are not tightly bounded to the nucleus of the atom especially for semiconductor material, and the fact that an electron will be excited or not is governed by the energy of the incident photon and the band gap of the semiconductor [1.14].

UNIVERSITY of the
WESTERN CAPE

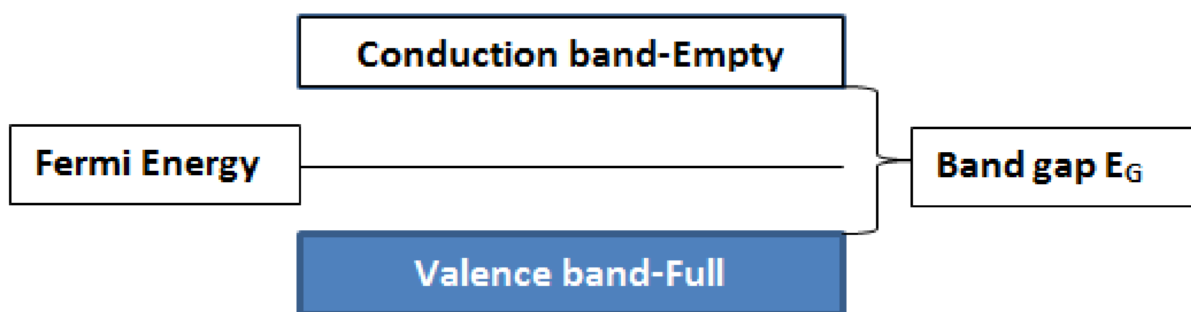

Figure 1.6: Schematic of a semiconductor band structure showing partially full E_V below E_F and partially empty E_C above E_F level. Reproduced as in [1.13 – 1.15].

The excited electron leaves behind a positively charged hole in the valence band. Once the electron is excited, an electron-hole pair is formed. When this occurs, the material is said to be mobile, during which time the excited electron is free and can conduct heat or electricity. In the valence band the hole can also be filled with another electron, resulting in that process also leading to conductivity. This shows that a rise in temperature, or if more photons are absorbed by a semiconductor material, more electrons will be excited to $E_{C,}$ resulting in high conductivity.

For intrinsic semiconducting material every excited electron will be substituted by a hole in the valence band. That means for intrinsic materials there are an equal number of electrons in the E_C as the number of holes in the E_V. These electrons and holes are therefore responsible for the flow of current in a semiconductor material [1.13, 1.14]. In semiconductor materials the band-gap is controlled by Fermi energy level, E_F, usually situated in the middle of the band-gap for intrinsic material as shown in Figure 1.6. The Fermi level can change positions depending on whether the structure of the material is changed, e.g. during doping of the material [1.15].

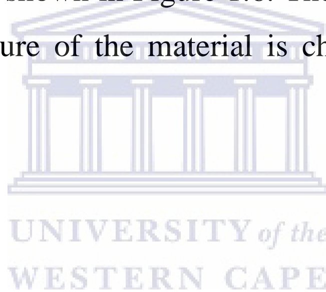
UNIVERSITY of the
WESTERN CAPE

1.4.3 Extrinsic Material

Conductivity in intrinsic semiconductor material can only be increased by reducing the band gap of the material or increasing the temperature of the material. However, it is not easy to change the band-gap, whereas high temperatures can damage the material. The alternative is to introduce impurities into the material via the process known as doping. Si for example has four valence electrons, which are there for bonding purposes, but a foreign atom of five valence electrons or three valence electrons can be substituted in the place of one Si atom. This process of doping is known to increase conductivity dramatically. For example, substitution of one boron atom, which has three valence electrons into pure Si of 10^5 atoms, increases the conductivity of the material by about 10^3 times at room temperature [1.15].

By doping silicon material with an atom of five valence electrons (pentavalent), e.g. P or As, four electrons are used for bonding, whereas the extra electron takes part in conduction. This type of impurity is known as a donor atom as it gives the material an extra electron; these types of semiconductors are called n-type. At low temperatures the material behaves as an intrinsic material, but as the temperature is increased, the less bounded electron is stripped off

the atom, leaving it positively ionised. This process is energetically presented by a donor state, which lies below the E_C and above the intrinsic Fermi level. For these n-type materials the Fermi level readjusts and appears in-between the E_C and donor state. At room temperature electrons will easily be excited to the E_C from the donor states. As such for n-type materials, electrons are the majority charge carriers, which is an important factor for conduction [1.15].

When an atom of three valence electrons (trivalent), such as B or Al, is used to substitute a Si atom, an extra hole is donated to the material. This type of impurity atom is called an acceptor because it takes an electron from the Si material; the material is said to be p-type. The acceptor state lies just above the valence band and the Fermi level moves down and lies between the acceptor level and the valence band. This is due to ionisation of the acceptor atom which has a slightly higher energy than the highest state of the E_V. In a p-type material there are more holes in the E_V than electrons in the E_C and these holes are the majority charge carriers responsible for conduction [1.13 – 1.15].

1.4.4 Generation and Recombination of Charge

As already discussed, when a photon of sufficient energy is incident on a semiconductor material, an electron is excited from E_V to E_C resulting in electron-hole pairs. In addition, an electron can be promoted to some energy state within the E_G leaving a hole in the E_V, or an electron can be generated by promotion from a donor state within the E_G to E_C. These processes are usually due to the absorption of the photon and are hence called charge generation. The reverse is known as recombination, which can destroy the generated electron-hole pair, an electron or a created hole. Recombination results in a release of energy as a photon (radiative recombination), energy can be given up as heat via phonon (non-radiative recombination), or the energy might be transferred to the kinetic energy of another electron (Auger recombination) [1.13].

Semiconductors are classified into direct and indirect band-gap materials. In a direct band-gap material such as GaAs, the valence band maximum and conduction band minimum coincides at the same wave vector, **k**, as shown in Figure 1.7 (a). Subsequently, based on conservation of momentum, absorption of a photon directly results in the creation of an electron-hole pair. In an indirect band gap material such as c-Si, these energy levels do not coincide at **k** = 0, implying that an extra phonon must be added for both energy and

UNIVERSITY of the WESTERN CAPE

momentum to be conserved, as shown in Figure 1.7 (b). Due to this process, absorption of light in an indirect band gap material is very low and thus leaves any potential solar cell inefficient [1.15].

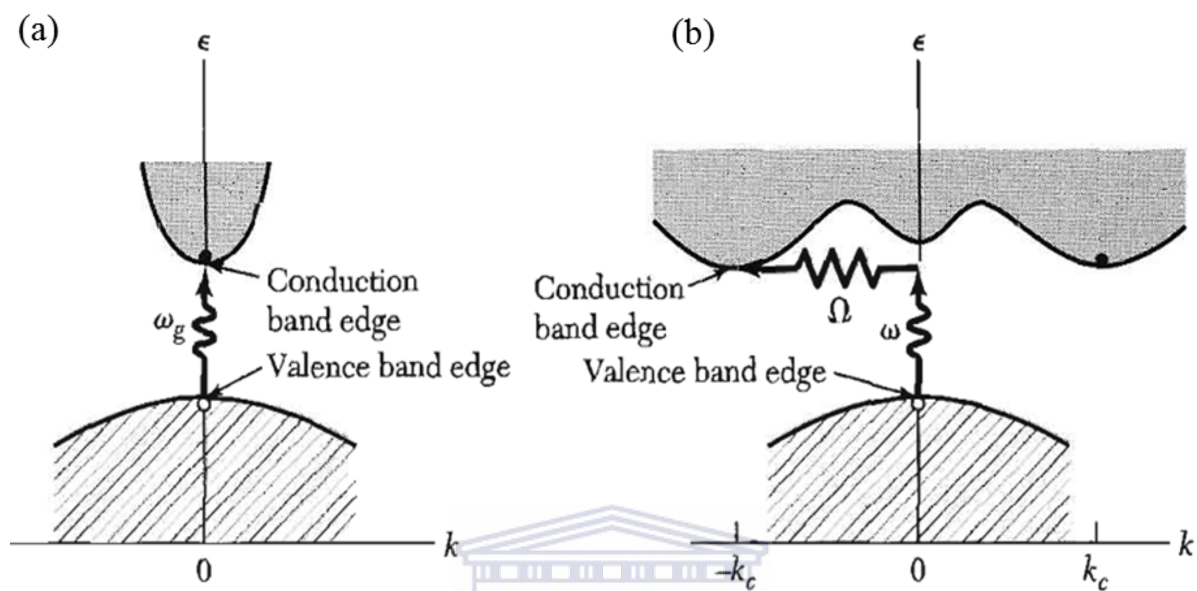

Figure 1.7: Schematic representation of (a) direct and (b) indirect semiconductor materials depicting the valence and conduction band edges [1.15].

UNIVERSITY of the
WESTERN CAPE

1.4.5 Basic Operating Principle of a Traditional Photovoltaic Cell

Traditional thin film PV cells, such as that of a-Si shown in Figure 1.8, employ a p-i-n (p-type layer – intrinsic layer – n-type layer) structure called a diode to convert radiant energy to electrical energy. When an incident photon of enough energy hits the device, it will be absorbed by the intrinsic layer, subsequently generating an electron-hole pair. This leads to the creation of a built-in electric field in the intrinsic layer, which separates these electron-hole pairs; this process is known as charge separation. During charge separation electrons move towards the n-type layer and the holes to the p-type layer. Metal contacts are there for charge collection and the transparent conductive oxide (TCO) layers for better light absorption [1.13].

The thickness of the intrinsic layer requires some optimisation as to maximise the current generation. However, more defects on thicker layers reduce the electric field needed to separate the charges. Even though enough light is absorbed by the thicker intrinsic layer there are drawbacks. Another important requirement is during the absorption of light which is the reason the TCO has to be textured to enhance the absorption [1.13].

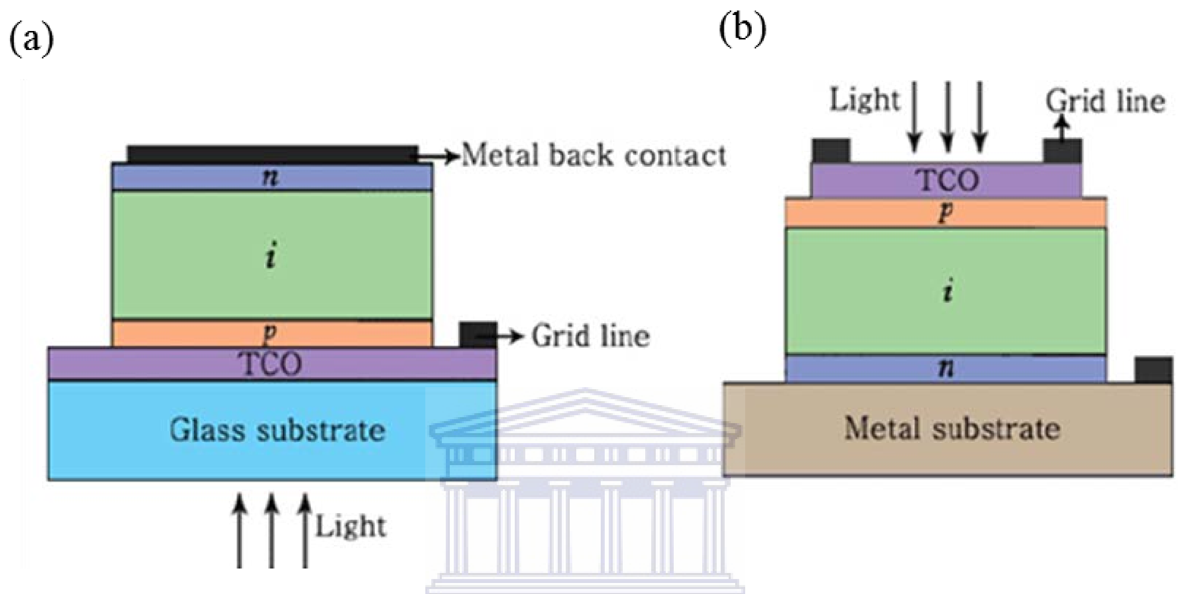

UNIVERSITY of the
WESTERN CAPE

Figure 1.8: Schematic illustration of amorphous silicon PV cell depicting the p-i-n junction [1.13].

1.5 Generations of Solar Cells

1.5.1 First Generation Solar Cells

In Chapter 1.4.1 it was mentioned that the first manufactured solar cell was based on single-crystalline silicon (c-Si), with moderate efficiency. Significant strides have since been made in increasing the efficiency of these wafer based c-Si devices, with record laboratory devices of 25% efficiency recorded in 2008 by M. Green [1.16]. For commercial devices, record efficiency of 20% was measured by the National Renewable Energy Laboratory (NREL) under standard test condition of AM1.5 illumination (1000 W m^{-2}) [1.5]. These devices are referred to as first generation solar cells. A major disadvantage of c-Si solar cells, either mono- or poly-crystalline silicon, is the very high costs associated with producing high

quality wafers needed for device manufacturing. One of the requirements for any photovoltaic technology is to absorb a wide range of solar spectrum (from ultraviolet to near infrared) for charge generation and to have minimum recombination of these charges [1.17]. For this to be achieved the solar cell requires a very thick c-Si material and that comes at high costs. Because of the costs, researchers are still looking at their reduction and striving to maintain or enhance the efficiency of silicon based solar cells.

1.5.2 Second Generation Solar Cells

Second generation solar cells contain amorphous silicon (a-Si) as the active material. These cells are based on thin film technology, aimed at reducing the thickness of the photo-active material used within the device. These thin layers can be deposited on top of less expensive substrates, such as glass or polymers at thicknesses varying from 200 to 300 nm, compared to 200 μm for c-Si [1.11, 1.18]. a-Si also has a wider band gap of 1.7 eV compared to 1.1 eV of c-Si, which allows it to absorb light more strongly in the visible range than it does in the infrared. The efficiency of a-Si based solar cells can be enhanced by combining this material with microcrystalline Si which absorbs light more effectively in the infrared region due to its narrow bandgap of 1.1 eV [1.5].

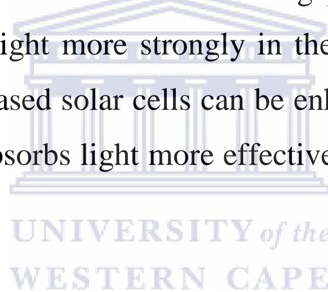
UNIVERSITY of the
WESTERN CAPE

Energy conversion efficiencies of about 12% have been achieved in the laboratory for single junction a-Si based devices, however the efficiency drops drastically when exposed to sunlight to approximately 5%. The low efficiencies were also attributed to the loss of charge carriers through recombination and non-radiative recombination processes. The introduction of multi-junction a-Si and passivating the surface dangling Si bonds with hydrogen to produce more stable hydrogenated amorphous silicon (a-Si:H) thin films, have seen an improvement in the reported efficiencies of these device, with stable efficiencies of about 8 to 9% achieved [1.5, 1.11].

Silicon is not the only semiconductor used in thin film solar cells. Other technologies include cadmium telluride (CdTe), copper indium diselenide (CIS), copper indium gallium diselenide (CIGS) thin films. These technologies have their own drawbacks in terms of efficiencies, in addition to being more expensive due to their rarity, e.g. indium and toxicity, e.g. cadmium. The advent of nanoscience and technology has sparked new interest in second generation thin film solar cells. Silicon has been researched for so long and its properties are well

understood. As such, nanostructured silicon with improved light absorption, charge transport and photo-stability are very attractive options for improved efficiencies and reduced costs for silicon based solar cells [1.5, 1.11].

1.6 Nanostructures for Photovoltaic Application

High cost and inefficiency in conventional solar cells (c-Si) has emerged as a major problem for photovoltaic technology and so great effort of research have been dedicated into solving these issues. Researchers are now looking into nanostructured material as an alternative which can be combined with second generation solar cell (thin film based) or used independently. These nanostructures include three-dimensional (3-D) nanocomposites, 2-D quantum wells, 1-D nanotubes (NTs), nanorods (NRs), nanopillers (NPs) and nanowires (NWs), and lastly 0-D quantum dots and nanoparticles [1.11]. Elongated, one-dimensional nanostructures (NTs, NRs, NP, and NWs) can offer unique advantages such as good absorption of light and high charge separation due to their high surface areas. In particular, 1-D semiconductor (silicon or germanium) nanowires with a direct light path along the wire axis and high aspect ratios for good light absorption are appealing for application in PVs [1.18, 1.19].

UNIVERSITY of the
WESTERN CAPE

Intense research over the past decade have focused on the synthesis and properties of 1-D silicon nanowires (SiNWs), owing to the abundance of silicon on earth compared to germanium and also taking advantage of known properties of bulk silicon [1.19]. SiNWs have proved to have a high aspect ratio (AR) compared to other 1-D elongated structures (NTs, NRs, etc.) with ARs of 5:1 and more reported. These nanomaterials have diameters ranging from 1 – 100 nm and have lengths up to tens of microns [1.18]. SiNWs as PV material offers potential advantages over primary based c-Si wafers and thin film technology due to the optical and electrical properties with new charge separation mechanisms leading to reduced cost [1.20]. These nanowires at the moment cannot offer higher efficiencies above recorded values for conventional solar cells but can reduce the material required to reach those numbers [1.20].

1.7 Techniques of Silicon Nanowires Synthesis

1.7.1 Background

Research based on SiNWs, which were regarded as silicon whiskers and later called silicon wires, started around 1957 based on a report by Treuting and Arnold, which is commonly regarded as the first publication on these structures [1.21]. A few years later (1964), Wagner and Ellis [1.22] developed the now famous technique of silicon wire synthesis, known as the vapour-liquid-solid (VLS) mechanism based on chemical vapour deposition (CVD). After the Wagner and Ellis report, very few research publications had been seen for silicon nanowires. It was only during the 1990's where the research started building up again, fuelled by interest in microelectronics based on silicon nanostructures [1.21].

As research on silicon nanowires have increased rapidly over the past 15 years, quite a number of synthesis methods have also been developed throughout this period. There are two main routes to fabricate, grow or synthesise SiNWs; these are bottom-up and top-down approaches. Bottom-up methods include VLS techniques, laser ablation and thermal evaporation [1.23]. On the other hand top-down methods includes patterned lithography techniques which are combined with reactive ion etching or metal assisted chemical etching (MaCE), however MaCE can be used by itself to synthesise silicon nanowires [1.24]. This section will look at brief descriptions of VLS, laser ablation, thermal evaporation and lithography techniques. Chapter 2 will give a detailed overview of the MaCE mechanism.

UNIVERSITY of the WESTERN CAPE

1.7.2 Vapour-Liquid-Solid Mechanism

VLS is a one-dimensional (1-D) nanostructure growth mechanism that is assisted by a thin layer of noble metal catalyst during CVD synthesis. The mechanism can be used to produce semiconductor structures and nanostructures like wires, whiskers, rods and nanowires. During VLS growth, a metal catalyst such as Au, Pt, Ag, Ni, Pd or Cu [1.18, 1.22], is deposited on a Si wafer; the metal catalyst maybe patterned or deposited as a continuous film on the substrate surface.

Figure 1.9 shows a schematic representation of the VLS method when using Au as a catalyst. As shown in the figure, when the substrate temperature exceeds the melting point of the catalyst during CVD, the catalyst forms liquid droplets. This temperature is also referred to as eutectic temperature – for Au this is approximately 364 °C [1.25]. An eutectic alloy of Au-Si is formed during the melting at the Au/Si interface, which is the preferred region for nucleation and nanowire growth.

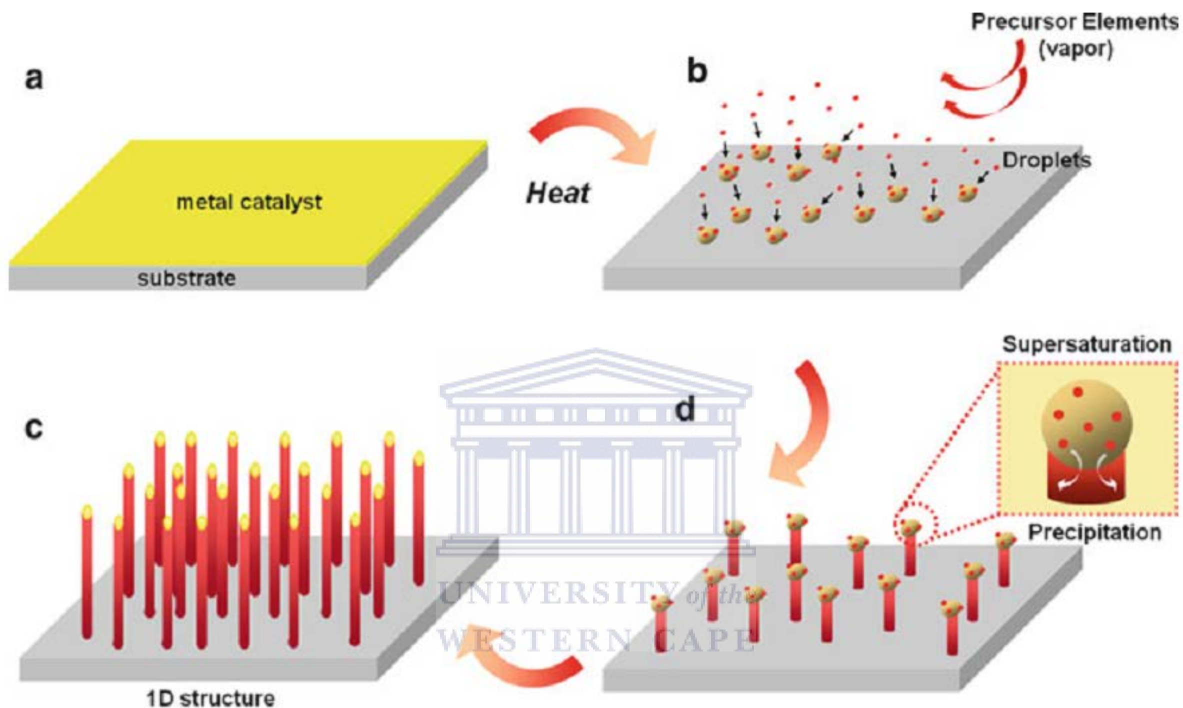

UNIVERSITY of the
WESTERN CAPE

Figure 1.9: Schematic showing the process of VLS mechanism from patterned catalyst to the final SiNWs [1.26].

Wagner and Ellis [1.22] reported that the Au particle coated Si wafer was heated at 950 °C to form the Au-Si alloy droplets. Kuo *et al.* [1.25] also reported that silicon nanowires could not be produced at temperatures below 700 °C without the use of an anodic aluminium oxide (AAO) template which helps produce SiNWs at lower temperatures but above the eutectic temperature of 360 °C. These results imply that the Au-Si alloy droplet forms at temperatures between 700 and 1000 °C depending on the instrumentation used.

The Au-Si alloy liquefies during heating and that enables the absorption of the precursor elements (silicon source) such as silane (SiH_4) or silicon tetrachloride ($SiCl_4$) [1.21, 1.22,

1.25]. The precursor vapours are conveyed to the Au particle containing Si substrate using inert carrier gases like Ar, He or H_2, mostly combined with other reactant gases along the way which can be for p- and n-type doping purposes [1.27]. Upon further heating the Au-Si alloy become supersaturated as shown in Figure 1.9 (d), absorbing the vapour precursor of silicon and during that phase the nucleation begins, which is also the beginning of silicon nanowire growth.

The growth proceeds as long as the deposition or the flow of vapour is in process. As can be seen in Figure 1.9, with more SiH_4 being absorbed by the Au-Si alloy, droplets supersaturate and precipitate, resulting in the wire growth. Au nanoparticles are usually located at the nanowire tips, which is significant of the VLS growth mechanism [1.27]. VLS mechanism is hence called as such, because it involves the vapour carrying solid components, liquid catalyst alloy and the final precipitated silicon nanowires, in solid state, with the initial metal catalyst diameter determining the final nanowire diameter [1.26].

Shown in Figure 1.10 are the transmission electron microscopy (TEM) micrographs of the in-situ growth of a Ge nanowire, starting from the Au nanoparticle in Figure 1.10 (a), to a final nanowire Figure 1.10 (f). Figure 1.10 (f) shows the final nanowire, which has a smaller diameter than the Au-Ge alloy [1.18]. Cui *et al*. [1.28] reported the growth of SiNWs using the VLS where they obtained nanowires with diameters slightly greater than the Au nanocluster diameter [1.28]. Based on their study the starting nanoclusters were averaging at 5 nm; 10 nm; 20 nm and 30 nm, whereas the nanowires were averaging at diameters of 6.46; 12.36; 20.6, and 31.16 nm, respectively [1.28]. Form these results they supported their observations with the fact that the wires were grown from the Au-Si alloy which forms before the nucleation or growth of the nanowires. They also added the contribution of thickness resulting from post growth oxidation through air which can make up few nanometres of thickness. These findings were further substantiated by Wu and Yang [1.29] who found that the alloying process results in nanowires with larger diameters than their starting nanoclusters. These reports show that by controlling the nanoparticle diameter, the nanowires diameter can be controlled as well, as shown in Figure 1.11. With these smaller diameters of nanoparticles (5 nm) resulting into smaller nanowires it shows that the properties of SiNWs can be tuned [1.28]. Silicon nanowires grown via VLS remain single crystalline in their cores, but their surface is usually covered with an amorphous SiO_2 layer that can be about 1-3 nm thick depending on the wire's diameter [1.28].

UNIVERSITY of the
WESTERN CAPE

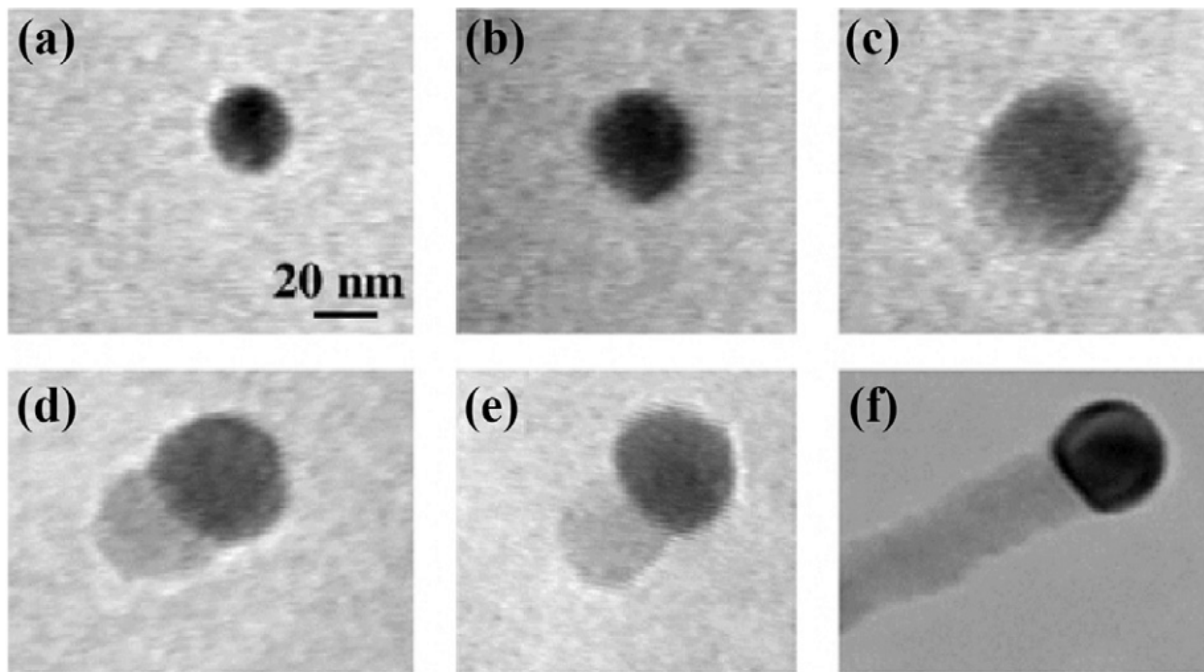

Figure 1.10: In-situ TEM images showing the evolution of the Ge nanowire grown via VLS mechanism from the Au nanoparticle (a) to actual nanowire (f) [1.18].

UNIVERSITY of the
WESTERN CAPE

The preferred growth direction of nanowires via VLS depends mainly on the diameter of the nanowires. In the first report by Wagner and Ellis, using a Si (111) substrate, the whiskers growth direction was found along$\langle 111 \rangle$. More recent results observed that nanowires of smaller diameters (6.7 nm) grew along $\langle 110 \rangle$ and larger nanowires (20.6 nm) grew along $\langle 111 \rangle$ directions [1.28]. These observations were further supported by Zhong *et al.* in [1.27, *pp.* 180 - 182] who stipulated that for diameters of 3-10 nm, 95% of the SiNWs were found to grow along the $\langle 110 \rangle$ direction; for diameters of 10-20 nm, 61% of the SiNWs grew along the $\langle 112 \rangle$ direction; and for diameters from 20-30 nm, 64% of the SiNWs grew along the $\langle 111 \rangle$ direction.

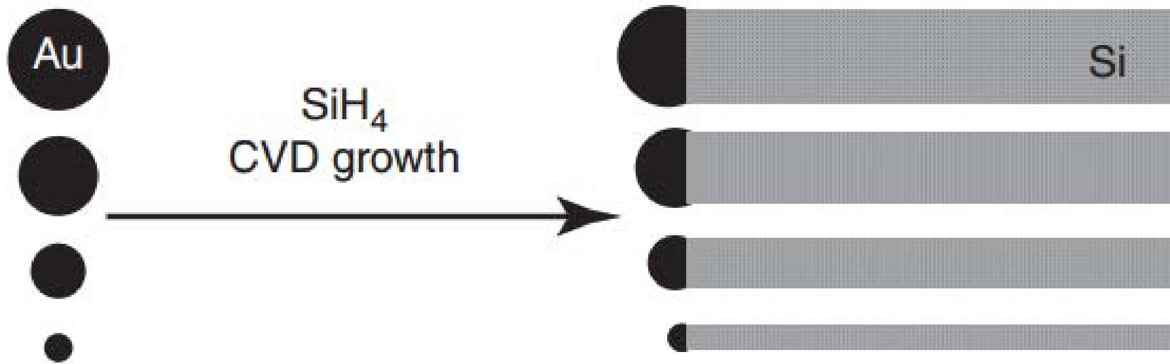

Figure 1.11: Size selection from deposited Au nanoparticle to a relative SiNWs [1.28].

These results show a clear indication for the preferred growth along the ⟨110⟩ direction in smaller nanowires and along the ⟨111⟩ direction in larger SiNWs. These observations are believed to be due to the competition between the liquid catalyst alloys Au-Si/solid silicon nanowire interface energies and the nanowire surface energy [1.27]. The silicon nanowires grown via VLS appear to be disordered in terms of morphology unless expensive patterning for catalyst deposition is used, and might have low surface-to-volume ratios. The control over growth direction depends entirely on the wire's diameter which appears as a drawback for the VLS mechanism [1.28]. To reduce the oxidation and obtaining very thin silicon nanowires, VLS should be operated at very low pressure chemical vapour deposition systems [1.25]. Despite the use of very low pressure and high temperature CVD systems, that makes this technique rather expensive, the nanowires grown via this route show good properties as a result of the fact that the wires can be thinned down to about 2 nm in diameter.

UNIVERSITY of the
WESTERN CAPE

1.7.3 Laser Ablation

Apart from the VLS mechanism via CVD, other methods like laser ablation, can also be used to produce semiconductor nanowires. Morales and Lieber [1.30] reported on laser ablation for the growth of semiconductor nanowires by combining laser ablation with the VLS mechanism. Laser ablation can be used for the synthesis of SiNWs as small as 3 nm in diameter [1.30] and as thick as 50 nm [1.31], depending on the components of the target as will be explained later.

As the name suggests, the method involves a laser of certain energy being focused on target consisting of silicon (or any other semiconductor interested in) and a desired metal catalyst, which in most cases is found to be Fe. The target is usually in powder form composing of 99% Si and 1% Fe. It is found that the percentage composition of Si and catalyst determines the diameter of the nanowires, in conjunction with the temperature of the furnace [1.31, 1.32]. A typical experimental setup is presented in Figure 1.12.

As shown in the figure, when the Si-Fe target is ablated, a dense, hot vapour plume of Si and Fe species is formed. The hot vapour condenses into Si-Fe small clusters, which cool as they collide with the buffer gas. The Si-Fe nanoclusters are kept at liquid state by controlling the temperature of the furnace. The operating temperature of the tube is usually maintained at 1200 °C in which the target should also reach this temperature. The nanocluster liquid supersaturates into Si and the growth of the nanowire begins and progresses as long as the nanocluster is in liquid state and the silicon reactant is still available. In the presence of a carrier gas (Ar) the nanowires would pass the hot zone of the furnace, coming close to the cold zone and then stop growing and solidifies [1.21, 1.30].

UNIVERSITY of the
WESTERN CAPE

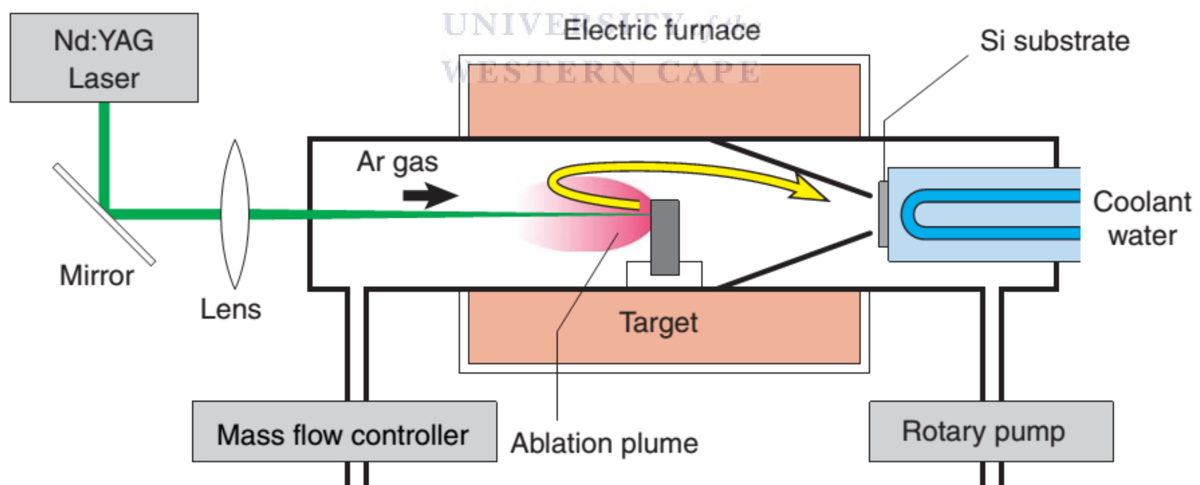

Figure 1.12: Quartz furnace for laser ablation setup with all the important components [1.31].

Due to the presence of the carrier gas (Ar), SiNWs can be deposited directly onto a Si substrate placed at the end of the quartz furnace as shown in Figure 1.12 [1.31]. Morales and Lieber showed that the nanowires grown via laser ablation had a Si crystal diameter of 7.8 ±

0.6 nm covered with a layer of amorphous SiO_x (x = 1 to 2) that is approximately 10 nm; shown in Figure 1.13. They suggested that the amorphous was SiO_2 and attributed to the residual oxygen found in the chamber. Other groups also reported that SiNWs of crystalline core Si covered with an amorphous layer were grown with this method [1.31 – 1.33].

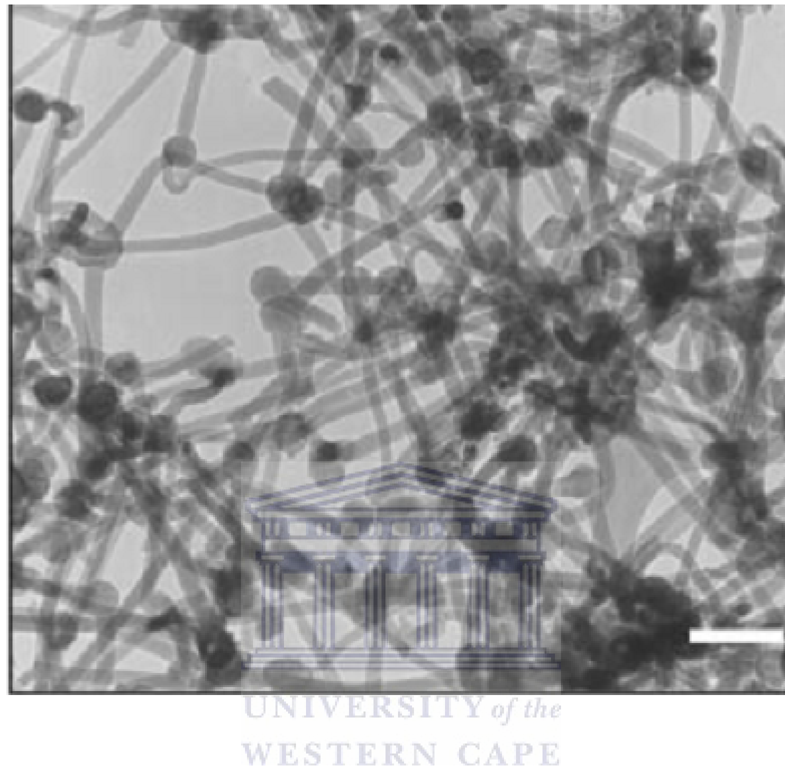

UNIVERSITY of the
WESTERN CAPE

Figure 1.13: TEM micrographs of silicon nanowires synthesised by laser ablation, scale bar 100 nm, [1.30].

Figure 1.14 shows that the top of the nanowires synthesised via laser ablation contain catalyst nanoparticles, which supports the notion that growth via this method follows the vapour-liquid-solid mechanism, explained earlier in this section. The nanoparticles were found to be about 1.5 to 2 times larger than the nanowire diameter and the preferred growth of the wires along$\langle 111 \rangle$, similar to that found when synthesised via the VLS method during CVD [1.32].

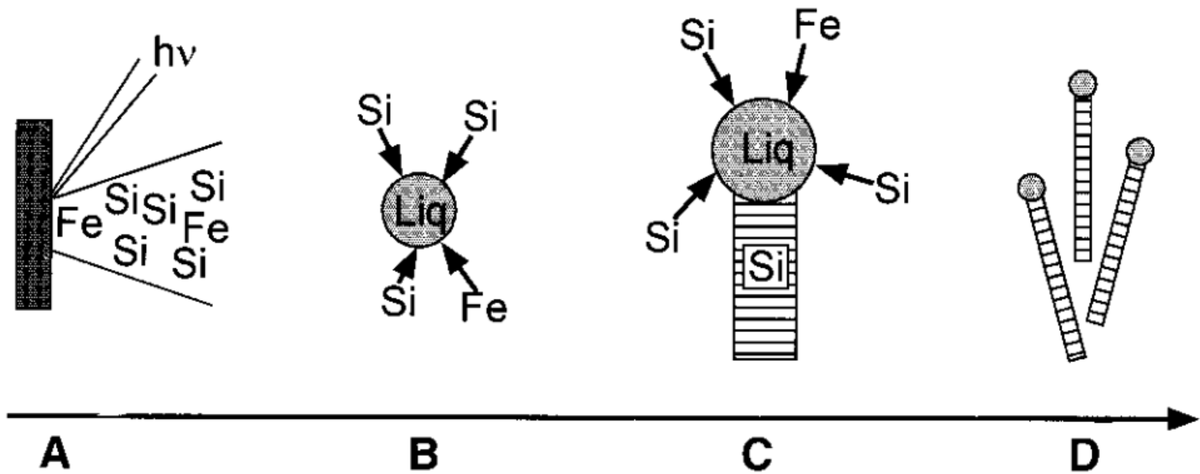

Figure 1.14: Growth mechanism during laser ablation for silicon nanowires growth [1.30].

As is the case for VLS via CVD, laser ablation also relies on high temperatures, in expensive equipment, to grow SiNWs. This technique also proves to be neither effective nor easy in controlling aspects like nanowire diameter. Rather, it is found that the wires grow randomly during this process. In addition, the thick oxide layer that is produced during growth normally requires post growth treatment in hydrofluoric acid for the removal of the SiO_2.

UNIVERSITY of the
WESTERN CAPE

1.7.4 Thermal Evaporation

Thermal evaporation is another method that employs high temperature and relatively low pressure systems to synthesise silicon nanowires. The method, however, does not necessary requires a metal catalyst such as Au, Ni or Fe to facilitate the growth of the nanostructures. Commonly, groups report on the growth of the nanowires using SiO as a source of silicon in vapour form. The SiO under high temperatures (850 – 1300 °C) liquefies into SiO nanoparticles which lead to the growth of silicon nanowires, typically on a silicon wafer [1.34, 1.35]. However, Ahmad and Hutagalung [1.37] have reported on thermal evaporation to synthesise SiNWs assisted by Ni catalyst.

Similar to CVD grown structures, the SiNWs grown via thermal evaporation typically have a crystalline silicon core, surrounded by a thicker amorphous SiO_2 layer and varies in diameter between 30 and 200 nm [1.34 – 1.36]. However, as shown by Niu *et al.* [1.35], highly crystalline Si nanowires, without the amorphous coating, is attainable via thermal

evaporation. In the case of catalyst prepared nanowires, Ahmad and Hutagalung reported that the nanowires terminated with Ni nanoparticles, which again shows a vapour-liquid-solid mechanism followed by thermal evaporation. Thermal evaporation, just like laser ablation and VLS via CVD, yields nanowires randomly grown on a substrate, unless patterning schemes are used.

1.7.5 Nanoimprint Lithography

As previously mentioned, silicon nanowires can be grown by either following a bottom-up or top-down approach, with the techniques discussed thus far employing a bottom-up approach. Nanoimprint lithography is a top-down method which can be combined with deep reactive ion etching (DRIE) [1.37] or metal assisted chemical etching (MaCE) [1.38]. This method forms a big part of lithography technology which includes electron beam lithography [1.39] and photolithography [1.40]. This section will focus mainly on nanoimprint lithography combined with MaCE, as it provides a much cheaper alternative to electron beam lithography and photolithography techniques.

UNIVERSITY of the
WESTERN CAPE

Lithography techniques have been combined with MaCE successfully over the years to synthesise silicon nanostructures such as nanoporous silicon [1.38], silicon nanopillers [1.40] and silicon nanowires [1.42, 1.43], with different approaches followed. For example, Huang *et al.* [1.42] used polystyrene (PS) spheres to control the diameter and density of the resulting nanowires. They found that by tuning the diameter of the PS spheres using reactive ion etching (RIE) they were able to control the resultant diameters of the nanowires. As shown in Figure 1.15, PS spheres were deposited onto a Si substrate and their diameters reduced using RIE. A thin layer of silver catalyst was then thermally evaporated onto the Si substrate, followed by etching in water, HF and H_2O_2 solution. It was found that the etching of the silicon substrate only occurred in regions where the polystyrene spheres of 250 nm diameters remained. Average diameters of the resultant wires were slightly less (about 1 – 2 nm less) than the diameters of the PS spheres. It was further found that control over the diameters of the PS spheres can only be maintained down to 100 nm, with diameters smaller than that affecting the ordering of the PS spheres [1.42, 1.43].

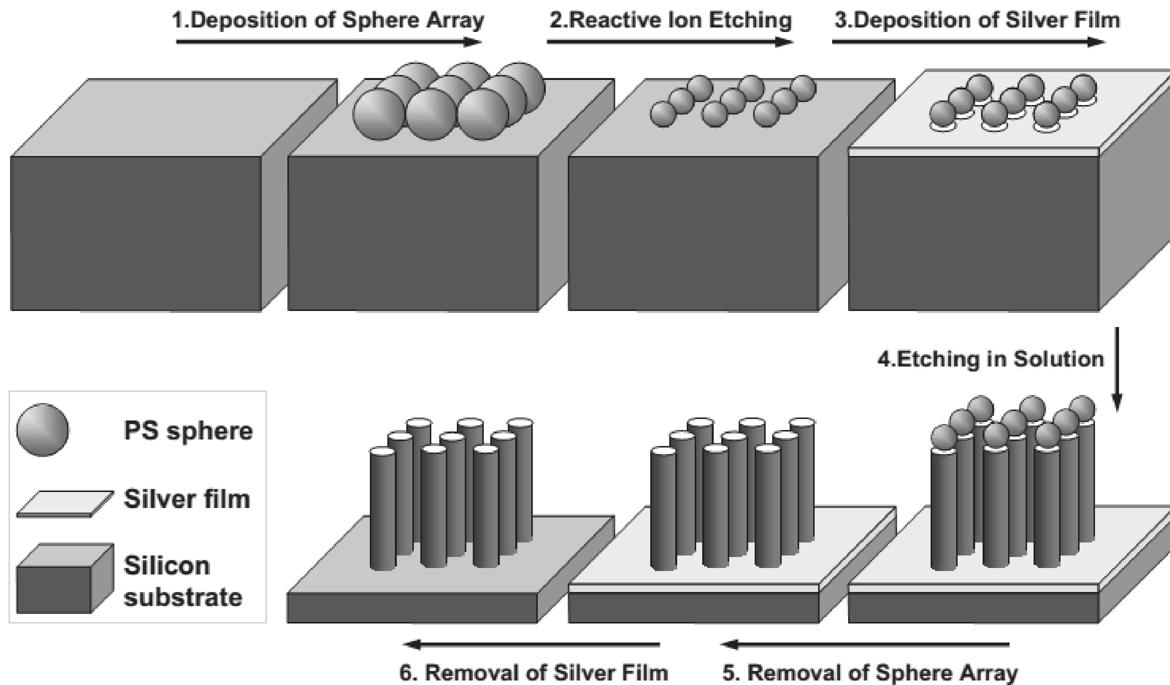

Figure 1.15: Schematic presentation of synthesis during lithography using PS spheres combined with MaCE [1.42].

Choi *et al.* [1.43] reported on a variation of the above technique, called interference lithography [1.43]. During this technique, a laser of specific energy is used to pattern a photo-resist layer deposited on a Si substrate, to form circular-shaped photo-resist dots. A thin layer of gold is then deposited onto the dots, followed by etching of the entire substrate in an etching solution. Similar to the model shown in Figure 1.15, the silicon nanowire formation only occurred in the areas where the photo-resist dots were located. However, in contrast to the technique reported by Huang *et al.* [1.42], Choi *et al.* found that with this method the diameters of the resulting SiNWs could be controlled all the way to about 20 nm over large surface areas (1 x 1 cm^2).

There are advantages in using lithography techniques, of which the obvious one would be the fact that one can gain control over the desired morphology. This includes control over the position of the nanowires on the substrate, the diameter and the packing density of the nanowires. Furthermore, the preferred orientation of the resulting nanowires can be much manipulated by simply choosing an appropriate Si substrate. However, lithography can however be very expensive depending on the method implemented; this includes the use of

reactive ion etching and the deposition of the catalyst layer, which may require low pressure systems [1.37 – 1.43].

MaCE, by itself, can give results similar to the lithography patterning technology, however, at much lower cost and reduced time. The techniques of silicon nanowire synthesis discussed above aim at achieving different aspects of these nanostructures, each with its advantages and disadvantages. All bottom-up approach methods (VLS via CVD, laser ablation and thermal evaporation methods) depend on high temperature and low pressure instruments. These methods can produce very thin nanowires, from as small as 2 nm to as big as 100 nm [1.30, 1.34], but if not patterned they produce randomly grown nanowires. This has led to the employment of lithography patterning techniques during top-down approach for the manufacturing of vertically aligned arrays of nanowires. However, all the above techniques prove to be expensive, with sophisticated high temperature, low pressure and laser equipment required for successful synthesis. For these reasons, research aimed at reducing cost, while maintaining vertical alignment of the SiNWs for various applications; employ inexpensive equipment, at atmospheric pressure and room temperature. MaCE is proving to be an ideal candidate and as such will be employed exclusively during this work for the synthesis of vertically aligned SiNW arrays; a detailed discussion on the underlying physics and chemistry of the technique will be discussed in Chapter Two.

UNIVERSITY of the
WESTERN CAPE

1.8 Aims and Outline of Thesis

The rapid depletion of fossil fuel resources and its effect on using fossil fuels as a source of energy has led to a pending energy crisis. Added to the long-standing negative effects that this method of energy conversion has had on global climate change, the intense focus on finding suitable renewable energy sources, comes as no surprise. In particular, the drive to optimally make use of solar energy, which is the most abundant renewable form, receives a vast amount of interest. Photovoltaic technology, mainly based on silicon solar cells, has shown its effectiveness in solving the problem, but at high cost. Cost reduction in these devices has been observed but at reduced efficiency, thus requiring further research.

Vertically aligned SiNWs, synthesised via the MaCE technique, have shown promise as a low cost solution for improving the efficiency of these thin film solar cells due to their suitability as an antireflective layer for incoming light. In addition, SiNWs offers effective carrier collection and charge separation owing to their aligned structure in which light is absorbed axially and charge collected radially. Thus these nanowires can be used in radial and axial solar cells due to their carrier transport path. Although many reports on SiNWs synthesised through MaCE have been published, a lack in clarity on the formation of the nanowires persist. As such, the overall aim of this study will be to investigate the formation of SiNWs during MaCE using a wide range of characterisation techniques. In particular, the study will aim to develop an understanding of the following important processes during nanowire formation:

- Evolution of the Ag catalyst during etching
- Morphology of the resultant arrays of nanowires and the parameters influencing the morphology during MaCE in terms of length and diameter
- Structural properties of the SiNW arrays, crystallinity and preferential etching direction
- Oxide formation during and post MaCE process
- Optical properties, specifically reflectivity on incident light

The investigation will be carried out using electron microscopy for the study of the overall morphology of the nanowire layers, elemental composition and localised crystalline properties, x-ray diffraction in conjunction with Raman spectroscopy for the probing of the bulk crystalline properties, infrared to study the bulk bonding properties and ultraviolet-visible (UV-Vis) spectroscopy to measure the reflection of light in the UV-Vis range. The thesis lay-out is as follows:

Chapter One gave a broad background on the global energy mix and the need for renewable energy. Specifically, the importance of solar cells in directly converting solar energy, which is the most abundant renewable energy source, into electrical energy was discussed and motivated. Chapter One also described how 1-D arrays of Si nanowires have the potential to lower the cost while enhancing the overall device efficiency of second generation p-n

junction solar cells, with the major growth and synthesis techniques of these structures summarised.

Chapter Two will look in detail into the mechanism of metal assisted chemical etching, synthesis parameters, preferred growth directions of SiNWs and some properties of nanowires. The chapter will also discuss the experimental procedures followed during synthesis and the parameters which are important to consider in controlling the physical dimension of the nanowires.

Chapter Three will provide a comprehensive summary of the characterisation techniques employed in this study in terms of their theory, basic working principles and the experimental set-up employed during data acquisition for SiNWs.

Chapter Four will discuss the results of the morphology of silver nanoparticles deposited at different conditions as well as the SiNWs synthesised at different MaCE conditions; structural properties, surface passivation and optical properties of the SiNWs will also be discussed.

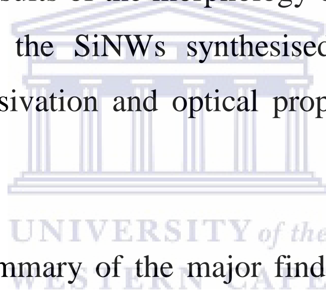
UNIVERSITY of the
WESTERN CAPE

Chapter Five will provide a summary of the major findings of this work as well as give details for further future studies.

References

[1.1] O. Edenhofer, R. Madruga, Y. Sokona, K. Seyboth, P. Matschoss, S. Kadner, T. Zwickel, P. Eickemeier, G. Hansen, S. Schlömer, C. Von Stechow, "*Summary for Policymakers: In IPCC Special Report on Renewable Energy Sources and Climate Change Mitigation*", Cambridge University Press, Cambridge, United Kingdom and New York, USA (2011).

[1.2] D. Goswami, F. Kreith, *"Energy Conversion"*, CRC Press Taylor & Francis Group, New York, USA (2008).

[1.3] BP Statistical Review of World Energy, June 2013. [Online]. Available: www.pb.com/statisticalreview [Accessed: 23 May 2014]

[1.4] M. Kaltschmitt, W. Streicher, A. Wiese, "*Renewable Energy – Technology, Economics and Environment"*, Springer Berlin, Heidelberg and New York (2007).

[1.5] L. Chaar, L. Lamont and N. Zein, Renewable and Sustainable Energy Reviews, **15** (2011) 2165 – 2175.

[1.6] W. Moomaw, F. Yamba, M. Kamimoto, L. Maurice, J. Nyboer, K. Urama and T. Weir, "*Introduction: In IPCC Special Report on Renewable Energy Sources and Climate Change Mitigation"*, Cambridge University Press, Cambridge, United Kingdom and New York, NY, USA (2011)

[1.7] H. Chum, A. Faaij, J. Moreira, G. Berndes, P. Dhamija, H. Dong, B. Gabrielle, A. Eng, W. Lucht, M. Mapako, O. Masera Cerutti, T. McIntyre, T. Minowa and K. Pingoud, "*Bioenergy: In IPCC Special Report on Renewable Energy Sources and Climate Change Mitigation"*, Cambridge University Press, Cambridge, United Kingdom and New York, USA (2011).

[1.8] A. Kumar, T. Schei, A. Ahenkorah, R. Rodriguez, J. Devernay, M. Freitas, D. Hall, A. Killingtveit and Z. Liu, "*Hydropower: In IPCC Special Report on Renewable Energy Sources and Climate Change Mitigation"*, Cambridge University Press, Cambridge, United Kingdom and New York, US (2011).

[1.9] D. Arvizu, P. Balaya, L. Cabeza, T. Hollands, A. Jäger-Waldau, M. Kondo, C. Konseibo, V. Meleshk, Y. Tamaura, H. Xu and R. Zilles, "*Direct Solar Energy: In IPCC Special Report on Renewable Energy Sources and Climate Change*

Mitigation", Cambridge University Press, Cambridge, UK and New York, USA (2011).

[1.10] Department of Energy, Republic of South Africa, 2014. *Clean Energy*. [Online]. Available: www.energy.gov.za [Accessed: 27 May 2014]

[1.11] L. Tsakalakos, Materials Science and Engineering R **62** (2008) 175 – 189.

[1.12] A. Shah, P. Torres, R. Tscharner, N. Wyrsch and H. Keppner, Science **285** (1999) 692 – 698.

[1.13] J. Nelson, "*The Physics of Solar Cells*", Imperial Collage, UK (2003).

[1.14] R. Van Overstraeten and R. Mertens, "*Physics, Technology and use of Photovoltaic"*, Adam Hilger Ltd, Bristol and Boston (1986)

[1.15] C. Kittel, "*Introduction to Solid State Physics"*, John Wiley & Sons, Inc., USA. (2005).

[1.16] E. Gurnee, Journal of Chemical Education **46** (1969) 80 – 85.

[1.17] S. De Wolf, A. Descoeudres, Z. Holman and C. Ballif, Green **2** (2012) 7 – 24.

[1.18] Y. Kuang, M. Di Vece, J. Rath, L. Van Dijk and R. Schropp, Reports on Progress in Physics **76** (2013) 106502 – 106531.

[1.19] K. Peng and S. Lee, Advanced Materials **23** (2011) 198 – 215.

[1.20] E. Garnett, M. Brongersma, Y. Cui, and M. McGehee, Annual Review in Materials Research **41** (2011) 269 – 295.

[1.21] V. Schmidt, J. Wittemann, and U. Gösele, Advanced Material **21** (2009) 2681 – 2702.

[1.22] R. Wagner and W. Ellis, Applied Physics Letters **4** (1964) 89 – 90.

[1.23] Q. Hu, H. Suzuki, H. Gao, H. Araki, W. Yang and T. Noda, Chemical Physics Letters **378** (2003) 299 – 304.

[1.24] E. Garnett, M. Brongersma, Y. Cui and M. McGehee, Annual Review of Materials Research **41** (2011) 269 – 295.

[1.25] C. Kuo and C. Gau, Thin Solid Films **519** (2011) 3603 – 3607.

[1.26] H. Choi, "*Nanoscience and Technology"*, Springer-Verlag, Berlin, Heidelberg, (2012).

UNIVERSITY of the
WESTERN CAPE

[1.27] Z. Zhong, C. Yang and C. Lieber in V. Kumar, "*Nanosilicon*", Elsevier, Oxford, London, UK, (2007) [pp. 176 – 214].

[1.28] Y. Cui, L. Lauhon, M. Gudiksen, J. Wang and C. Lieber, Applied Physics Letters **78** (2001) 2214 – 2216.

[1.29] Y. Wu and P. Yang, Journal of American Chemical Society **123** (2001) 3165 – 3166

[1.30] A. Morales and C. Lieber, Science **279** (1998) 208 – 211.

[1.31] N. Fukata, T. Oshima, N. Okada, T. Kizuka, T. Tsurui, S. Ito and K. Murakami, Physica B **376 – 377** (2006) 864 – 867.

[1.32] N. Saddiqi, H. Javed, M. Islam and K. Ghauri, Chemistry and Materials Research **6** (2014) 76 – 86.

[1.33] N. Fukata, T. Oshima, N. Okada, K. Murakami, T. Kizuka, T. Tsurui and S. Ito, Journalof Applied Physics **100** (2006) 024311 – 024318.

[1.34] Z. Zhang, X. Fan, C. Lee and S. Lee, Chemical Physics Letters **337** (2001) 18 – 24.

[1.35] J. Niu, J. Sha and D. Yang, Physica E **23** (2004) 131 – 134.

[1.36] A. Ahmad and S. Hutagalung, Journal of Applied Science **11** (2011) 3586 – 3592

[1.37] K. Morton, G. Nieberg and S. Chou, Nanotechnology **19** (2008) 345301 – 345307.

[1.38] D. Wang, S. Schonherr, R. Ji, A. Herz, C. Ronning and P. Schaaf, Journal of Micromechanics and Microengineering **23** (2013) 074004 – 074010.

[1.39] Y. Choi, J. Grunes, J. Lee, J. Zhu, G. Somorjai, L. Lee and J. Bokor, Proceedings of SPIE (Nanofabrication Technologies) **5220** (2003) 10 – 19.

[1.40] J. Rashid, J. Abdullah and R. Hajian, Journal of Nanomaterials **2003** (2003) 1 – 16.

[1.41] D. Wang, S. Schonherr, C. Ronning and P. Schaaf, Materials Letters **98** (2013) 186 – 189.

[1.42] Z. Huang, H. Fang and J. Zhu, Advanced Material **19** (2007) 744 – 748.

[1.43] W. Choi, T. Liew, M. Dawood, H. Smith, C. Thompson and M. Hong, Nano Letters **8** (2008) 3799 – 3802.

UNIVERSITY of the WESTERN CAPE

CHAPTER TWO

Metal Assisted Chemical Etching

2.1 Introduction

One-dimensional (1-D) SiNWs form part of an intensive research focus on silicon nanostructures and porous silicon. The research is motivated by the excellent properties shown by SiNWs, e.g. their excellent optical and electrical properties with a large surface-to-volume ratios and high aspect ratio, rendering it promising material for application in many technological devices such as photovoltaic cells based on nanostructures [2.1 – 2.5]. This chapter will discuss the mechanism behind metal assisted chemical etching (MaCE), briefly introduced towards the end of Chapter One, some of the most important properties of SiNWs and the experimental approach taken during the course of this study to synthesise arrays of 1-D SiNWs.

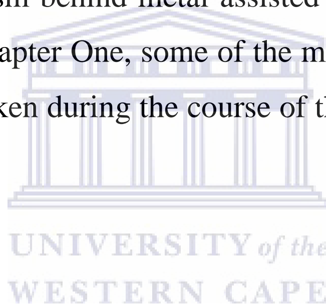

2.2 Background of Metal Assisted Chemical Etching

As mentioned in Chapter One, research on SiNWs started around 1957 following a report by Treuting and Arnold [2.6] in which few years later (1964) Wagner and Ellis [2.7] discovered the principle technique of vapour-liquid-solid mechanism during chemical vapour deposition for the growth of SiNWs [2.7]. It was not until 1997 where the etching method was reported for the synthesis of porous silicon, in chemical baths containing hydrofluoric acid (HF), hydrogen peroxide (H_2O_2) and nitric acid (HNO_3) without the use of high temperatures or low pressure systems. This top-down approach was termed metal assisted chemical etching.

Li and Bohn [2.8] were the first researchers to explore MaCE in detail, in 2000. They realized that by depositing a thin layer of noble metal on top of silicon substrate and etch that into HF plus an oxidant (H_2O_2) containing solution, porous silicon of straight pores were obtained. Other groups improved on this ground-breaking work to produce different silicon nanostructures, including silicon nanowires [2.1]. Further etching based techniques were also

developed in this time to synthesise silicon nanowires, all aimed at controlling different properties or aspects of these nanostructures. These include some of the more expensive methods, such as lithography patterning and reactive ion etching (RIE) [2.1, 2.5]. However, MaCE is unique from these techniques simply because the technique allows easy control over the resulting morphology or structures without the use of complicated vacuum or high temperature equipment.

Metal assisted chemical etching is considered a wet etching method and is based on electroless metal particle deposition followed by an etching step [2.9]. Three main important conditions required during MaCE are the need of a complexing agent which is played by hydrofluoric acid (HF), metal nanoparticles for catalyses purposes and lastly an oxidant which needs to have higher reduction potential than the semiconductor material e.g. silicon [2.10]. Other groups have however reported on the one-step synthesis, where the nanowires were only grown using the combination of HF and metal catalyst which also plays the role of an oxidant [2.9]. It was also reported by Bai *et al.* the growth of silicon nanowires by following another one-step synthesis where the two steps are done simultaneously, in other words the nanowires were grown from the solution of HF, metal salt and an oxidant combined into one solution [2.11]. This method is opposing the normal route of MaCE (two-step synthesis) where the nanoparticles are deposited and then the nanowires are grown from a different solution.

This technique is regarded as being simple, low cost and easy to control which produces different kinds of silicon nanostructures including silicon nanowires and porous silicon among others [2.12, 2.13]. SiNWs grown via MaCE have high aspect ratios [2.13] and large surface to volume ratios as was mentioned earlier in this chapter [2.5]. Depending on the original orientation of the Si wafer, MaCE produces vertically aligned silicon nanowires, uniformly grown on the wafer (especially the Si (100) wafer) [2.1], and lastly high quality of crystallinity from resulting SiNWs is obtainable [2.14]. The research on this technique came recent (90's) as to play a role in the current research on silicon nanostructures as it holds advantages over some of the techniques used to grow silicon nanowires such as VLS method and dry etching methods (reactive ion etching (RIE)) [2.6, 2.13].

The new research based on the production of photovoltaics is looking at reducing the amount of material used; reducing the fabrication cost and must be user friendly. MaCE provides

solutions for these requirements as the technique grows silicon nanostructures at lower cost, not only for photovoltaic technology but for other nano-electronic devices as well. Some of the techniques briefly explained in chapter one does provide good properties but difficult to control or maintain the nanostructure's morphologies which make it difficult to control the properties. Huang *et al.* [2.1] and X. Li [2.13] included in their respective reports few advantages of MaCE over VLS and RIE, respectively. One of the disadvantages of VLS and RIE is that these methods require expensive instruments which operate at high temperatures or low pressure; others require hazardous silicon precursors for the synthesis [2.15].

There have been however arguments and disagreements on the mechanism of MaCE which includes the role that metal particles plays during synthesis of SiNWs; the preferred etching directions as compared to the starting Si wafers [2.1]. It is thus important to look into details the mechanism of metal assisted chemical etching in order to understand the resulting nanostructures. The mechanism is discussed below starting from deposited silver nanoparticles to the resulting nanowires.

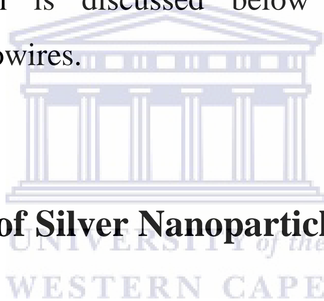
UNIVERSITY of the
WESTERN CAPE

2.3 Formation Mechanism of Silver Nanoparticles

During the two step synthesis of SiNWs through MaCE, firstly the metal nanoparticles are deposited using solutions containing HF, deionised water and the desired metal salt, which can be Ag, Au or Pt [2.13]. Platinum assisted etching does not necessarily result in SiNWs but it is used for Si etching [2.16]. Silver is mostly used in the MaCE method, dissolved in the form of silver nitrate ($AgNO_3$) as the metal salt [2.13 - 2.16]. The metal nanoparticles can also be deposited through spin coating using preformed nanoparticles or thermal evaporation of thin films [2.10]. Chemical solution based reduction of noble metal salts is the easy way of depositing nanoparticles as it only requires solution mixtures in a small beaker.

Deposition process of silver nanoparticles (AgNPs) is known as an electroless metal deposition (EMD) which follows the techniques of galvanic displacement process [2.17]. Galvanic displacement follows two simultaneous processes during cathodic and anodic reactions. The cathodic reaction results in the reduction of metal ions (Ag^+ to Ag^0) whereas the anodic reaction leads to the oxidation of silicon underneath the AgNPs to form silicon

dioxide (SiO_2) [2.16 – 2.18]. When the Si substrate is submerged in the aqueous solution of HF, $AgNO_3$ and deionised H_2O the cathodic and anodic reactions occur simultaneously. In the process Ag is deposited onto the silicon surface in the form of metallic silver ions (Ag^+) via cathode reaction, as shown in equation (2.1). The process happens in a way that silver injects holes in the valence band (VB) of silicon. The injected holes causes the Si-Si bonds to release electrons which are attracted by Ag^+ for their reduction, in which silicon oxidise and dissolved by HF.

This mechanism is favoured in regions where Si with silver is exposed to the HF solution. Ag^+ receives electrons from Si and becomes chemically neutral, resulting in small silver nuclei on the surface of silicon as shown in Figure 2.1 (a). Because the Ag nuclei have higher electronegativity than the VB of silicon, the silver continues attracting electrons from Si, eventually causing the silver nuclei to become negatively charged [2.19]. At that stage the negatively charge silver ions will donate the electrons to the other Ag^+ ions at the silicon surface. This transfer of electrons also reduces those incoming Ag^+ ions into silver nuclei which will be deposited around the previously formed silver nuclei, which results in the silver nuclei on the silicon surface growing into larger silver nanoparticles which at times rather choose spherical or semi spherical shapes [2.14, 2.18, 2.19].

UNIVERSITY of the
WESTERN CAPE

Cathode reaction

$$Ag^+ + e^-_{VB} = Ag^0 \,, \; E^0 = 0.79 \text{ V (v. SHE (Standard Hydrogen Electrode))} \qquad (2.1)$$

Anode reactions

$$Si + 2H_2O = SiO_2 + 4H^+ + 4e^- \qquad (2.2)$$

$$SiO_2 + 6HF = SiF_6^{2-} + 2H_2O + 2H^+ \qquad (2.3)$$

The overall reaction, combining reactions (2.1) – (2.3) yields:

$$Si + 6HF + 4Ag^+ = 4Ag + SiF_6^{2-} + 6H^+ \qquad (2.4)$$

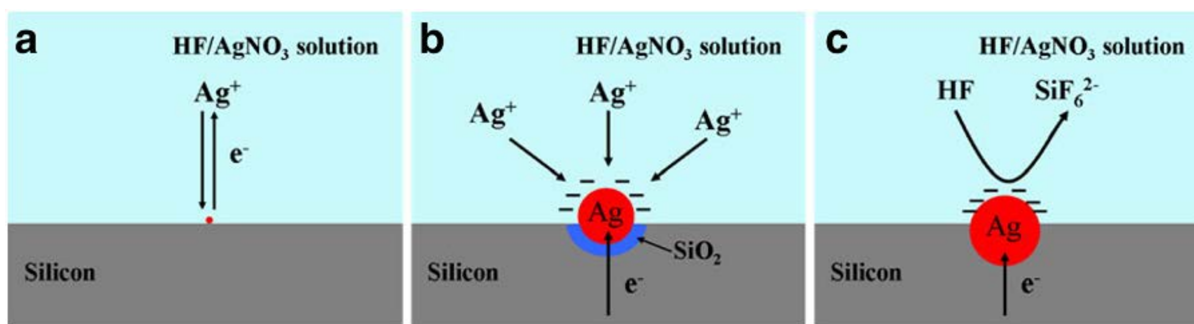

Figure 2.1: Schematic representation of silver nanoparticle formation mechanism [2.12].

The silicon underneath the silver particles is dissolved, leaving small pits during the initial stages of etching. It was argued by Nassiopoulou *et al.* [2.14] that the silicon oxidation results from the injection of holes and by the simultaneous gain of electrons by Ag^+. The pit formation is due to the fact that the surface Si bonding electrons are transferred to Ag^+ ions and at the same time the silicon oxidises to SiO_2 and etched away by HF as shown in Figure 2.1 (b). As shown by reaction in equation (2.3) and Figure 2.1 (c), the area beneath the SiO_2 is dissolved in the form of a soluble fluorosilicate compound (SiF_6^{2-}) into the etching solution. AgNPs sink into those pits, which have a diameter relative to the AgNPs, and act as a catalyst during the formation of the SiNWs.

UNIVERSITY of the
WESTERN CAPE

It is clear from these reactions that all the chemical components have their respective major roles during the deposition of AgNPs. For example, silver nitrate for the creation of silver ions, HF for SiO_2 dissolution and silicon (not chemical) for electron supply during silver reduction. It was observed that longer immersion of the Si into the $AgNO_3$ solution resulted into AgNPs growing larger, such as those reported by Smith *et al.* [2.10] in Figure 2.2, known as dendrite structures.

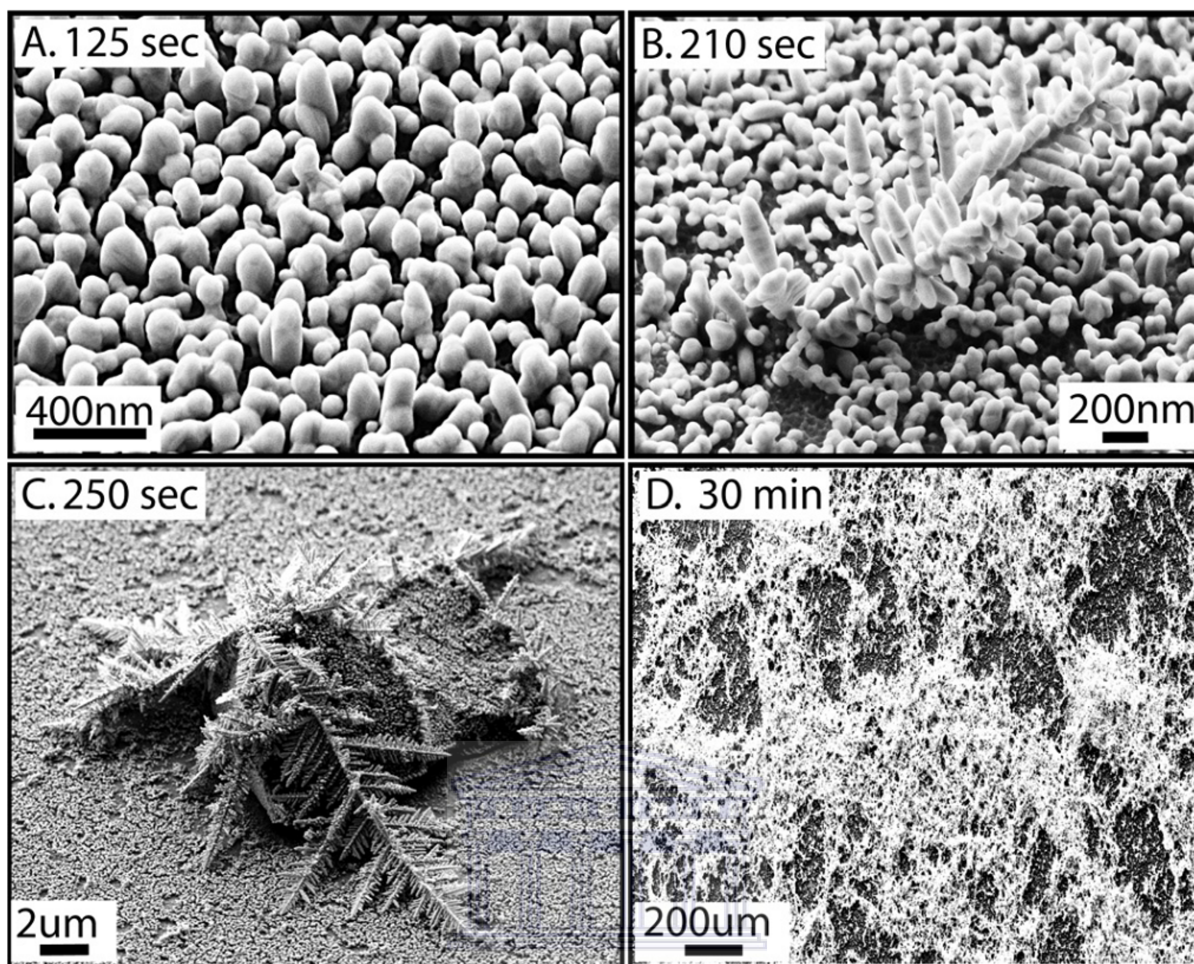

UNIVERSITY of the
WESTERN CAPE

Figure 2.2: Scanning electron micrograph (SEM) of AgNPs deposited at different times with concentration of 5 mM $AgNO_3$ where images (b) – (d) shows the formation of dendrite structures [2.10].

Qu *et al.* [2.20] reported that the packing density of these AgNPs may also be affected by the doping level of the Si wafer. They found that the packing density increases as the doping level increases, as shown in Figure 2.3. This was attributed to the fact that the growth of the nanoparticles is preferred around defective states, since the energy barrier in that region is low and ideal for redox reactions. It would be interesting to see how the resulting nanowires looks like when there are different AgNPs structures, to see how does the packing density affects the resulting SiNWs, but that will be discussed during formation of SiNWs.

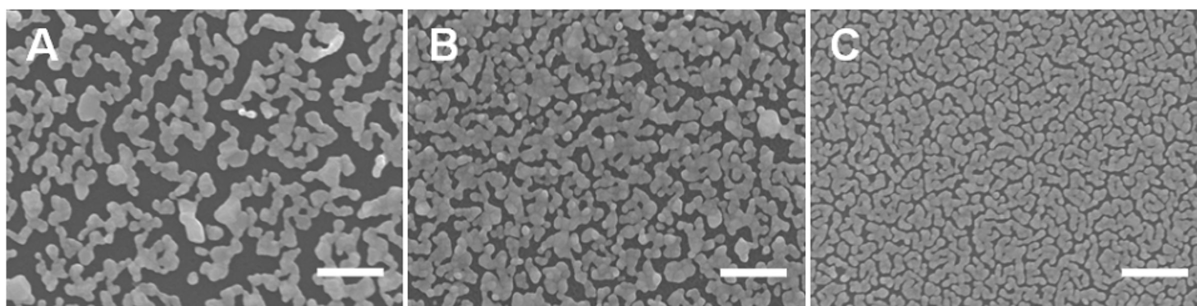

Figure 2.3: SEM micrographs of AgNPs deposited at different doping levels of Si piece. (a) 1 – 5 Ω·cm; (b). 0.3 – 0.8 Ω·cm and (c) 0.008 – 0.02 Ω·cm. Deposition time was 1 minute using 5 mM $AgNO_3$ concentration and the scale bar is 500 nm [2.20].

2.4 Formation Mechanism of Silicon Nanowires

UNIVERSITY of the
WESTERN CAPE

Two step syntheses of silicon nanowires hold some advantages over the one step process because in the one step method it is difficult to study the individual steps of the growth/etching mechanism. In one step synthesis the SiNWs are synthesised from a single solution of $AgNO_3$/HF/deionised water often resulting in big Ag dendrite structure formation on the Si surface, making it difficult to study morphology of the nanowires without dissolving the Ag into nitric acid (HNO_3) [2.12, 2.21]. During this process Ag plays the role of catalyst and an oxidant. It is however easier in the two step process where AgNPs are deposited and then samples are transferred into an etching solution. This way the evolution of the nanowires can be studied easily without dissolving the nanoparticles.

In two step synthesis the AgNPs are deposited on the Si substrate and then rinsed in water to remove extra Ag ions, followed by the etching step in an oxidant containing solution. It is known that any oxidant with a higher reduction potential than Si can be used to grow SiNWs. These oxidants include $Cr_2O_7^{2-}$, MnO_4^-, HNO_3, $S_2O_8^{2-}$ [2.10] and $Fe(NO_3)_3$ [2.16], with the preferred oxidant being H_2O_2. Hydrogen peroxide is mostly used because it has a more positive electro-potential than the valence band of silicon and also more than that of other mentioned oxidants [2.1]. H_2O_2 provides a faster etching rate than AgNPs because it has a higher positive redox potential than Ag^+ (1.77 V for H_2O_2 and 0.79 V for Ag^+).

When the AgNPs coated Si wafers are removed from deposition solutions and rinsed with water, the reactions stops immediately. But when these samples are immersed into an etching solution containing H_2O_2 another two simultaneous redox reactions take place. The side of the nanoparticles facing the etching solution act as a cathode site and the side facing silicon as an anode site. The reactions that take place are as follow:

Cathode (Ag side facing solution)

$$H_2O_2 + 2H^+ + 2e^- \rightarrow 2H_2O, \quad E^0 = 1.78 \text{ V (v. SHE)} \quad (2.5)$$

Anode (Ag side facing Si)

$$Si + 2H_2O \rightarrow SiO_2 + 4H^+ + 4e^-, \quad E^0 \cong 0.91 \text{ V (v. SHE)} \quad (2.6)$$

$$SiO_2 + 6HF \rightarrow H_2SiF_6 + 2H_2O \quad (2.7)$$

$$Si + 6HF \rightarrow H_2SiF_6 + 4H^+ + 4e^-, \quad E^0 = 1.2 \text{ V (v. SHE)} \quad (2.8)$$

Overall reaction:

$$Si + 2H_2O_2 + 6HF \rightarrow H_2SiF_6 + 2H_2O \quad (2.9)$$

UNIVERSITY of the
WESTERN CAPE

During the reaction in equation (2.5) the AgNPs sitting on pits in the silicon substrate surface capture electrons from Si. These electrons are then transferred to H_2O_2 for its reduction, during which time the H_2O_2 also consumes protons (H^+) [2.17, 2.20]. H_2O_2 has more positive electrochemical potential than the valence band (VB) of Si and thus easily inject holes into the Si VB. The hole injection results into the oxidation of Si during anode reactions in equation (2.6) and (2.7). In the anode site where Si is oxidised, it provides electrons and protons (equation (2.6) to Ag, and the Ag transfers those electrons and protons to the oxidant (H_2O_2) for its reduction. SiO_2 is formed immediately via anode equation (2.6) and etched away by HF as shown by reaction in equation (2.8) and Figure 2.4 (a). This happens as long as there is H_2O_2 to be reduced in which during that process AgNPs sinks deep into the pits forming silicon nanowires also shown in Figure 2.4 (b). The etching of Si is localized on the AgNPs/Si interface and the regions where there are no AgNPs would be the resulting SiNWs.

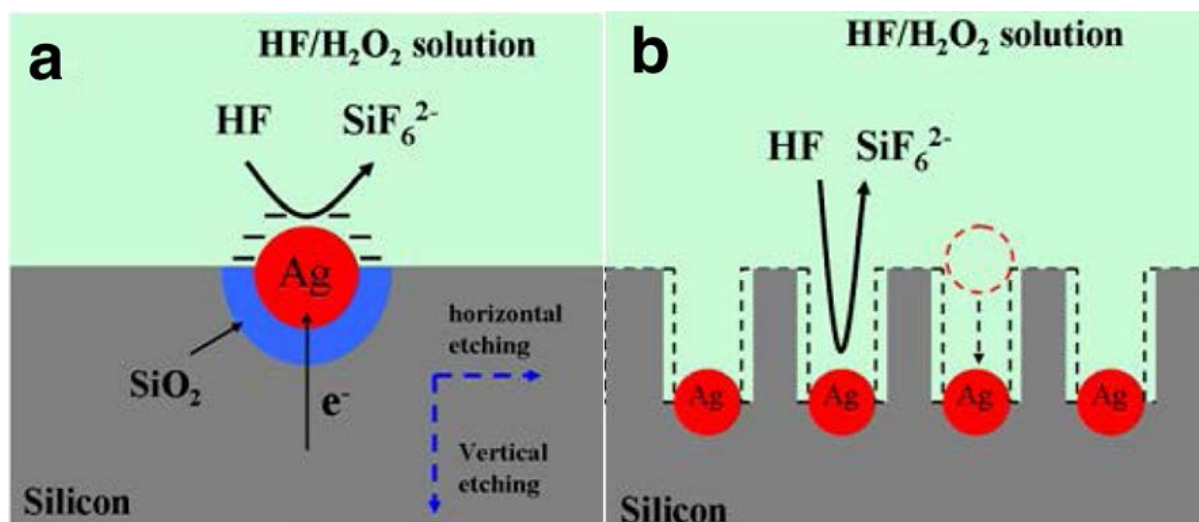

Figure 2.4: Mechanism formation of SiNWs in two-step synthesis showing how nanowires develop from deposited AgNPs [2.12].

Figure 2.5 shows a SEM micrograph of SiNWs reported by Huang *et al.* (2010) [2.18] synthesised from an aqueous solution of HF and H_2O_2 but did not mention the etching time duration. The nanowires are vertical with respect to the silicon substrate, highly dense with remnants of AgNPs visible in their bottoms. The insert shows the top view SEM of these nanowires with pores depicting the sinking of AgNPs leaving un-etched regions on the surface of the substrate.

UNIVERSITY of the WESTERN CAPE

AgNPs are usually dissolved into concentrated HNO_3 [2.12, 2.21] in which during the process Ag combines with HNO_3 to form other compounds via these following reactions [2.22]:

For concentrated HNO_3

$$Ag + 2HNO_3 \rightarrow AgNO_3 + NO_2 + H_2O \quad (2.10)$$

For diluted HNO_3

$$3Ag + 4HNO_3 \rightarrow 3AgNO_3 + NO + 2H_2O \quad (2.11)$$

For the combination of equation (2.10) and (2.11)

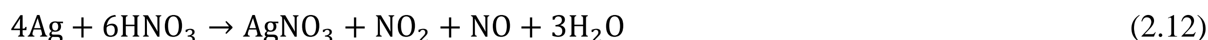

$$4Ag + 6HNO_3 \rightarrow AgNO_3 + NO_2 + NO + 3H_2O \quad (2.12)$$

These equations (2.10) – (2.12) shows that AgNPs can be dissolved in different ways depending on the concentration of the nitric acid used. The formed $AgNO_3$ also dissolves in water.

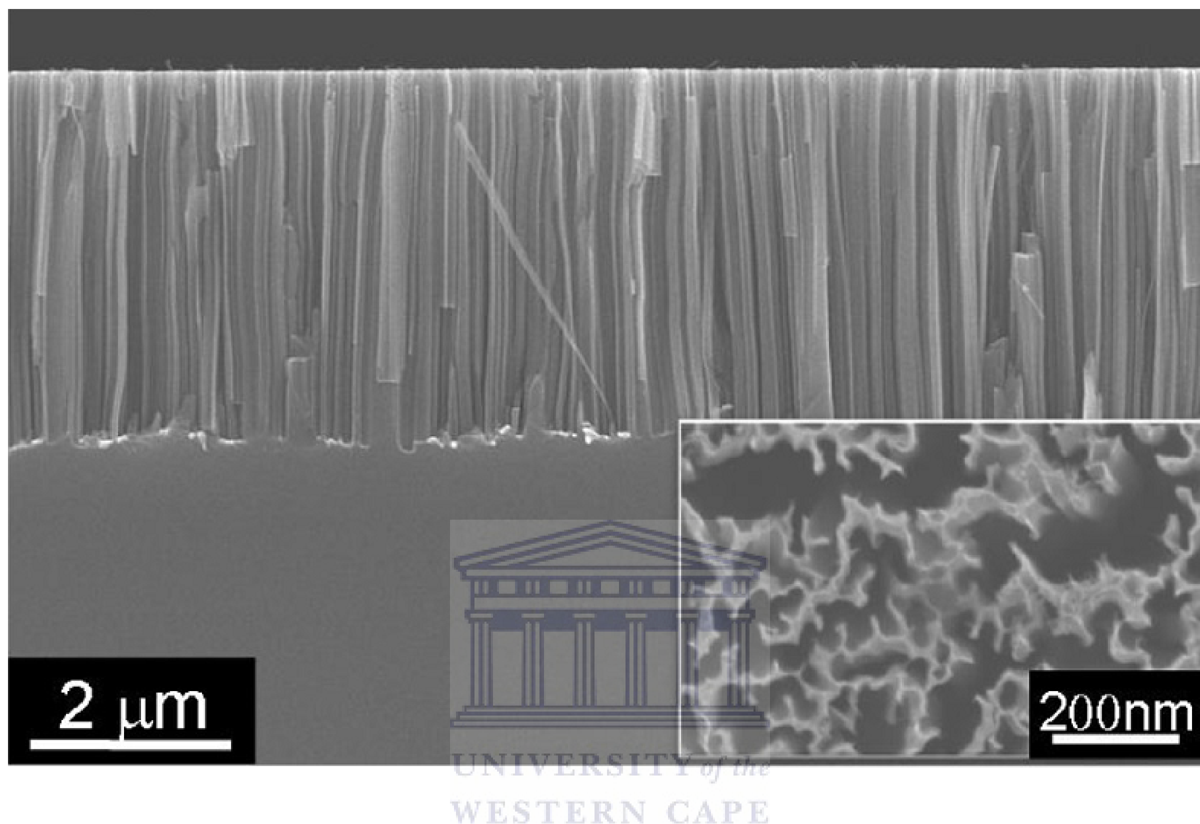

UNIVERSITY of the
WESTERN CAPE

Figure 2.5: Cross sectional SEM micrograph of vertical SiNWs synthesised from an aqueous solution of HF/H_2O_2 with an insert showing the top view of the nanowires [2.18].

2.5 Silicon Nanowires Synthesis Parameters

As discussed above etching of Si pieces covered with AgNPs in a solution containing HF, H_2O_2 and water will yield SiNWs. The mechanism shows that AgNPs sink into the substrate leaving vertically standing nanowires. This sinking of nanoparticles means that their density on the surface will determine the morphology of resulting nanowires. This is because the spaces between nanoparticles during etching will be left un-etched and depending on how the particles are arranged the nanowires will be formed. In contrast, nanoparticles with large spaces in between will result into larger SiNWs and densely packed AgNPs will result into

smaller nanowires, but this cannot be true all the time as the introduction of oxidants also changes the shape of the nanoparticles [2.1]. Fang *et al.* [2.15] also reported that different thin layers of Ag nanoclusters on top of Si substrate resulted into different etched structures [2.15].

Etching solution concentration, time and temperature all affect the resulting nanowires, mainly the length [2.1, 2.21]. It has been reported that by increasing the oxidant concentration or the etching time greatly increased the SiNW length [2.23 – 2.25]. The influence of high oxidant concentration could be explained in terms of high etching rate due to the high concentration. Longer etching times allow for enough time for etching to occur as the synthesis stops when samples are taken out of solution and rinsed with deionised water. In most reports the relation between etching time or oxidant concentration has been found to be more linear [e.g. as in 2.23]. The nanowires grow longer than 10 μm and form congregated bundles at their tops. Lin *et al.* [2.23] discussed the effect of both the oxidant concentration and etching time in the evolution of nanopores on the sidewalls of formed SiNWs. The formation of nanopores is also explained by chemical reactions within the solution containing H_2O_2 during etching. Ag ions (Ag^+) are formed when the AgNPs coated samples are immersed into H_2O_2 containing solution by the following reactions:

UNIVERSITY of the
WESTERN CAPE

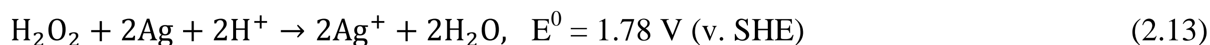

$$H_2O_2 + 2Ag + 2H^+ \rightarrow 2Ag^+ + 2H_2O, \quad E^0 = 1.78\ \mathrm{V\ (v.\ SHE)} \qquad (2.13)$$

$$Si + 4Ag^+ + 6F^- \rightarrow 4Ag + SiF_6^{2-} \qquad (2.14)$$

Net reaction:

$$Si + 2H_2O_2 + 4H^+ + 6F^- \rightarrow SiF_6^{2-} + 4H_2O \qquad (2.15)$$

Reactions (2.13) and (2.14) above show the formation of Ag ions from Ag in which those ions react with Si and nucleate forming new Ag nuclei [2.23]. These chemical reactions add to the reactions that results in SiNWs formation where AgNPs are reduced and sinks down into the Si substrate. Some of these Ag ions will diffuse out without being reduced into Ag, and when these Ag^+ reaches a certain threshold they will start nucleating on the sidewalls of the SiNWs, possibly on the sites where there are high dopants concentration [2.20, 2.21, 2.23]. The nucleation of Ag forming small AgNPs etches the SiNWs on their sidewall leaving nanopores. This nucleation near dopants sites shows also that highly doped Si wafer would

results into porous SiNWs and lightly doped wafer might not produce any pores on SiNWs. The porosity has been found to be high on the top of SiNWs and decrease downwards [2.23].

These reports show that with more oxidant concentration in the etching solution or the etching given more time, the wires grow long and become porous due to faster Si oxidation and dissolution, whereas more oxidant concentration guarantees high concentration of Ag^+ of which some diffuse and etch the nanowire sidewalls. Li *et al.* [2.25] explained the formation of pores in terms of energy bands [2.25]. For heavily doped p-type Si wafer the Fermi level drops down and sits at the same energy as the equilibrium energy of the solution. This forms a Schottky barrier that allows charge transfer (hole or electron) across the interface and that enhances the silicon oxidation and dissolution leading to faster SiNWs synthesis and pore formation. Also differences in H_2O_2 and HF concentrations play a role in terms of oxidation and dissolution of Si, respectively.

2.6 Preferred Etching Directions

UNIVERSITY of the
WESTERN CAPE

Most SEM images in literature show silicon nanowires that are vertically aligned (or perpendicular nanowires with respect to the horizontal surface of the silicon substrate) as synthesised via MaCE, such as the micrograph in Figure 2.5. The nanowires are usually synthesised on Si (100) or Si (111) substrates [2.10, 2.20, 2.21]. Tilted nanowires at certain angles were also produced on starting wafers of Si (110), Si (111) and Si (113) in which the concentration of oxidant played a major role as an effect [2.17, 2.26].

Oxidant concentration such as H_2O_2 or $Fe(NO_3)_3$ has an effect in a way that etching solutions that contains low concentration of oxidant will synthesise nanowires along $\langle 100 \rangle$ direction even if the starting wafer is Si (111) [2.27]. However, it was found that Si (111) etched with solution of high oxidant produced nanowires along $\langle 111 \rangle$ and the same concentration produced nanowires along $\langle 100 \rangle$ for starting wafers of Si (110) and Si (113) [2.17]. The lack of enough oxidant concentration to synthesise SiNWs with an axial direction along $\langle 110 \rangle$ and $\langle 113 \rangle$ for starting wafers of Si (110) and Si (113), respectively, is possibly the answer to the last statement.

Etching direction has been explained in terms of back-bonds strength theory where Si (100) has two back-bonds to the underlying atom and Si (111) has three [2.17, 2.27]. This then means Si (100) will be etched much easier and faster than Si (111) and thus leaving the ⟨100⟩ as the preferred etching direction. Low oxidant concentration will be enough to etch the substrate along ⟨100⟩ where there are less atoms to be removed during oxidation in which that is promoted by an oxidant. Slanted nanowires from specifically Si (111) substrate orientated on the ⟨100⟩ direction has been characterised by a tilt angle of just above 45° which is the known angle between [111] and [100] directions for a diamond like crystal structure [2.27].

It is well documented in literature that vertical SiNWs always follow the direction of the starting wafer, for example nanowires synthesised on the Si (100) and appears perpendicular to the substrate then they grow along the ⟨100⟩ [2.28]. If the nanowires are slanted with respect to the wafer then that means they grow on a different direction as a starting wafer. Synthesis of SiNWs on a Si (100) has been found to be faster than in other wafers of silicon and always produce vertical nanowires when using metal assisted chemical etching technique.

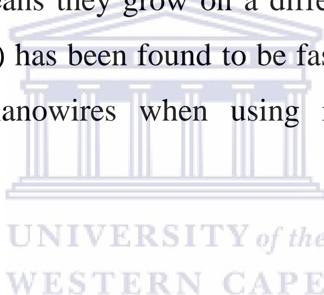
UNIVERSITY of the
WESTERN CAPE

2.7 Properties of SiNWs Synthesised via MaCE

Characteristic properties of each material determine its usefulness, especially nanomaterials as they are intensively researched because of their different properties compared to their bulk counterparts. It is important to study the materials properties as that provides knowledge on their respective applications into different device technologies. For example excellent antireflection properties of vertical silicon nanowires make it eligible to be used in photovoltaics technology. It is expected that when dimensions are reduced for bulk silicon the properties changes too.

2.7.1 Structural Properties

It is important to understand the crystal structure of any material in order to be applied in any technology. X-ray diffraction (XRD) is used to investigate changes in the crystal structure of material mainly bulk material. The XRD studies are usually confirmed with transmission electron microscopy (TEM) for nanostructured material. Razek *et al*. [2.29] performed XRD in their silicon nanowires synthesised by MaCE and they observed Si (100) related peak which confirmed that the nanowires preserved the crystallinity, as the starting wafer was Si (100). They further peeled off SiNWs from the substrate in order to do XRD on the nanowires separately from the Si substrate and again observed the same peak related to Si (100). This crystallinity was also confirmed with TEM studies. Hochbaum and co-authors [2.30] also performed XRD on SiNWs which showed Si (100) peak broadening, which they related to nanoscale crystalline silicon domains as compared to bulk Si.

A wide range of research on the crystallinity of SiNWs has been performed with most studies reporting on the crystalline core of the nanowires [2.17, 2.20, 2.28, 2.29]. As was discussed in Section 2.6 the orientation of planes depends on the starting substrate, usually remains single crystalline and have long range order. Qu *et al*. [2.20] reported that the SiNWs remained crystalline and that the etching did not destroy or change the quality of crystallinity. Selected area electron diffraction studies have also shown good mono-crystallinity as they show spot- and not ring-patterns, which is usually the case for polycrystalline silicon [2.17, 2.20].

2.7.2 Raman Scattering

Raman (scattering) spectroscopy is known to be a non-destructive technique for the characterisation of changes in crystallinity and quantum confinement effects in silicon nanostructures. Most Raman studies usually focus on the c-Si peak at 520 cm^{-1} associated with the Si-Si first order optical phonon mode vibration. The shape of this peak has been found to vary for SiNWs as compared to that of bulk Si due to the reduced dimension. These changes are characterised by a down shift of the wavenumber (frequency) and is accompanied by an asymmetric peak broadening for nanowires [2.31, 2.32].

There are some factors contributing to the down shift or broadening of the c-Si Raman peak. These include phonon confinement, mostly recognised from SiNWs of diameters less than 10 nm and MaCE produces nanowires of diameters usually above that range [2.31]. The phonon confinement effect in terms of shift and broadening was studied by Richter *et al*. and Campbell and Fauchet, known as the RCF model and it predicts the changes (Raman shift and peak broadening) as the diameters are changed for nanowires [2.31]. Piscanec *et al*. [2.31] reported on down shifts of about 10 cm^{-1} for nanowires with diameters of 10 – 15 nm, which contradicts the value of 1 cm^{-1} predicted by the RCF model.

Internal heating has been reported as the other important effect that can cause changes in the shape of the Raman peak at 520 cm^{-1}. This heating effect happens during Raman scattering measurements and is due to high laser power used to scan samples, with down shifts of up to 10 cm^{-1} reported [2.32]. Wang and co-authors [2.33] reported that a laser power of less than 2.5 mW does not induce any internal heating on the nanowires. However, Khorasaninejad *et al.* [2.32] found that even though they increased the laser power to 9.75 mW no changes were observed on the peak shape, signifying no effect of laser power in their nanowires. The group suggested that the nanowires they synthesised via MaCE had higher thermal conductivity than small diameter nanowires in which heating had been observed.

UNIVERSITY of the
WESTERN CAPE

A third factor that affects the shape of the peak (down shift and broadening) is stress induced by thicker layers of SiO_2 covering crystalline core nanowires. A thin layer of SiO_2 can cause a downshift of about 4 cm^{-1} due to tensile stress [2.34]. Wang *et al*. [2.35] reported that a naturally occurring 5 nm thick SiO_2 layer covering SiNWs can cause a down shift of 3 cm^{-1} (from 520 to 517 cm^{-1}) for the c-Si peak due to stress. To confirm their findings SiNWs that were dipped in HF to remove the native oxide layer showed no significant shift as compared to the c-Si peak of bulk Si. A broad peak was reported by Adachi *et al.* [2.36] situated at around 480 cm^{-1} and assigned to amorphous silicon (a-Si) but they also observed a shoulder on the a-Si peak related to the c-Si (520 cm^{-1}).

There are two other visible Raman peaks at about 300 cm^{-1} and a broad peak from 900 – 1000 cm^{-1} observable for SiNWs. The peaks are assigned to second order transverse acoustic at critical point X for 300 cm^{-1} peak and transverse optical at point L for the 900 cm^{-1} peak; these peaks confirm crystallinity [2.32, 2.33]. Light localisation (light trapping) was also probed by Raman scattering, with a group led by Goncher [2.37] reporting on a high intensity

c-Si peak for vertically aligned SiNWs, which they attributed to good light absorption, compared to bulk Si, due to multiple scattering of light within the SiNW array.

2.7.3 Surface Passivation

Fourier transform infrared (FTIR) spectroscopy reveals that as MaCE synthesised silicon nanowires are passivated with oxygen atoms, characterised by a peak around 1050 – 1200 cm^{-1} which is attributed to Si-O-Si vibrations. In a typical FTIR spectrum, there usually are two absorption bands associated with the transverse optical absorption of asymmetric Si-O-Si modes. The appearance of these features in SiNWs is related to the presence of high quality SiO_2 covering the nanowires [2.33]. Leontis *et al.* [2.38] reported on an intentional oxidation of SiNWs using a piranha solution and performed FTIR in comparison with samples dipped in HF for the removal of the oxide layer. The results showed similar degree of oxidation of the Si-O-Si modes, when comparing the two sets of samples. They, however, also observed new peaks from the HF dipped samples at about 626 and 2112 cm^{-1} which they related to Si-H vibrations characterising hydrogen passivation of the Si surface bonds. It was further noted that an increase in the Si-H peak intensity resulted in a decrease in the Si-O-Si peaks which confirms that the hydrogen termination step was successful.

UNIVERSITY of the
WESTERN CAPE

Even though that was a success for short scale investigation, Sun *et al*. [2.39] reported that H-termination cannot work over an extended time frame (days to weeks) as they observed that after some days (26 days) their nanowires were covered with a naturally occurring oxidation. Their samples were dipped in HF after synthesis and FTIR measurements were taken after few minutes, hours and days. These FTIR results showed a reduction in the $Si\text{-}H_x$, where $x = 1, 2$ or 3, (at 2000 – 2200 and ~ 900 cm^{-1}). This reduction was complemented by an increase in the Si-O-Si bonding around 1060 cm^{-1} due to oxidation [2.39].

2.7.4 Optical Reflectance

Less than 4% reflectance was measured for high aspect ratio silicon nanowires over the entire visible regime for nanowires with diameters ranging between 117 and 170 nm [2.29]. Bachtouli *et al.* [2.9] also reported on the difference between bulk Si and SiNWs reflectivity with 25% on average for bulk Si and less than 10% for nanowires measured over the visible range (300 – 1000 nm) reported. Even lower values of up to 1% reflection have been reported

for these vertical orientated SiNWs [2.29]. Ghosh *et al.* [2.40] measured the reflection at single wavelength of 405 nm and obtained 6.3% for nanowires and 42% for bulk Si substrate showing the well reduced reflectivity by the SiNWs. Strong light scattering which results in good light trapping by silicon nanowires has been reported to cause these low reflections as compared to bulk Si wafers.

The reduced dimensions provide elongated optical path lengths for vertical nanowires, which yield good light harvesting [2.29, 2.20]. Razek and co-authors [2.29] attributed the low reflection to the graded refractive index, which is introduced as the middle medium between air and Si substrate. The reflection was reported to decrease with increased nanowires length due to longer optical path length [2.9]. Syu *et al.* [2.41] found a disadvantage of longer nanowires though, where they reported very low power conversion efficiency (PCE) in longer nanowires (5.6 µm) solar cell (3.76%) compared to the one of shorter nanowires (0.37 µm, with PCE of 8.4%). They attributed the problem to shorter minority charge carrier lifetimes and high possibility of carrier recombination due to more surface states caused by high surface area in those longer nanowires. These results show the trade-off between low reflection from longer nanowires and good solar cell performance from shorter ones.

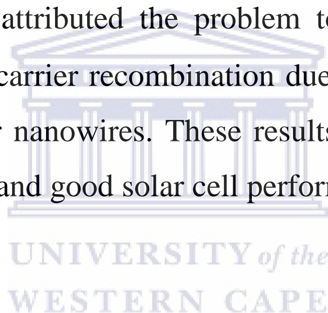
UNIVERSITY of the
WESTERN CAPE

2.8 Experimental Procedure

2.8.1 Solution Preparation

The two-step MaCE process was followed exclusively during the course of this study. All the solution preparations containing hydrofluoric acid (HF) were prepared under a fume hood, with proper protective gear and extraction used for protection against the dangerous HF. For all HF solutions, 5 mol/l molarity concentration (M) yielding a final volume of 50 ml was prepared as follows: 9.065 ml of HF (48% purity, analysed reagent, purchased from Merck Chemicals (Pty) Ltd. Gauteng, South Africa) was slowly added to 12.5 ml deionised water using a micropipette in a Teflon beaker. Then 28.5 ml of deionised water was added to reach a final desired solution volume of 50 ml.

Silver nitrate ($AgNO_3$, ≥ 99% purity, ACS reagent purchased from Sigma – Aldrich, St. Louis, MO, USA) concentrations were varied with concentrations of 5 mM, 20 mM, and 50 mM used to study the changes on the deposited silver nanoparticles while keeping HF concentration at 5 M. For all these $AgNO_3$ concentrations deionised water volume was kept to 50 ml as it was the desired final volumes for all and because the addition of the of $AgNO_3$ salt did not change the final volume of the solution. $AgNO_3$ salt amounts were measured on a sensitive mass scale with masses of 42.5 mg, 170 mg and 425 mg for concentrations of 5 mM, 20 mM, and 50 mM, respectively. Each of these $AgNO_3$ aqueous solutions was mixed with 5 M HF (50 ml) as to make final volumes of 100 ml $AgNO_3/HF/H_2O$ solution and the final solution was stirred slowly.

The etching solution was also prepared with 5 M of HF solution and 0.5 M of hydrogen peroxide (H_2O_2, 30% purity, analysed reagent, purchased from Merck Chemicals (Pty) Ltd. Gauteng, South Africa) solution in different Teflon beakers, with each making 50 ml volumes. HF solution was prepared the same way as explained above. For 0.5 M of H_2O_2 that makes up 50 ml of solution, 2.55 ml H_2O_2 was added into 47.4 ml of deionised water. The two solutions were added together making 100 ml solution of $HF/H_2O_2/H_2O$ again stirred slowly to avoid spilling.

UNIVERSITY of the
WESTERN CAPE

The 0.5 M H_2O_2 concentration of was used for the etching time effect studies and different concentrations of H_2O_2 were investigated and the solution were prepared as shown in Table 2.1 but final volumes were reduced to 25 ml. Some of the values in Table 2.1 were rounded off as it was difficult to accurately measure the amount of water to four decimal digits. The volume of HF solution was also reduced to 25 ml but kept at a concentration of 5 M. To achieve that, 4.53 ml of HF (48%) was added to 6.25 ml deionised water and 14.2 H_2O was then added to make 25 ml of solution. Once again the 25 ml solutions for each H_2O_2 concentrations were mixed with the 25 ml diluted HF making 50 ml $HF/H_2O_2/H_2O$ solutions.

Table 2.1: Different H_2O_2 concentrations with required amounts (in ml) and those of H_2O.

Concentration (M)	H_2O_2 amount (ml)	H_2O amount (ml)
0.05	0.128	24.9
0.1	0.255	24.7
0.5	1.30	23.7
1.5	3.80	21.2
2.5	6.40	18.6
3.5	8.90	16.1
5.0	12.8	12.2

2.8.2 Sample Preparation and Synthesis

The Si substrates (N-type Si (100) test grade, phosphorus doped with a resistivity of 1 – 10 Ω.cm, having thickness of 380 ± 50 µm and diameter of about 7.62 cm (3 inches) and were purchased from Silicon Sense Inc.) were used in this study. Samples were cut into 1 x 1 cm^2 using a diamond pen and were labelled prior the cleaning steps. The cleaning steps involved 10 minutes washing with acetone in an ultrasonic bath, followed by 5 minutes with ethanol to remove contamination. Samples were repeatedly rinsed with deionised water and dipped into a 5% diluted HF for 5 minutes to remove the native oxide layer prior the AgNPs deposition and etching steps. The diluted 5% HF was prepared by adding 5 ml HF (48%) to 50 ml of deionised water which roughly made a 4.8% solution.

After the samples were cleaned and rinsed with deionised water, they were left do dry before the AgNPs deposition step began. Deposition was done for different times in which samples were immersed into a deposition solution ($AgNO_3/HF/H_2O$) one sample at a time. Because deposition times were short samples were held with a Teflon tweezer as to keep deposition time precise; a stopwatch timer was used to record the time of deposition and varied between 15 and 300 seconds at different $AgNO_3$ concentrations. Schematic of the steps is shown in Figure 2.6. The samples were rinsed with deionised water immediately after removal from the solution as to remove extra Ag ion formation on the Si substrate prior to immersion in the etching solution.

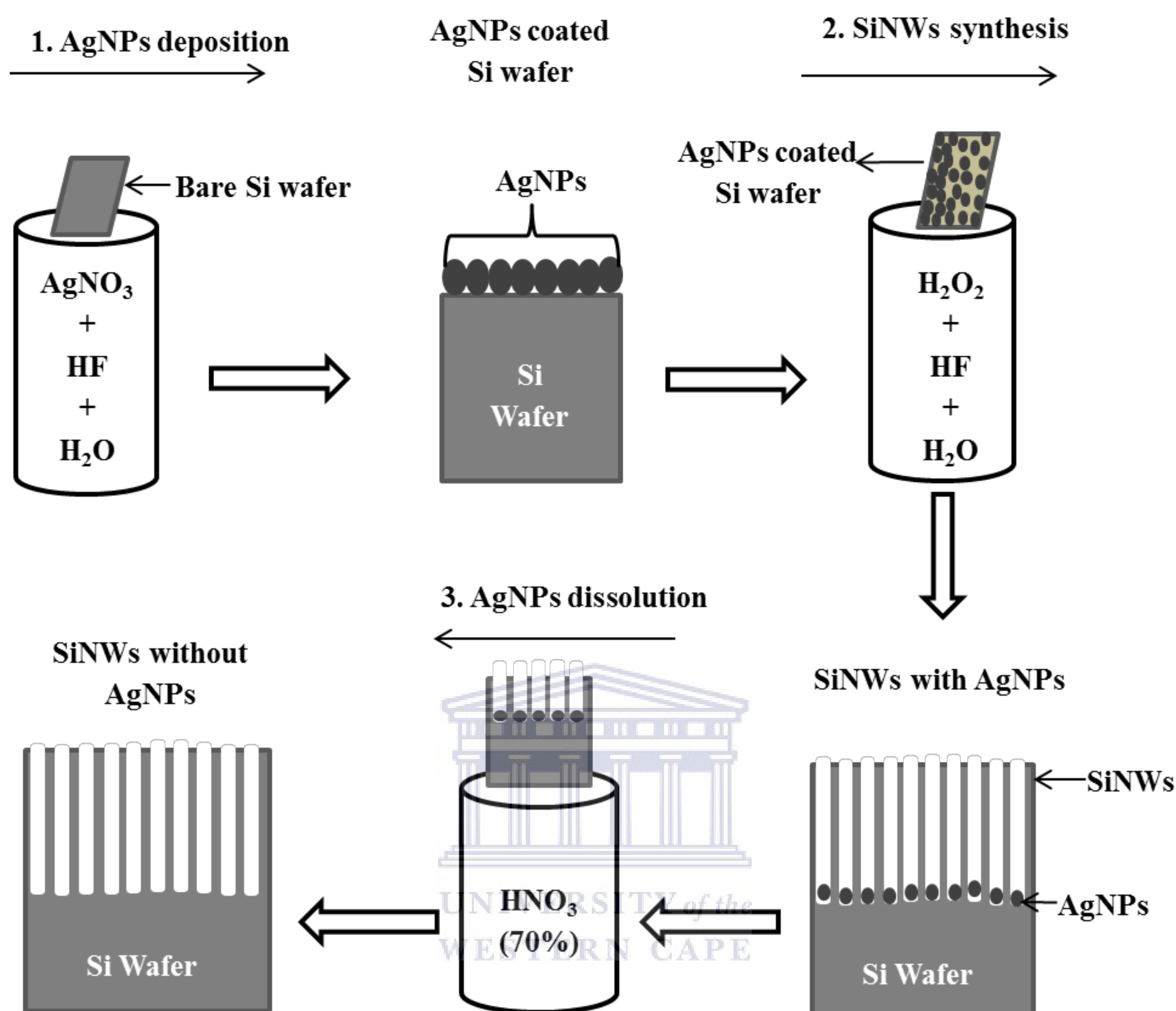

Figure 2.6: Schematic illustration of SiNWs synthesis steps.

The dried AgNPs/Si samples were then immersed into an etching solution of $HF/H_2O_2/H_2O$ at deposition times between 30 seconds and 80 minutes for the investigation of etching time effect. For longer times (5 minutes or greater) samples were placed at the bottom of the beakers for the whole duration of the synthesis. Again after each synthesis samples were rinsed with deionised water, left to dry and were placed on numbered sample holders. Silver nanoparticles were dissolved onto a concentrated nitric acid (HNO_3, 70% purity, ACS reagent purchased from Sigma – Aldrich, St. Louis, MO, USA) which was measured to make 30 ml for an immersion of 15 minutes and the dissolution follows equation (2.10).

References

[2.1] Z. Huang, N. Geyer, P. Werner, J. De Boor and U. Gösele, Advanced Material **23** (2011) 285 – 308.

[2.2] D. Ma, S. Lee, F. Au, Y. Tong and T. Lee, Science **299** (2003) 1874 – 1877.

[2.3] Y. Li, Y. Wu, L. Shi and P. Yang, Applied Physics Letters **83** (2003) 2934 – 2936.

[2.4] Y. Cui and C. Lieber, Science **291** (2001) 851 – 853.

[2.5] B. Ozdemir, M. Kulakci, and H. Unalan, Nanotechnology **22** (2011) 155606 – 155612.

[2.6] V. Schmidt, J. Wittemann, and U. Gösele, Advanced Material **21** (2009) 2681 – 2702.

[2.7] R. Wagner and W. Ellis, Applied Physics Letters **4** (1964) 89 – 90.

[2.8] X. Li and P. Bohn, Applied Physics Letters **77** (2000) 2572 – 2574.

[2.9] N. Bachtouli, S. Aouida, B. Bessais, Microporous and Mesoporous Materials **187** (2014) 82 – 85.

[2.10] Z. Smith, R. Smith and S. Collins, Electrochimica Acta **92** (2013) 139 – 147.

[2.11] F. Bai, M. Li, D. Song, H. Yu, B. Jiang and Y. Li, Journal of Solid State Chemistry **196** (2012) 596 – 600.

[2.12] Y. Liu, G. Ji, J. Wang, Z. Zuo and Y. Shi, Nanoscale Research Letters **7** (2012) 663 – 671.

[2.13] X. Li, Current Opinion in Solid State and Materials Science **16** (2012) 71 – 81.

[2.14] A. Nassiopoulou, V. Gianneta and C. Katsogridakis, Nanoscale Research Letters **6** (2011) 597 – 604.

[2.15] H. Fang, Y. Wu, J. Zhao and J. Zhu, Nanotechnology **17** (2006) 3768 – 3774.

[2.16] K. Peng, J. Hu, Y. Yan, Y. Wu, H. Fang, Y. Xu, S. Lee and J. Zhu, Advanced Functional Material **16** (2006) 387 – 394.

[2.17] K. Peng, R. Zhang, and S. Lee, Advanced Functional Material **18** (2008) 3026 – 3035.

[2.18] Z. Huang, T. Shimizu, S. Senz, Z. Zhang, N. Geyer, and U. Gösele, Journals of Physical Chemistry C **114** (2010) 10683 – 10690.

UNIVERSITY of the WESTERN CAPE

[2.19] M. Lachiheb, N. Nafie, M. Bouaicha, Nanoscale Research Letters **7** (2012) 455 – 459.

[2.20] Y. Qu, L. Liao, Y. Li, H. Zhang, and X. Duan, Nano Letters **9** (2009) 4539 – 4543.

[2.21] M. Zhang, K. Peng, X. Fan, J. Jie, R. Zhang, S. Lee and N. Wong, Journal of Physical Chemistry C **112** (2008) 4444 – 4450.

[2.22] S. Sadrnezhaad, E. Ahmadi and M. Mozammel, Journal of Material Science and Technology **22** (2006) 696 – 700.

[2.23] L. Lin, S. Guo, J. Feng and Y. Wang, Nanoscale Research Letters **5** (2010) 1822 – 1828.

[2.24] J. Jung, H. Um, S. Jee, K. Park, J. Bang and J. Lee, Solar Energy Materials & Solar Cells **112** (2013) 84 – 90.

[2.25] S. Li, W. Ma, Y. Zhou, X. Chen, Y. Xiao, M. Ma, W. Zhu and F. Wei, Nanoscale Research Letters **9** (2014) 196 – 203.

[2.26] S. Wu, T. Zhang, R. Zheng and G. Cheng, Applied Surface Science **258** (2012) 9792 – 9799.

[2.27] C. Chartier, S. Bastide, and C. Levy-Clement, Electrochimica Acta **53** (2008) 5509 – 5516.

UNIVERSITY of the
WESTERN CAPE

[2.28] C. Chen, C. Wu, C. Chou and T. Yen, Advanced Material **20** (2008) 3811 – 3815.

[2.29] S. Razek, M. Swillam and N. Allam, Journal of Applied Physics **115** (2014) 194305 – 194313.

[2.30] A. Hochbaum, D. Gargas, Y. Hwang and P. Yang, Nano Letters **9** (2009) 3550 – 3554.

[2.31] S. Piscanec, M. Cantoro, A. Ferrari, J. Zapien, Y. Lifshitz, S. Lee, S. Hofmann and J. Robertson, Physical Review B **68** (2003) 241312 – 241315.

[2.32] M. Khorasaninejad, J. Walia and S. Saini, Nanotechnology **23** (2012) 275706 – 275712.

[2.33] R. Wang, G. Zhou, Y. Liu, S. Pan, H. Zhang, D. Yu and Z. Zhang, Physical Review B **61** (2000) 16827 – 16832.

[2.34] S. Toda, T. Oishi, T. Yoshioka and T. Okuno, Japanese Journal of Applied Physics **49** (2010) 095002 – 095008.

[2.35] Z. Wang, X. Chen, Q. Yan and J. Zhang, Europhysics letters **100** (2012) 14002 – 14005.

[2.36] M. Adachi, M. Anantram and K. Karim, Nano Letters **10** (2010) 4093 – 4098.

[2.37] K. Gonchar, L. Golovan, V. Timoshenko, V. Sivakov and S. Christiansen, Bulletin of the Russian Academy of Sciences: Physics **74** (2010) 1712 – 1714.

[2.38] I. Leontis, A. Othonos and A. Nassiopoulou, Nanoscale Research Letters **8** (2013) 383 – 389.

[2.39] X. Sun, S. Wang, N. Wong and S. Lee, Inorganic Chemistry **42** (2003) 2398 – 2404.

[2.40] R. Ghosh, P. Giri, K. Imakita and M. Fujii, Nanotechnology **25** (2014) 045703 – 045716.

[2.41] H. Syu, S. Shiu and C. Lin, Solar Energy Materials & Solar Cells **98** (2012) 267 – 272.

UNIVERSITY of the
WESTERN CAPE

CHAPTER THREE

Analytical Techniques

3.1 Introduction

A scanning electron microscope (SEM) was employed in this work to study the structural features such as the length, diameter, surface topology and morphology of the resulting Ag nanoparticle film and SiNW array. Energy dispersive x-ray spectroscopy (EDS) was used to investigate the elemental composition, whereas further investigation of the structure and crystallinity of the nanowires were done using a transmission electron microscope (TEM). The crystal structure of the bulk layer of nanowires was investigated with x-ray diffraction (XRD) and Raman scattering (RS) with surface bonding investigated using Fourier transform infrared spectroscopy (FTIR). Lastly ultra-violet visible (UV-Vis) spectroscopy was employed to study the optical properties, in terms of reflectivity, in both specular and diffuse reflection modes. This chapter will give a background of the underlying physics of these techniques and the practical operation of the instruments used to obtain the results reported in this study.

UNIVERSITY of the
WESTERN CAPE

3.2 Scanning Electron Microscopy

3.2.1 Introduction

The SEM was developed due to limitations in resolving images obtained from optical microscopes, which has a resolution limit of about 200 nm. The major advantage of SEM is the wavelength of electrons used, ranging between 0.01 and 0.001 nm, compared to light microscopy operating at wavelengths of 400 to 700 nm. During scanning electron microscopy, image resolution down to 1 nm is attainable. In addition SEM can provide images in three-dimensions with information about the topography and morphology of solid materials [3.1].

The operation of a SEM begins with the electron source (or gun) situated on top of the instrument column, as shown in Figure 3.1. The electrons are produced from a tungsten thermionic filament, or field emission gun (FEG) which provides higher resolution and has become a more preferred source. These electrons are accelerated at high energies ranging between 1 and 30 keV. The charged electron beam is accelerated towards the anode and further de-magnified by two or more electromagnetic condenser lenses to reach a specific diameter as it hits the specimen (sample). In between these condenser lenses there are condenser apertures and coils which are used to control the convergence angle of the beam. The lower most condenser lens, often called objective lens, provides the final spot size of the beam and determines the brightness of the image by controlling its intensity [3.1, 3.2].

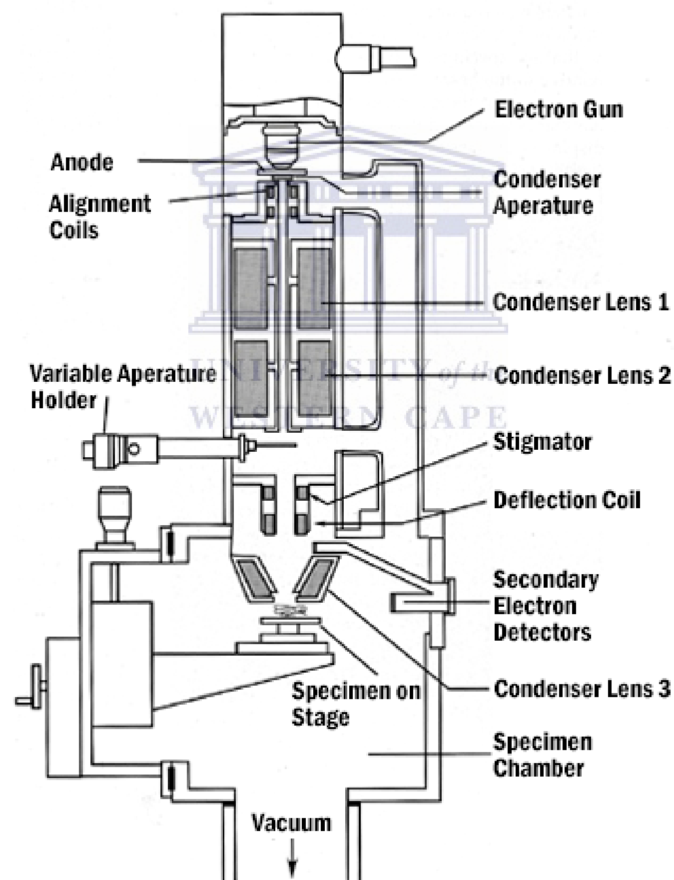

Figure 3.1: Schematic representation of scanning electron microscope diagram [3.2].

3.2.2 Resolution

Resolution is defined as the ability to resolve two entities or spots separately through a microscope. There are limits on the resolution than can be achieved in an SEM. When the beam of electrons passes through the lenses and apertures, it will diffract, forming cones seen as discs on a 2-D screen, called Airy dicks or rings. The limit of resolution limit (d_r) was theoretically explained by a German optician, Ernst Abbe, with the following mathematical relation [3.1, 3.2]:

$$d_r = \frac{0.61\,\lambda}{\mu \sin \alpha} \quad (3.1)$$

where λ is the illumination wavelength, μ is the refractive index of the medium between the object and the objective lens, and α is the aperture angle. The product $\mu \sin \alpha$ is known as the numerical aperture. The formula can be used to work out the theoretical limit of any microscope where λ can be reduced and μ increased (usually 1 in a vacuum) or α increased to achieve better resolutions. However, these factors cannot be changed above different boundaries like a different medium with high refractive index would be required such as oil, aperture angle has an upper limit of 90° and there would be a limit for electron beam wavelength [3.2].

UNIVERSITY of the
WESTERN CAPE

3.2.3 Depth of Field and Working Distance

Depth of field (DOF) in a microscope is described as the range of positions in which the image does not lose sharpness, even when the specimen is changed and depends on the resolution of the microscope. DOF can be controlled by an aperture of the objective lens and the working distance, which is the distance between the surface of the specimen and the objective lens (lower lens). The working distance and the aperture determine the beam size which strikes different thicknesses of the specimen surface. Figure 3.2 shows that short working distance and bigger apertures will result into small DOF and longer working distances and small aperture result into large depth of field. Different values of DOF are often used for various interests during the study of different specimen. Shorter working distances and appropriate aperture are required when the interest is to operate at higher resolution and these conditions result into small depth of field. For the study of rough surface specimens, which require high DOF, longer working distances and smaller apertures are used [3.1, 3.3].

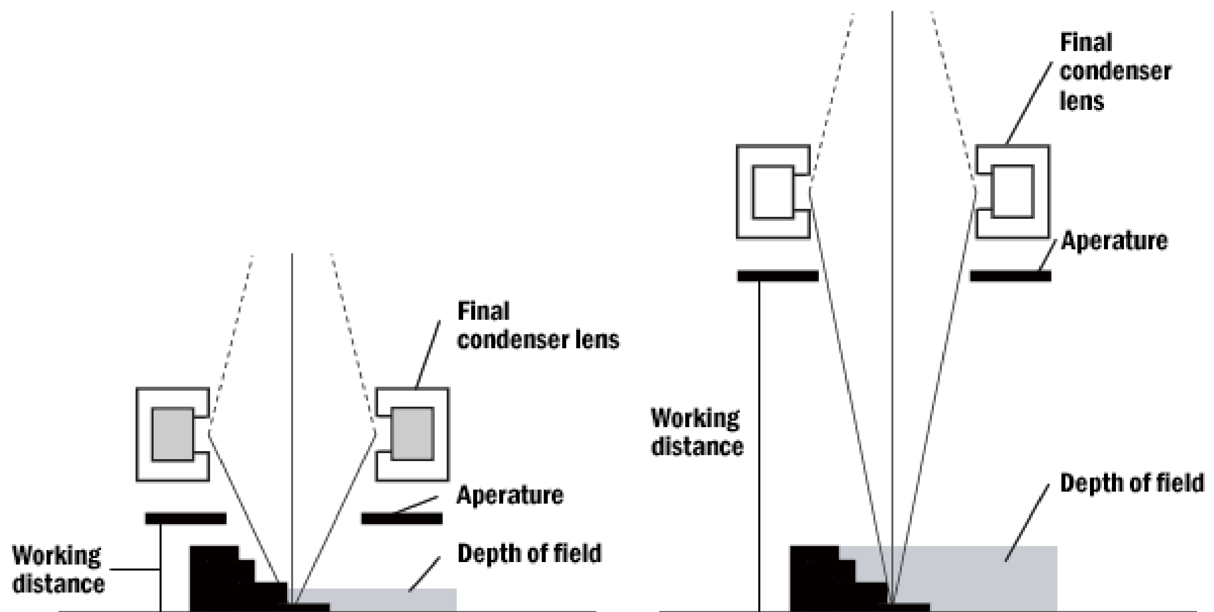

Figure 3.2: Schematic representation for the relation between depth of field, working distance and aperture [3.2].

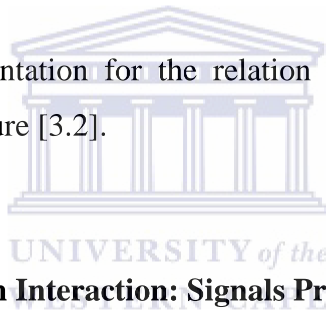
UNIVERSITY of the
WESTERN CAPE

3.2.4 Electron Beam-Specimen Interaction: Signals Produced

When the electron beam interacts with the specimen within the SEM two processes take place, namely elastic and inelastic scattering. Elastic scattering is an event where only the trajectory of the electron beam is affected but their energy does not change by much within the specimen (about 1 eV is transferred to the specimen compared to 10 keV of incident beam). Elastic scattering happens between the incoming beam and the atoms of the specimen together with their cloud of electrons and the interaction depends mainly on the atomic number of the scattering atom [3.1]. In inelastic events the energy of the beam is transferred to the atoms and electrons of the specimen during interaction. Most of the primary electron's (incident electron beam) kinetic energy will be lost as heat during inelastic scattering and a small part of the energy will escape as x-rays, light or secondary electrons and all these are important for imaging and analysis in SEM.

During interaction of the primary electron beam and specimen there are different signals that maybe important for characterisation in the SEM and those are secondary electrons,

backscattered electrons used for imaging in SEM and x-rays signal for chemical composition studies. Other signals are low energy Auger electrons, which may be easily absorbed and would require specialised equipment for their use and the last one is cathodoluminescence. Transmitted electrons are used in transmission electron microscopy, as will be discussed later in this chapter. All these signals are shown in Figure 3.3.

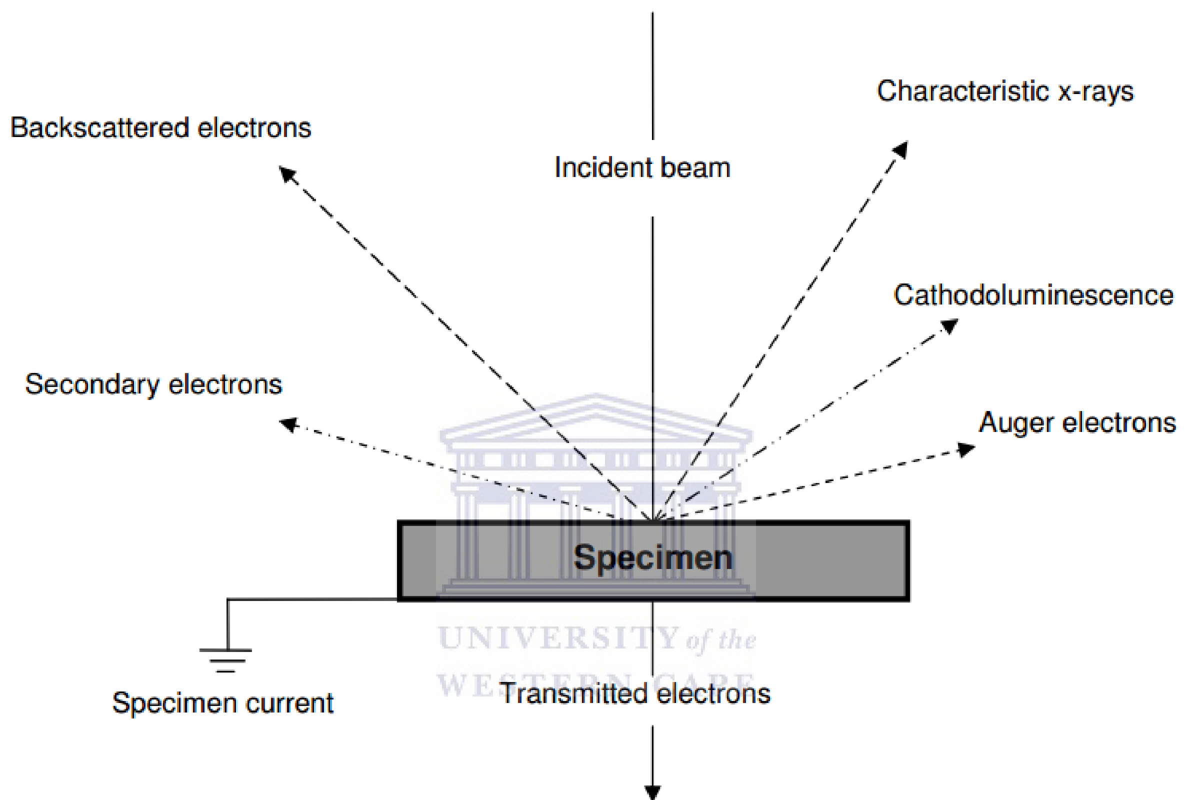

Figure 3.3: Schematic illustration of different signals produced during electron beam – specimen interaction [3.1].

The electron beam penetrates the specimen in a manner known as interaction volume where different radiations are generated as a result of inelastic scattering as shown in Figure 3.4. Different specimens will generate different types of radiations and only the radiation escapes from the specimen will be detected. X-rays are not easily absorbed and thus will escape the specimen and because of this large amount of the interaction volume (several micrometres) will contain x-ray signal. Backscattered electrons will be detected if they penetrated less than a fraction of a micrometre and thus this signal will originate from a smaller region than x-ray signal. Secondary electrons have energies less than 50 eV and are generated by the incident

electrons escaping the specimen and low energy backscattering electrons. Secondary electrons originate from a small region of the interaction volume, a region just bigger than the incident electron beam diameter. Secondary electrons originate from a small sampling volume and thus give better spatial resolution than other signals. Penetration depths for each signal are shown in Figure 3.4.

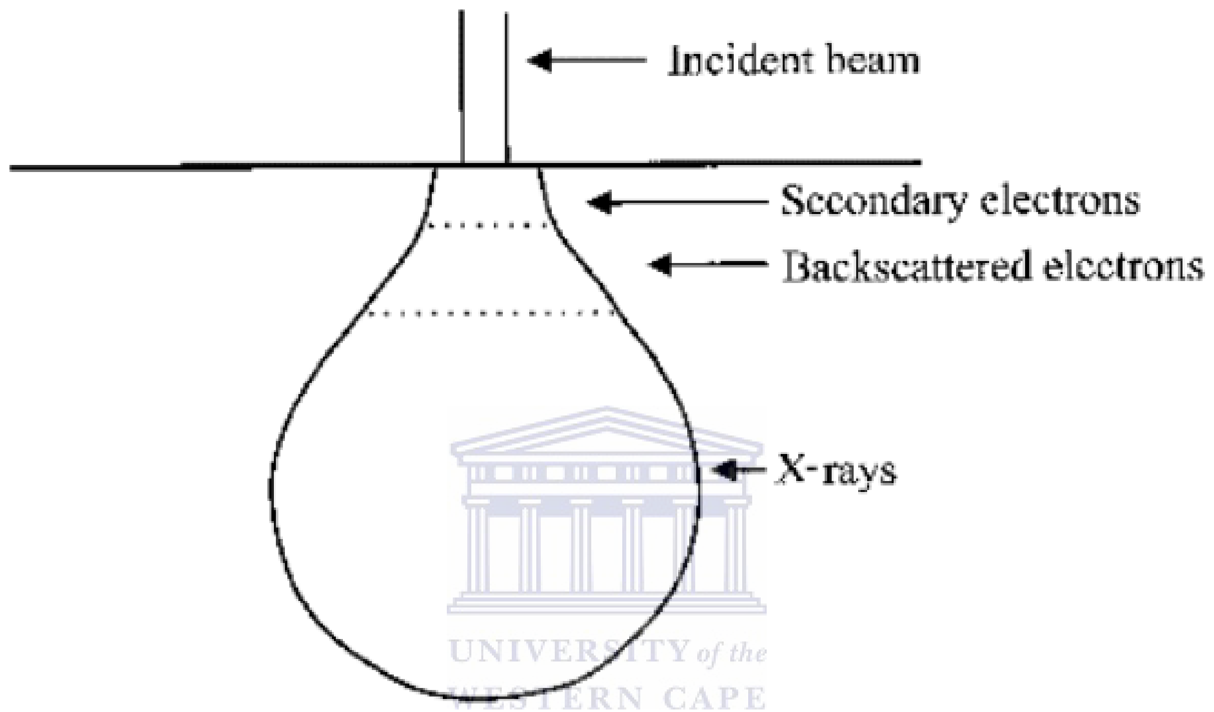

UNIVERSITY of the
WESTERN CAPE

Figure 3.4: Schematic representation of different signals as they originate within the interaction volume [3.1].

3.2.5 Detecting Secondary and Backscattering Electrons

The most common signal used in modern SEM instruments comes from secondary electrons, which are used for imaging purposes as they provide better spatial resolution. These electrons are detected by a photomultiplier system which is known as the Everhart-Thornley detector. Secondary electrons are captured by a phosphor scintillator which goes through conversion from electrons to light and light to electrons via photomultiplier the finally amplified and used to modulate the intensity of the cathode ray tube. Secondary electrons are accelerated to excite the scintillator because of their low energy (10 – 50 eV) and are further collected by a

metal grid in the detector for better resolved image. Everhart-Thornley detector is a very efficient system and can collect almost all secondary electrons from a flat specimen [3.1].

Few backscattering electrons travelling at the right direction will hit the scintillator of the Everhart-Thornley detector and thus the signal obtained for secondary electrons might contain few backscattering electrons. Even though this process happens there are detectors in SEM instrument specialising on the collection of backscattering electrons. These detectors include scintillator detectors, solid state detectors, and through the lens detector and each has its advantage over the other [3.1].

3.2.6 Characteristic X-ray and Energy Dispersive Spectroscopy

X-ray signals are generated when electron beam of enough energy (several keV) hits the specimen. The signal is mainly used for chemical composition studies in the SEM and that is one of the important information acquired from the instrument equipped with x-ray detector. Qualitative analysis can be obtained from this signal where characteristic x-ray wavelength emitted by a specimen gives information about different types of elements present in the specimen. Quantitative analysis is also possible where a number of different x-ray types emitted per second provide information about the quantity of elements present in the specimen.

UNIVERSITY of the
WESTERN CAPE

When an incident electron beam strike an atom in the specimen a localised electron in the inner shell of the atom (K shell in Figure 3.5) will be kicked out from an atom leaving an atom in an excited high energy state. An electron from an outer shell (L shell) will fill in the empty (vacant) space in the inner shell and an atom will relax giving off a certain energy which is greater than that of incident beam energy as shown in Figure 3.5. The emitted energy correspond to a characteristic x-ray wavelength and this energy is the difference of the two excited states (L and K states) and these energies vary for different atoms giving information about the elements present on the specimen [3.1, 3.2].

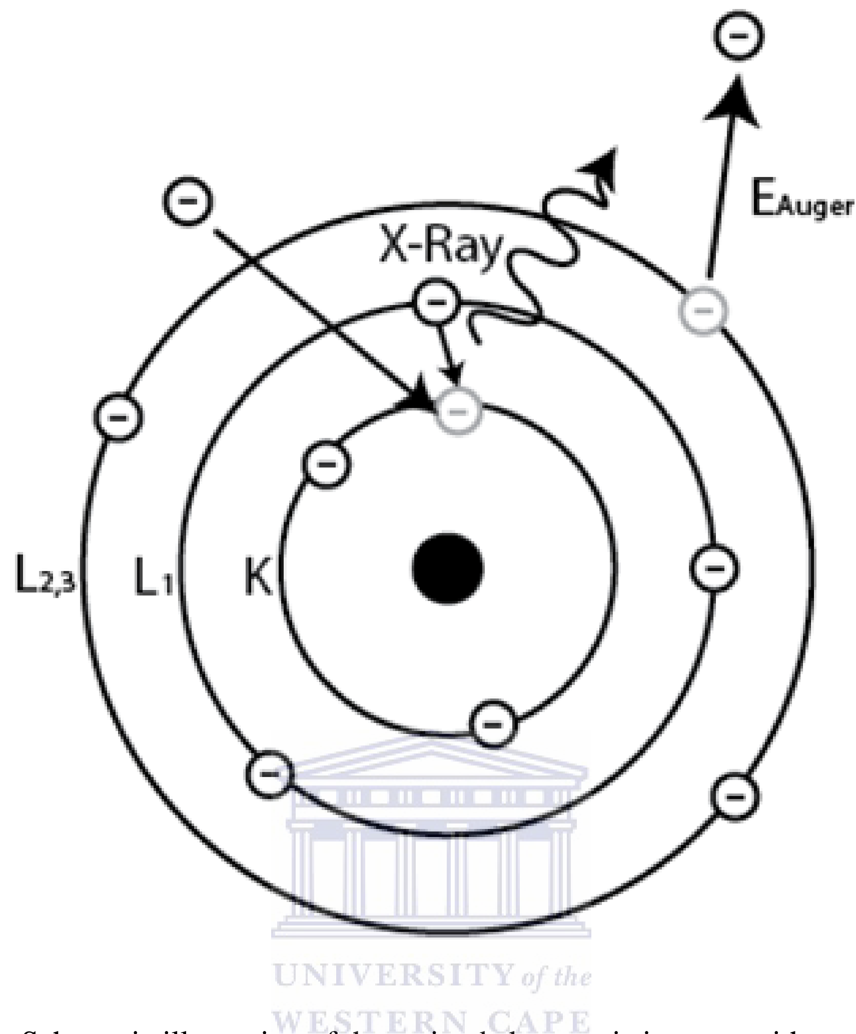

UNIVERSITY of the
WESTERN CAPE

Figure 3.5: Schematic illustration of the emitted characteristic x-ray with an atom [3.1].

Characteristic x-rays can be detected with wavelength dispersive spectrometer which measures accurately the wavelength and energy of the x-ray and alternatively, modern SEMs use energy dispersive spectrometer (EDS) detection systems but these are associated with loss of precision and resolution. EDS detector consist of a piece of semiconductor material (silicon or germanium) held in a position where many x-rays emitted by a specimen will fall on it. The detector is required to be close to the specimen and be in the line of sight of the specimen for efficient collection. It is within the detector where x-rays are converted into measurable signals which form the EDS spectra. In modern SEM instruments EDS detectors can measure energies up to boron in which that include detection of oxygen which often covers silicon nanowires [3.1, 3.2].

3.2.7 Sample Preparation and Data Acquisition

In order to obtain effective images in SEM the specimen is required to be electrically conductive to increase the collection of secondary and backscattered electrons. To satisfy this requirement, non-conducting or low conductive specimen are coated with a thin highly conductive layer of gold or carbon which is done via sputter coating or thermal evaporation. When the electron beam hits the specimen there is a build-up of charge which may damage the specimen. For non-conductive specimen (biological specimen) this build-up of charge results into an effect known as charging and may degrade the resolving power producing low quality image. If the specimen is conducting the effect is insignificant as the charge will be conducted through the specimen and eventually grounded by contact with the specimen stage [3.3].

Silicon nanowires (SiNWs) and silver nanoparticles (AgNPs) samples in this study were coated with carbon using carbon sputter coater. The coating was done using an Emitech K950X Sputter Coater and the samples were investigated in top view for surface morphology and topology and cross sectional view for morphology in terms of length for SiNWs. The images were taken with Zeiss Auriga field-emission gun scanning electron microscope (FEG-SEM), hosted by the Electron Microscope Unit within the Department of Physics of the University of the Western Cape. The instrument is equipped with an Oxford Instruments X-Max solid state silicon drift detector (SDD) for EDS measurements. The SEM was operated at working distance of about 5 mm with a specimen stand that can be manually adjusted up and down; an accelerating voltage of 5 and 20 kV was used for imaging and EDS measurements, respectively.

UNIVERSITY of the
WESTERN CAPE

3.3 Transmission Electron Microscopy

3.3.1 Introduction

The TEM was the first electron microscope to be developed in the 1930's by Knoll and Ruska [3.4]. The instrument though, first provided information for materials scientists in the 1950's where thin metal foils were studied. Modern TEMs are now used to study materials at

atomic scale, nanomaterials at a range of 1 to 100 nm, micrometre scale and beyond [3.4]. Modern TEMs have the capability to directly image atoms in crystalline specimens at resolutions close to 0.1 nm, which is smaller than the interatomic distance, whereas an electron beam can be focused to a diameter smaller than 0.3 nm allowing for qualitative analysis of nano-materials like SiNWs. As the name suggests the most important signal in a TEM originate from the transmitted electrons, shown in Figure 3.3. Transmission of these electrons thus requires a thinner specimen for good imaging. TEMs operate at very high accelerating voltages, typically ranging from 40 to 200 kV, and beyond. High resolution TEM (HR-TEM) is being operated nowadays with a fraction of a nanometre resolution and these instrument can provide information about atomic planes in a thin material or specimen. Other valuable information obtainable in TEM is the crystal structure of the material via electron diffraction, chemical composition via EDS and electron energy loss spectroscopy (EELS).

In addition to what was shown in Figure 3.1 for schematic of a typical SEM, a TEM consists of more lenses sitting below the specimen, a viewing screen and a camera at the bottom of the microscope column, as shown in Figure 3.6. The electrons are produced from the filament, accelerated down and controlled by the condenser lenses and apertures which both controls the beam diameter before it hits the specimen. Another important part in the instrument is the specimen chamber which contains the objective lens, objective aperture and the objective stigmator coils. The sample is inserted in to the objective lens using a specimen holder and can be moved for several millimetres and tilted at different angles for different investigations. The objective lens below the specimen forms the first intermediate image and diffraction patterns, which are enlarged by the projector lens and viewed on the display screen as shown in Figure 3.6. The intermediate lens and projector lens are used to control the magnification of the image. A charge coupled device (CCD) camera records the image [3.1, 3.2].

Some of the operational principles of TEM were discussed during the description of the operation principle of a scanning electron microscope in Section 3.2 above, e.g. the depth of field and some of the signals that can be obtained. Similarly, elemental composition can also be accurately extracted during TEM, however, with a smaller probe size.

UNIVERSITY of the WESTERN CAPE

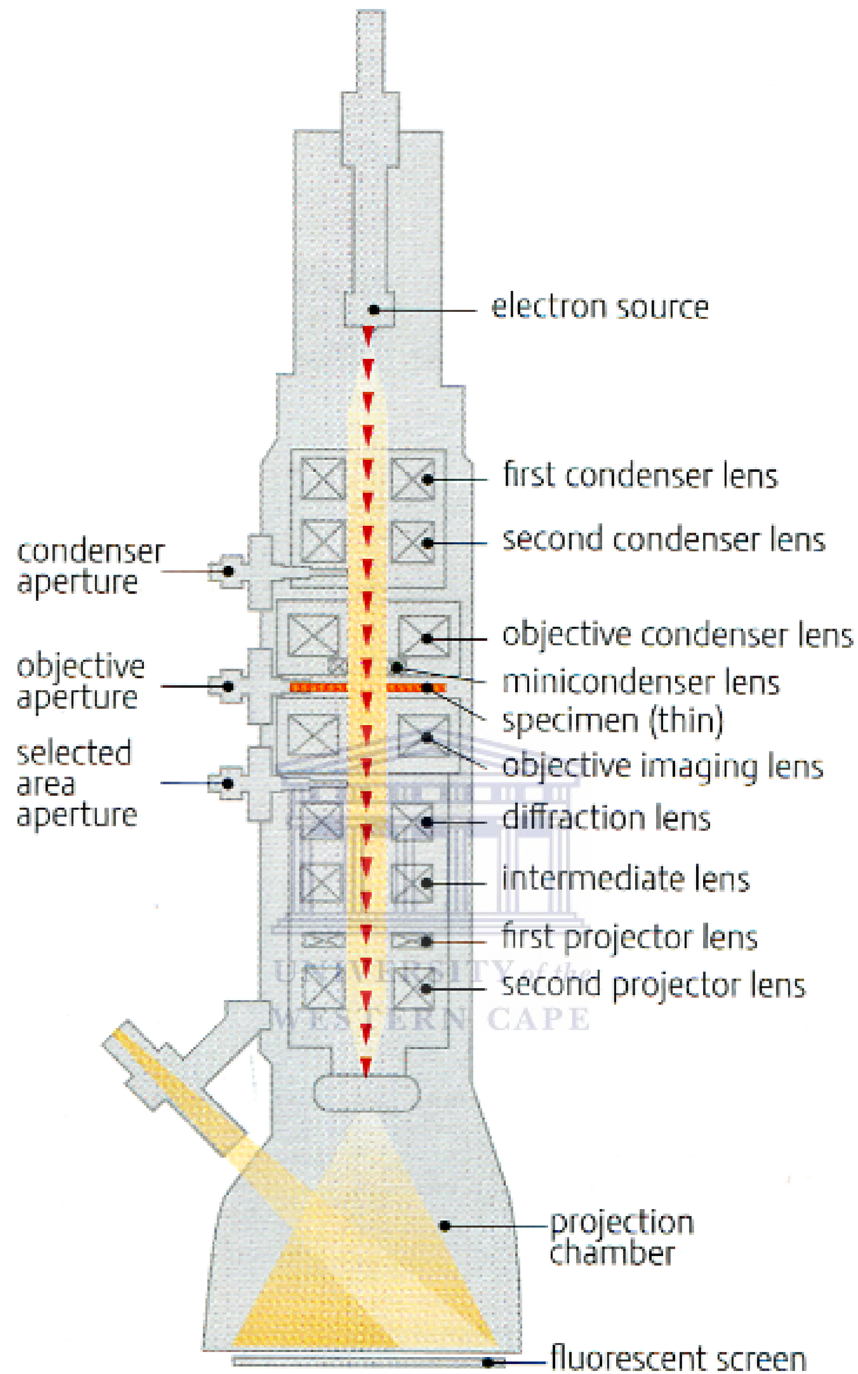

UNIVERSITY of the
WESTERN CAPE

Figure 3.6: Schematic illustration of TEM column and its important parts [3.4].

3.3.2 Electron Beam-Specimen Interaction in Transmission Electron Microscopy

As was mentioned earlier, only transmitted electrons in TEM are used to acquire an image and therefore this subsection will look in to their interaction with the thin specimen, typically

100 nm or less. The transmitted electrons can be elastically scattered, which will be deflected into wide angles upon interaction with the nuclei of specimen atoms. These scattered electrons suffer a small loss in energy and the number of electrons scattered may give information about the atomic number within the specimen. Electrons may also be scattered inelastically where they lose a significant amount of energy during interaction and provide information about elemental composition. Alternatively, electrons may encounter no energy loss or deflection and these can easily be separated from inelastic scattering via an energy analyser [3.2].

If, however, all these electrons are involved in image formation in the TEM, then all the regions of the specimen (i.e. with different thicknesses) will look the same in the image, thereby producing an image with no contrast. An image with contrast can thus be formed if the elastic and inelastic scattered electrons are separated and that aspect is controlled by an objective aperture which stops some and allows some electrons through for imaging. If the aperture is positioned in the middle of optical axis and there is no specimen then a bright background will be observed and the effect is known as bright field imaging. In the presence of a thicker and denser specimen the electrons will be deflected at wider angles and these regions will appear darker in the image. The aperture can be displaced and used to select some deflected beam and without a specimen the background will appear dark resulting into dark field imaging and this effect needs to be avoided in TEM as it induces aberrations resulting in bad images. As mentioned before, if the aperture is removed all primary transmitted electrons will go through and contribute in the image and no contrast will be obtained and the image will look bright [3.1].

UNIVERSITY of the
WESTERN CAPE

3.3.3 Electron Diffraction

Valuable information in TEM about crystal structure of the material is obtainable where high energy electrons penetrate a thin specimen, leaving finger prints about diffraction planes. The way electrons interact with the material is similar to x-rays and light because electrons have wave-particle duality behaviour and thus electron diffraction can be explained in a similar way as x-ray diffraction, first explained by Bragg and commonly known as Bragg’s law [3.1, 3.4].

In Figure 3.7 an interaction of electron beam with a perfect crystal is shown with all atoms lie in a cubic crystal. If a beam of electrons with in-phase waves hit the atoms in the crystal and scattered waves (electrons) are also in-phase with one another after hitting for example atoms A and B in Figure 3.7 then these will strengthen up forming a strong electron beam. If the scattered waves are out of phase then they will fade out. If the path length of the waves in D (refers to Figure 3.7) differs by an integral number of wavelengths then the scattered waves will be in phase. This condition will be satisfied if $CB + BE = n\lambda$ where n is the integer number and λ is the wavelength of electrons and mathematical observations show that $BE = CB = d \sin \theta$ in Figure 3.7 where d is the space between atomic planes (interplanar spacing) as shown in the figure. This leads to Bragg's Law [3.1, 3.4]:

$$2d \sin\theta = n\lambda \tag{3.2}$$

The above equation suggests that only electrons that have been elastically scattered at Bragg angle θ will be emerging from the specimen [3.1]. The integer number n is usually 1, 2, 3, etc., but for electron diffraction it is considered to be one where the first order of diffraction ($n = 1$) is used. Also for electron diffraction the wavelength of electrons is very short (λ = 0.0037 nm) and d-spacing for most materials is usually small and thus these results into small diffraction angles where $\sin \theta \approx \theta$. For first order diffraction and small Bragg angles equation 3.2 becomes:

UNIVERSITY of the WESTERN CAPE

$$2d\theta = \lambda \tag{3.3}$$

This makes the electron diffraction much more easily compared to x-ray diffraction which works with large diffraction angles. As already mentioned that diffraction angles are very small in electron diffraction and so strong diffraction will result from atomic planes that are almost parallel to the incident beam. Interplanar spacing can also be calculated via this equation:

$$d_{hkl} = \frac{a}{\sqrt{h^2+k^2+l^2}} \tag{3.4}$$

provided that lattice parameter "*a*" of a cubic crystal is known and the diffracting planes *(h k l)* are known where *(h k l)* is the system used for Miller index of planes [3.1, 3.4].

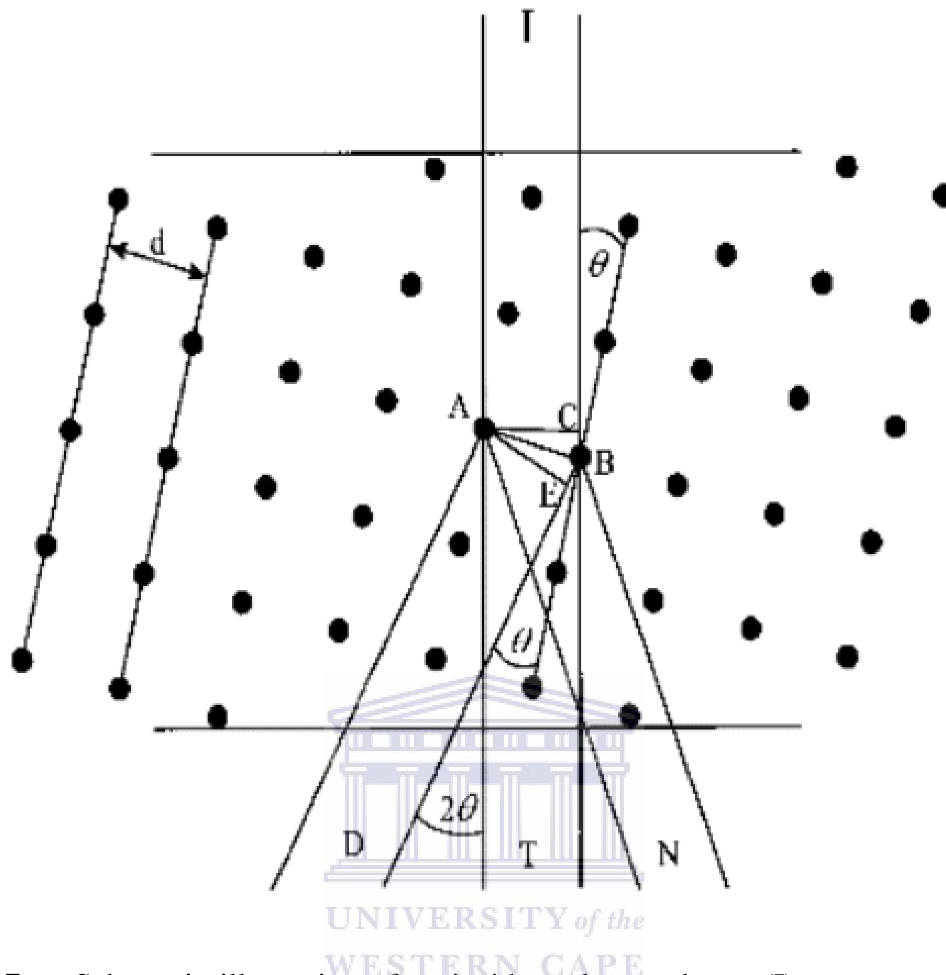

UNIVERSITY of the
WESTERN CAPE

Figure 3.7: Schematic illustration of an incident electron beam (I) on an array of atoms separated by *d*, the beam may be diffracted (D and N) or not diffracted (T) [3.1].

3.3.4 Electron Diffraction in the Transmission Electron Microscope

An incident electron beam on a crystalline specimen will have some electrons passing through without any interaction and hit a screen of distance *L* away from the specimen as shown in Figure 3.8. Some electrons will be diffracted at 2θ angle by crystal planes having interplanar spacing *d*, hitting the film at A situated at distance *r* from O (Figure 3.8), thus by geometry of small diffraction angles:

$$\frac{r}{L} = 2\theta \qquad (3.5)$$

And combining equation (3.3) and (3.5) and rearrange gives:

$$rd = L\lambda \tag{3.6}$$

The term $L\lambda$ is known as the camera constant since the camera length, L, and the wavelength, λ, do not depend on the specimen. The relation in (3.6) shows that with a known camera constant the interplanar spacing d can be obtained by measuring the distance between the diffracted spot and un-diffracted one which is r. In the relation (3.6) d is inversely proportional to r and that means big r will result into small d-spacing [3.1, 3.2, 3.4].

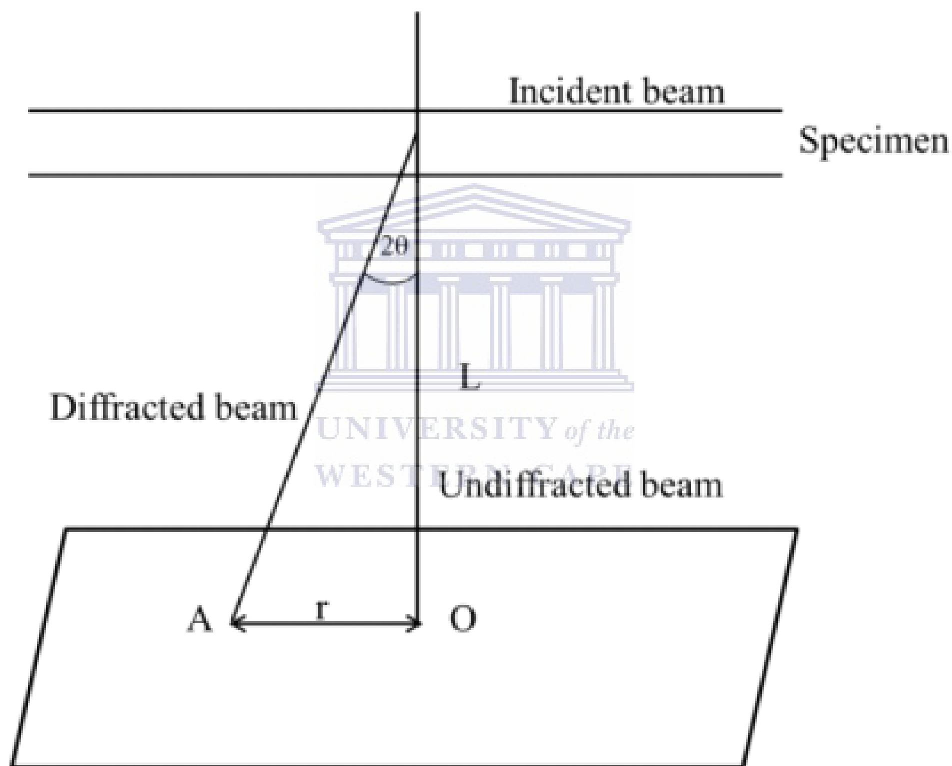

UNIVERSITY of the WESTERN CAPE

Figure 3.8: Schematic representation of diffraction pattern formation in TEM [3.1].

The formation of a diffraction pattern in a TEM is different from the way an image is formed. Shown in Figure 3.9 is the diagram of illustrating transmitted electron beams as they leave the specimen. The rays that have single arrow from AA' will pass through D' and ones with two arrows will pass through D before all form an image in BB' as shown in Figure 3.9. All the rays leaving the specimen will have a corresponding point in the DD', the back focal plane of the objective lens. Another set of points will be formed in EE' when the rays pass

through the second projector lens. A diffraction pattern from these rays will thus be formed in DD' or EE' where as the micrograph will be formed in CC' if the viewing screen is placed in these positions. This lens system is there to magnify and enlarge the diffraction patterns and can alternatively be switched to image the specimen and projecting the diffraction pattern [3.1].

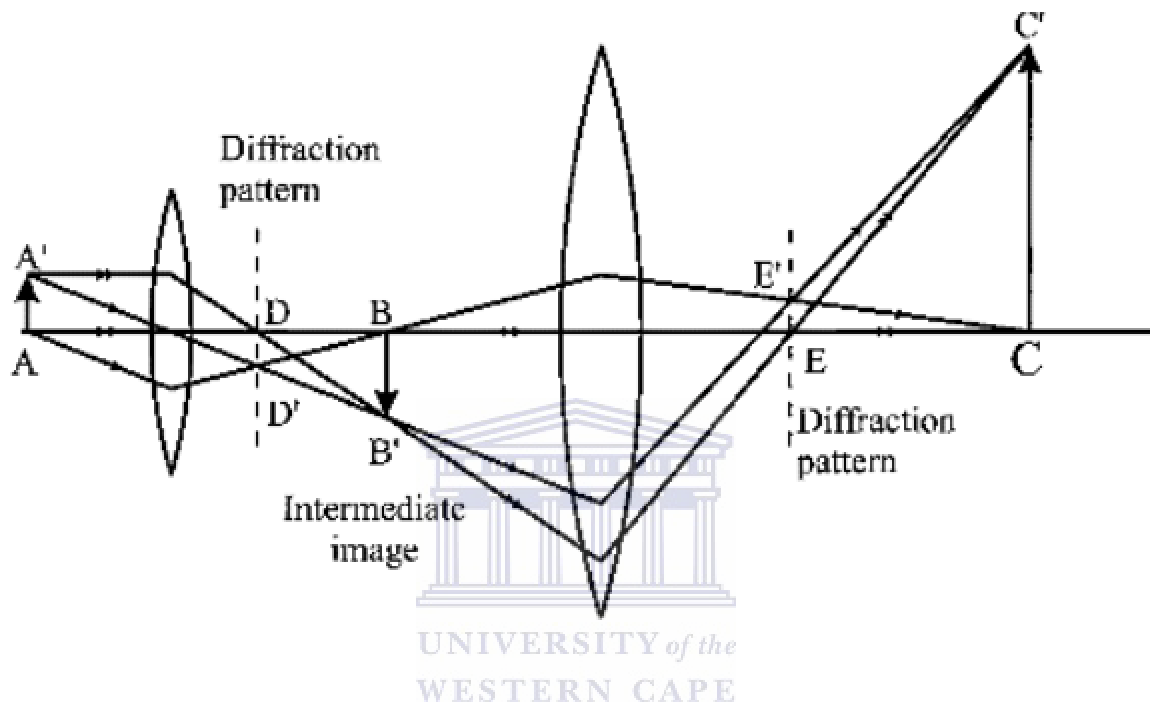

UNIVERSITY of the
WESTERN CAPE

Figure 3.9: Schematic illustration of diffraction pattern formation in positions DD' and EE' or formation of a micrograph in CC' [3.1].

Diffraction patterns that have been observed with TEM are usually spots patterns arranged in a periodic array and spots forming rings of different diameters. Different spots of certain distances away from the un-diffracted spot usually situated in the middle of the pattern represent different set of planes available in the crystal. This type of pattern presented by spots comes from single crystal material or specimen and d-spacing for each set can be measured to index those planes. Consequently the patterns that form rings are associated with polycrystalline material or specimen and different diameters of those rings represent different planes in the material. TEM probe with a small diameter and thus can measure one crystal in polycrystalline material providing information about that small selected area and thus the diffraction in TEM is referred to as selected area electron diffraction (SAED) [3.1, 3.2, 3.4].

3.3.5 Structure Factor

Another important aspect of electron diffraction or any diffraction (x-ray diffraction) is the structure factor, which leads to some planes of the crystal appearing bright and some faint. The structure factor is related to the diffraction amplitude by [3.1, 3.4]:

$$A_{hkl} = F_{hkl} A_0 \tag{3.7}$$

A_{hkl} in (3.7) is the diffracted amplitude; F_{hkl} is the structure factor for (*h k l*) planes and A_0 the amplitude of the diffracted electron beam. The structure factor is made up of all the electron scattered by each atom in the plane in a unit cell with same scattering wave phase (in-phase waves) and is given by this equation [3.1, 3.4]:

$$F_{hkl} = \sum_{j=1}^{n} f_j(\theta) exp\left[-2\pi i\left(hu_j + kv_j + lw_j\right)\right] \tag{3.8}$$

The summation is for atom 1 to n, f_j is the scattering factor for the jth atom with atomic coordinates u_j, v_j, and w_j, the exponential factor controls the phase of each scattered wave and θ is the scattering angle between the incident beam and the scattered beam. The structure factor is controlled by selection rules where some planes with Miller index (*h k l*) will give rise to diffraction and some will not and this depends on the structure of the cubic system i.e. simple cubic, body-centred cubic (bcc), face-centred cubic (fcc) or diamond cubic structure. These selection rules state, for example, in fcc crystal structures only the planes with all even or all odd Miller indices (*h k l*) will give rise to diffraction e.g. (1 1 1), (2 2 0), (3 1 1), (4 2 0), etc. and the rest will not e.g. (1 0 0), (3 2 1), etc. For a bcc structure selection rules says if the summation of the Miller indices (*h k l*) i.e. ($h + k + l$) gives an even number then the planes will result into diffraction e.g. (1 1 0), (3 1 0), (2 2 0), etc. and if the sum give an odd number then there would be no diffraction e.g. (1 1 1), (2 1 0) etc. This then shows that by knowing the material one can predict what type of diffraction will be obtained from TEM [3.1, 3.4]. The theory of structure factor also applies to x-ray diffraction which will be discussed in the next section.

3.3.6 Sample Preparation and Data Acquisition

TEM requires thin samples in order for electrons to pass through. As such, during this work, the vertically aligned silicon nanowires were scratched off the Si substrate using a razor blade and dispersed in a 5 ml ethanol. This solution was then agitated in an ultrasonic bath, as to disperse the array of nanowires in the ethanol. This solution was then drop-casted onto a 3 mm holey carbon coated copper grid, which was then inserted into the instrument for analysis. All results were obtained using a Tecnai $G^2$20 field emission gun transmission electron microscope (FEG-TEM) operated at 200 kV, hosted at the Electron Microscope, UWC. This instrument is fitted with an EDAX detector for EDS analysis. This EDS detector system differs from the Oxford Instruments' SDD set-up used in the Auriga SEM, in that it is a lithium doped Si (Si:Li) detector, which is cooled using liquid nitrogen. The Tecnai system is also equipped with a Fischione high angular annular dark field (HAADF) detector, which was used to obtain dark field images during scanning transmission electron microscopy (STEM) studies of the SiNWs. In particular, STEM mode was used to obtain STEM-EDS maps of the SiNWs before and after HF treatment during this work.

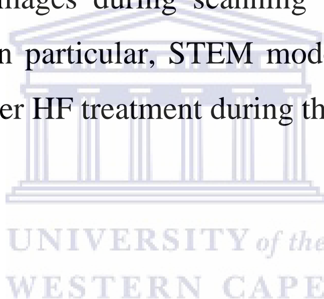

UNIVERSITY of the
WESTERN CAPE

3.4 X-ray Diffraction

3.4.1 Introduction

X-rays are high energetic electromagnetic radiation with similar propagation as visible light but because of their high frequency (short wavelength) they are not visible with a naked eye. This type of radiation was discovered by a German physicist W. Roentgen in 1895. X-rays used in diffraction have wavelengths of 0.5 – 2.5 Å (1 Å = 1×10^{-10} m) and this correspond well with interplanar spacing (d-spacing), introduced during TEM discussion. X-rays are generated when an electron of sufficient kinetic energy decelerate upon heating a target material. Structures of different crystals will scatter the incoming x-ray waves resulting in constructive or destructive interference patterns. Crystals in materials have three-dimensional periodic arrays of atoms or molecules in space, however, other patterns with no order are called amorphous. When a crystal containing regular repeating arrays of atoms is irradiated by a mono-chromatic x-ray beam, it generates a unique fingerprint in the form of diffraction

peaks [3.5]. X-ray diffraction in this study is used to investigate the crystal structure of SiNWs compared to the bulk wafer of Si and this is done by studying the diffraction peaks.

3.4.2 Crystal Structure and Bravais Lattices

Figure 3.10 (a) shows an illustration of a three dimensional periodic array of atoms arranged in a crystal; the cube shown Figure 3.10 (b) represents a unit cell. Each point in the lattice represents an atom or molecule and is identical to the other surrounding atoms. The configuration of atom or molecule is referred to as a lattice point and the whole crystal in Figure 3.10 (a) a point lattice. A unit cell shown in Figure 3.10 (b) is formed by three translational vectors $\vec{a}$, $\vec{b}$, and $\vec{c}$ and these vectors have lengths a, b, and c with angles between the vectors being α, β, and γ. These lengths and angles are known as lattice parameters or constants, and can vary, resulting in different shapes of unit cells, which in turn results in different point lattices. Only seven kinds of unit cells are possible, giving seven different crystal systems; because there are more requirements for point lattices, where each point must have an identical surrounding, it turns out that there are fourteen point lattices. These are known as Bravais lattices and are illustrated in Table 3.1 [3.5].

UNIVERSITY of the
WESTERN CAPE

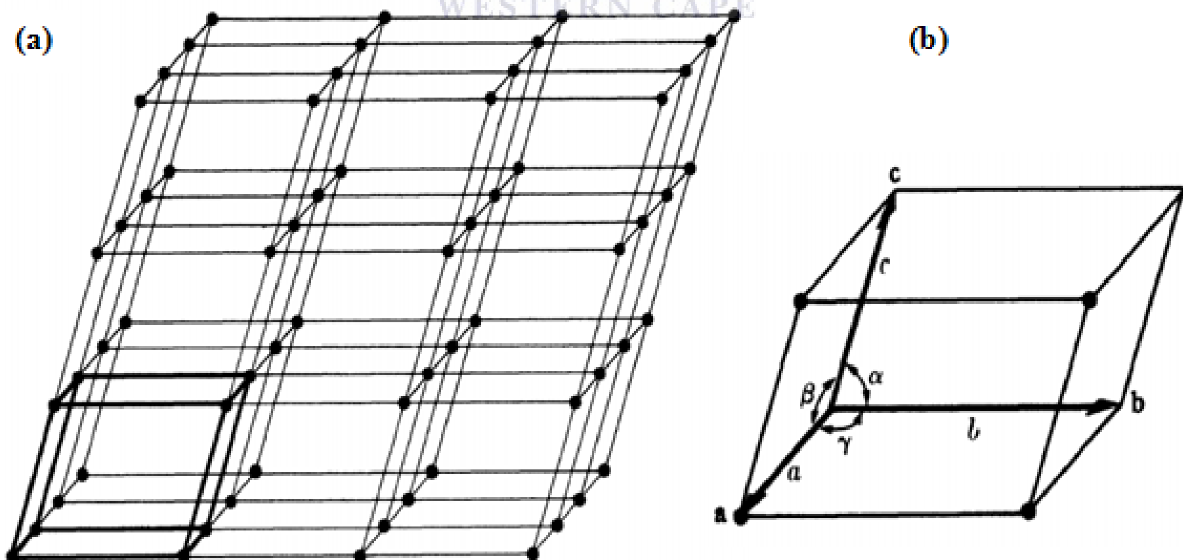

Figure 3.10: Schematic illustration of (a) point lattice and (b) the unit cell [3.5].

Table 3.1: Descriptions of seven crystal systems and fourteen Bravais lattices [3.5].

System	Axial length and Angles	Bravais lattice	Lattice symbol
Cubic	3 equal axis at right angles $a = b = c$, $\alpha = \beta = \gamma = 90°$	Simple Body-centred Face-centred	P I F
Tetragonal	3 axis at right angle, 2 equal $a = b \neq c$, $\alpha = \beta = \gamma = 90°$	Simple Body-centred	P I
Orthorhombic	3 un-equal axis at right angles $a \neq b \neq c$, $\alpha = \beta = \gamma = 90°$	Simple Body-centred Base-centred Face-centred	P I C F
Rhombohedral (Trigonal)	3 equal axes, equally inclined $a = b = c$, $\alpha = \beta = \gamma \neq 90°$	Simple	P
Hexagonal	2 equal co-planar axes at 120°, 3rd axis at right angles $a = b \neq c$, $\alpha = \beta = 90°$, $\gamma = 120°$	Simple	P
Monoclinic	3 unequal axes, one pair not at right angles $a \neq b \neq c$, $\alpha = \gamma = 90° \neq \beta$	Simple Base-centred	P C
Triclinic	3 unequal axes, unequally inclined and none at right angles $a \neq b \neq c$, $\alpha \neq \beta \neq \gamma \neq 90°$	Simple	P

UNIVERSITY of the WESTERN CAPE

The unit cell vectors shown in Figure 3.10 (b) can describe any point in the lattice which is given by a linear combination of the crystallographic axes [3.5]:

$$\vec{r} = u\vec{a} + v\vec{b} + w\vec{c} \tag{3.9}$$

where *u*, *v*, and *w* are the coordinates of any vector in the lattice represented by $\vec{r}$. These vector coordinators can be simplified by writing any point in a lattice using the form [u v w]. Furthermore, [u v w] need to be converted to a set of smallest integers, for example [2 2 0] and [$\frac{1}{2}$ $\frac{1}{2}$ 0] both represents the same direction with a common preferred notation of [1 1 0].

Directions related by symmetry in a lattice are known as directions of a form or family of directions and have certain notation according to Miller indices *h k l*. Directions of [1 0 0], [0 1 0], [0 0 1], [$\bar{1}$ 0 0], [0$\bar{1}$0], and [0 0 $\bar{1}$] all belong to $\langle 100 \rangle$ family of directions where a negative direction is represented by a bar index.

The symmetry of crystals results in crystal planes labelled as (*h k l*), which are also important in x-ray diffraction. Similarly planes that are related by symmetry are called planes of a form and are denoted by $\{h\ k\ l\}$. Planes of one family have the same d-spacing but have different indices. For example, the faces of a simple cube, (1 0 0), (0 1 0), (0 0 1), ($\bar{1}$ 0 0), (0 $\bar{1}$ 0) and (0 0 $\bar{1}$) belong to a family of planes {1 0 0}. Planes of Miller indices (*h k l*) in a unit cell will intercept the crystal axis *a, b* and *c* and thus the notation for that will be (*a/h b/k c/l*) but the reciprocal is chosen such that *(h/a k/b l/c*) is used instead to give proper Miller indices of planes [3.5].

3.4.3 Bragg's Law of Diffraction by Crystals

UNIVERSITY of the
WESTERN CAPE

If an incident beam of in-phase x-rays hits an array of stacked planes in a crystal with interplanar spacing *d*, then some x-rays will be transmitted through the crystal and some in-phase x-rays will be scattered at angle θ_B known as the Bragg angle, the illustration of this is shown in Figure 3.11. The scattered x-ray waves will combine and form a diffracted beam if their path difference forms an integer multiple of wavelengths such that CA + AD = $n\lambda$, *n* is the integer and λ is the x-ray wavelength and result into a following mathematical expression:

$$2d\ \sin\theta_B = n\lambda \tag{3.10}$$

Equation (3.10) is known as the Bragg's law of x-ray diffraction and gives the angle θ_B at which a set of planes (*h k l*) of spacing d constructively reflects x-rays of wavelength λ in the nth order as observed from Figure 3.11 [3.5]. For cubic crystals or systems shown in Table 3.1 the d-spacing is related to lattice constant "*a*" and Miller indices of planes (*h k l*) by this equation:

$$a = d_{hkl}\ \times \sqrt{h^2 + k^2 + l^2} \tag{3.11}$$

Equation (3.11) is important for the calculations of lattice parameter from d_{hkl} that is obtainable from XRD measurements [3.5].

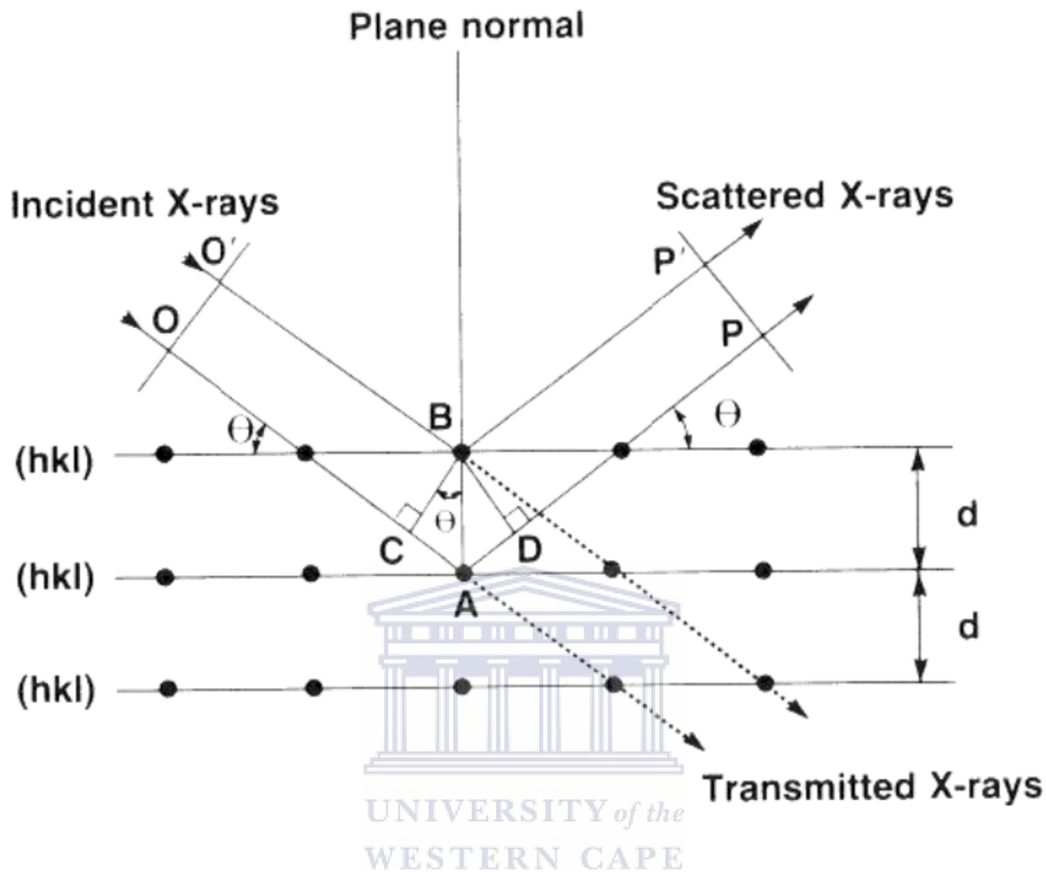

UNIVERSITY of the
WESTERN CAPE

Figure 3.11: Schematic of Bragg's interpretation for the interaction of x-rays with atomic planes in a crystal [3.5].

3.4.4 The X-ray Diffractometer

The illustration of how x-ray diffraction is performed from interaction with the sample to the detection of the signal is shown in Figure 3.12. The instrument is called an x-ray diffractometer and consists of three basic parts, an x-ray source (positions S and T), diffractometer circle and the detector system (G and E) all as shown in Figure 3.12. Detector G is placed on the circumference of a circle centred at the sample stage, C. The sample is supported by a table H, which can rotate about an axis, O, coming out of the page as shown in the figure. X-rays diverge as they leave their source at S directed towards the sample. After interaction with the sample in C these x-rays will be diffracted and form a converging

diffracted beam. The diffracted x-ray beam is focused by the slit in F before it can be detected at G. The carriage in E supports the slit and the detector and also rotates about the axis O and has an angular position 2θ in which its position can be read on the scale in K. The supports E and H are mechanically locked in a θ – 2θ relationship such that when the detector rotates at 2θ the sample automatically rotates at θ. The slits A and B are there to define and collimate the incident and diffracted beams, respectively. A filter is placed in the diffracted beam-path to stop the K_β radiation in which K_α is the preferred radiation and to decrease the background radiation originating in the sample. All the discussion is based on Figure 3.12 [3.5].

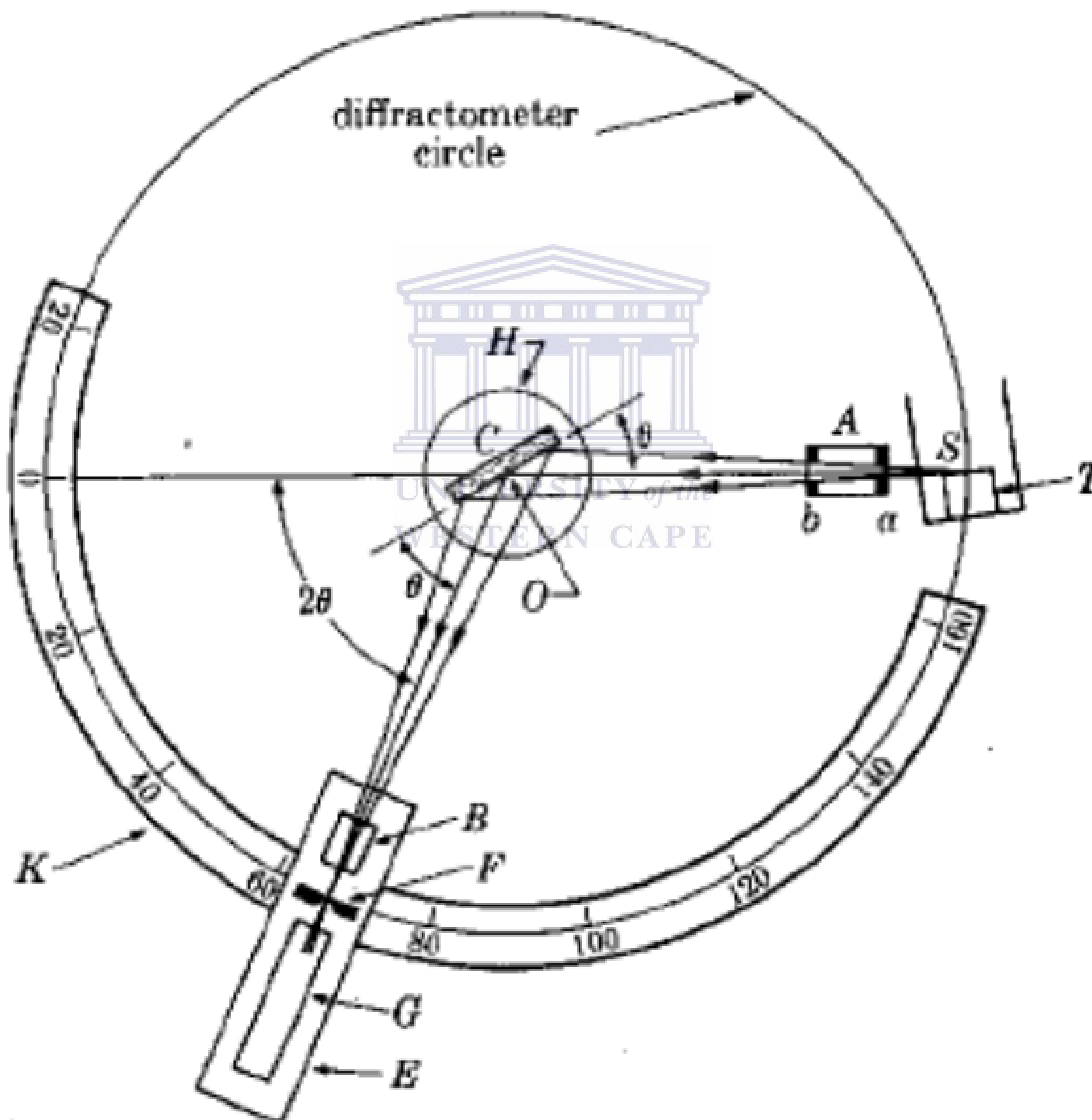

UNIVERSITY of the WESTERN CAPE

Figure 3.12: Schematic representation of x-ray diffractometer operational principles [3.5].

3.4.5 Data Acquisition and Sample Preparation

XRD is used to investigate structural evolution in materials, crystal or amorphous and this technique can give valuable information about structural changes in SiNWs. XRD measurements were performed on SiNWs and bulk silicon samples for comparison with samples sizes of 1 x 1 cm^2 using a PANalytical X'Pert Pro diffractometer at the Council for Scientific and Industrial Research (CSIR), South Africa.

Measurements were taken at room temperature with a 2θ scan range from 10° – 90° and angular scan step size of 0.026°. Copper (Cu) K-alpha 1 ($K\alpha_1$) was used with a wavelength of 0.1540 Å as x-ray source, operated at a voltage and current of 45 kV and 40 mA, respectively. The divergent slit was fixed at 0.38 mm to ensure that the measured spot was less than the sample size of about 1 x 1 cm^2.

UNIVERSITY of the
WESTERN CAPE

3.5 Raman Spectroscopy

3.5.1 Introduction

Raman spectroscopy has proven to be a valuable technique to study nanostructured material effectively and non-destructively. Vibrational phonon frequencies, line-width and intensities can provide information about chemical bonding and structural properties of these nanomaterials and any crystalline deviation from their bulk counterparts can be studied with this technique. Raman spectroscopy is about the interaction of radiation with molecules of the material giving fingerprints about the molecular vibration frequencies. Raman spectroscopy is a two photon inelastic scattering event where the incident photon with high energy than the vibrational quantum energy of the molecule, loses part of its energy to the molecular vibration and the remaining energy get scattered as a photon with reduced frequency [3.6].

3.5.2 Theory of Raman Spectroscopy

When monochromatic radiation of certain frequency is incident on the material there scattering of radiation with a different polarization as the incident radiation. The scattered

radiation might have the same frequency as the incident radiation referred to as Rayleigh scattering or it might be different and those are known as Raman scattering events. Raman scattering with scattered frequencies less than that of the incident radiation are referred to as Stokes shift and those with higher scattered frequencies as anti-Stokes shift. These events are shown in Figure 3.13 where a molecular vibrating system is considered with ground and an excited states *m* and *n*, respectively, as shown. Rayleigh or elastic scattering results from the transitions that start and end at the same vibrational energy level, ground or first excited states. The Stokes Raman scattering result from a transition that begins from the ground state and ends at the excited state and anti-Stokes Raman starts at the excited state and finishes at the ground state as depicted in Figure 3.13. Out of all these processes Rayleigh scattering is the most intense one because most photons scatter this way and the next probable event will be Stokes and then anti-Stokes [3.6, 3.7].

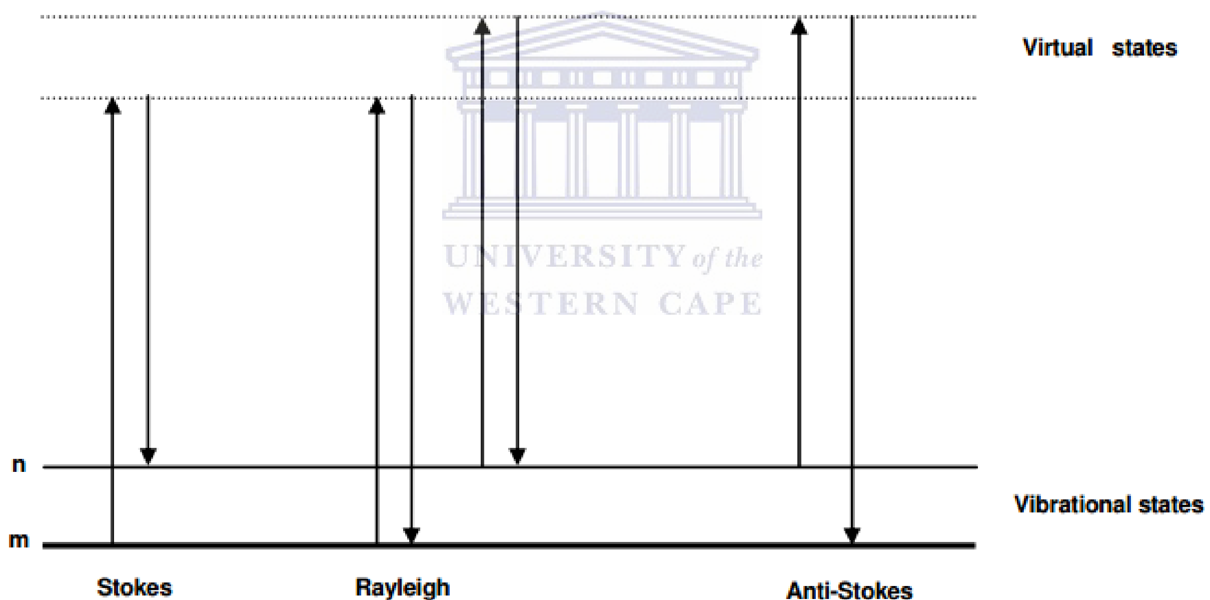

Figure 3.13: Illustration of the scattering events, Rayleigh, Stokes and anti-Stokes [3.6].

Raman spectroscopy involves molecular vibration in materials and these vibrations can be explained with Hooke's law. If two atoms in a molecule can be imagined as two balls and the chemical bonds between these atoms as massless springs then the vibration follows Hooke's law as shown in Figure 3.14. This law relates the restoring force, F of the atoms to the displacement, x from their equilibrium position via this relationship [3.7]:

$$F = -kx \tag{3.12}$$

where k is the spring constant in *N/m* and measures the strength of the bond between the connected atoms. The atom-and-bond (ball-and-spring) model is known as the simple harmonic oscillator and the vibrational frequency is classically given by:

$$f_0 = \frac{1}{2\pi}\sqrt{\frac{k}{m}} \tag{3.13}$$

where *m* is the reduced mass of the atoms in shown in Figure 3.14 and given by:

$$m = \frac{m_1 m_2}{m_1 + m_2} \tag{3.14}$$

UNIVERSITY of the
WESTERN CAPE

Figure 3.14: Representation of a ball-and-spring model for diatomic molecule [3.7]

Wavenumber "q" is commonly used in Raman spectroscopy instead of frequency or wavelength because it holds an advantage of being linear with the energy. Wavenumber has the reciprocal units of wavelength i.e. cm^{-1} and is related to frequency by this relationship:

$$q = \frac{1}{\lambda} = \frac{f}{c} \tag{3.14}$$

where λ is the wavelength, *f* the frequency and *c* is the speed of light in vacuum given by $3 \times 10^8\ m/s$ [3.7].

3.5.3 Raman Characterisation of Silicon Nanowires

The Raman scattering spectroscopy is used to study structural changes in Si which can be crystalline or amorphous. The most studied vibrations are those from Si-Si bonds which set a peak at 520 cm^{-1} related to crystalline silicon (c-Si) as shown in Figure 3.15. This peak is caused by first order optical phonon vibrations at the centre of Brillion Zone (BZ) i.e. wave-vector $\mathbf{q}$ = 0 and due to active transverse optical (TO) and longitudinal optical (LO) phonon vibrations at critical Γ-point (TLO (Γ)) [3.8, 3.9]. The amorphous peak is usually observed at about 480 cm^{-1}.

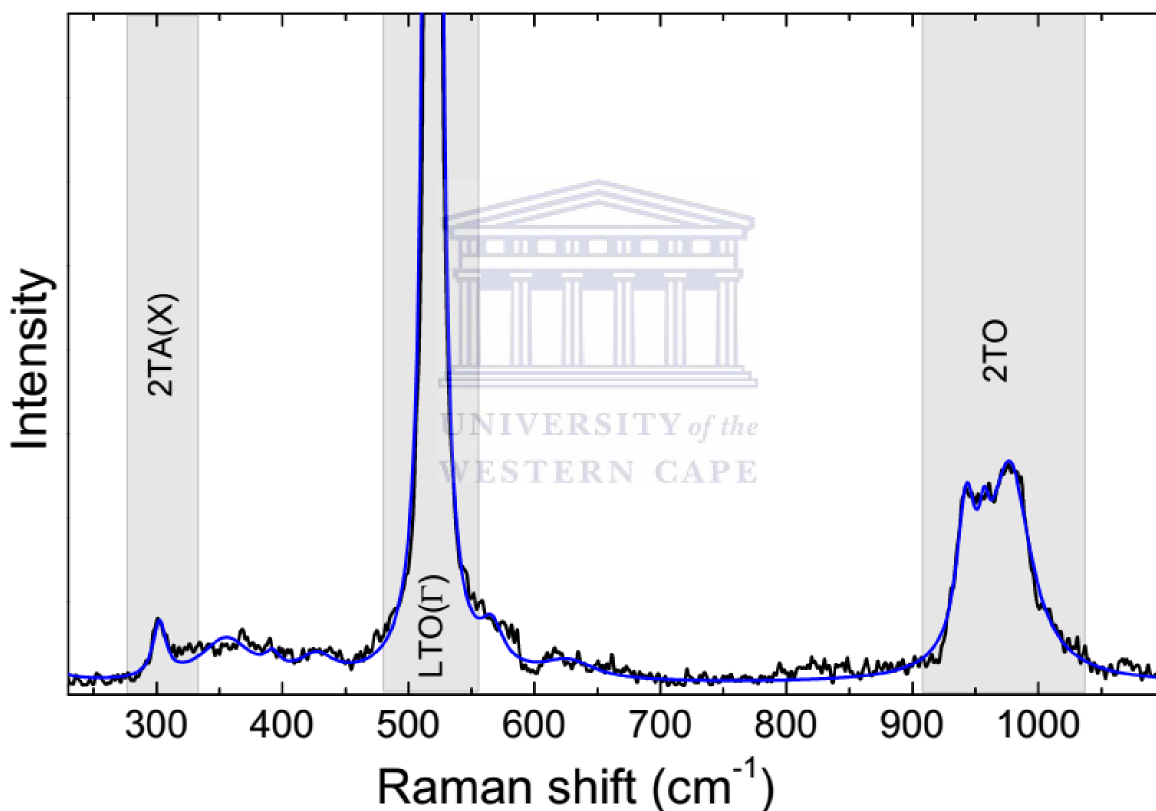

UNIVERSITY of the
WESTERN CAPE

Figure 3.15: A typical Raman spectrum of bulk Si illustrating main peaks [3.9]

The shape of the c-Si peak changes for Si nanostructures (SiNWs) as compared to that of bulk Si. These changes are usually related to quantum confinement and some to structural disorder. These changes are due to the fact that the momentum selection rule of Raman scattering is relaxed for nanomaterials. This relaxation allows phonons that are far away from the BZ centre to contribute to the phonon vibration of the first order Raman scattering. From

the confinement model derived by Richter et al. and Campbell and Fauchet known as the RCF model the peak position and full width at half maximum (FWHM) of the c-Si changes as the nanostructure (dots and wires) dimensions reduces.

The model predicts the effect to be only dominant if the nanostructures are at least below 10 nm in dimensions. There is an asymmetric peak broadening which is followed by a downshift (peak shift towards low wavenumber) of the 1st order c-Si Raman peak as shown in Figure 3.16. This effect is due to phonons confined into low dimensions as compared to bulk silicon [3.8 – 3.10].

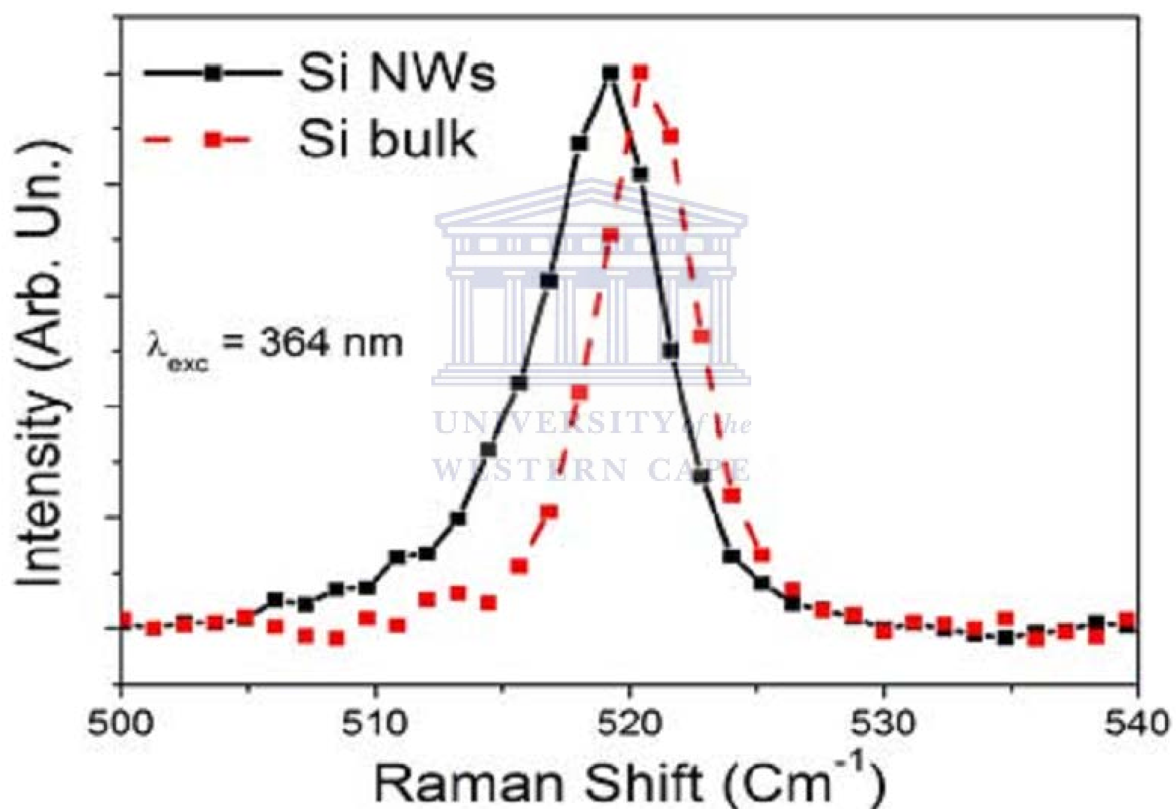

UNIVERSITY of the
WESTERN CAPE

Figure 3.16: First order Raman peak of SiNWs showing a downshift and asymmetric broadening as compared to the bulk Si [3.10].

Figure 3.15 shows two more peaks at 300 and around 900 cm^{-1} related to second order overtones of transverse acoustic vibrations at critical point X, 2TA (X) and second order transverse optical phonon vibrations, 2TO. In second order Raman scattering all the phonon in the BZ contribute to the vibrations and that is different from first order Raman scattering

[3.9]. This discussion shows SiNWs characterisation with Raman spectroscopy can provide valuable information about structural behaviour of silicon nanostructures (SiNWs).

3.5.4 Experimental Set-up and Data Acquisition

A typical set-up for Raman spectroscopy is shown in Figure 3.17 where a monochromatic beam laser is generator from an excitation source. The laser is passed through a pinhole, measured by a spectrometer and then collected as an expanded parallel beam. The radiation is then deflected by mirrors towards the notch filter and beam splitter, which reflects the light into the microscope. After interaction of the light with the sample the scattered radiation is collected from the microscope back through the same optics. The scattered radiation then passes through the notch filter at an angle that allows transmission of the scattered radiation. This radiation is then passed through a grating and onto the charge coupled device (CCD) detector, as shown in Figure 3.17.

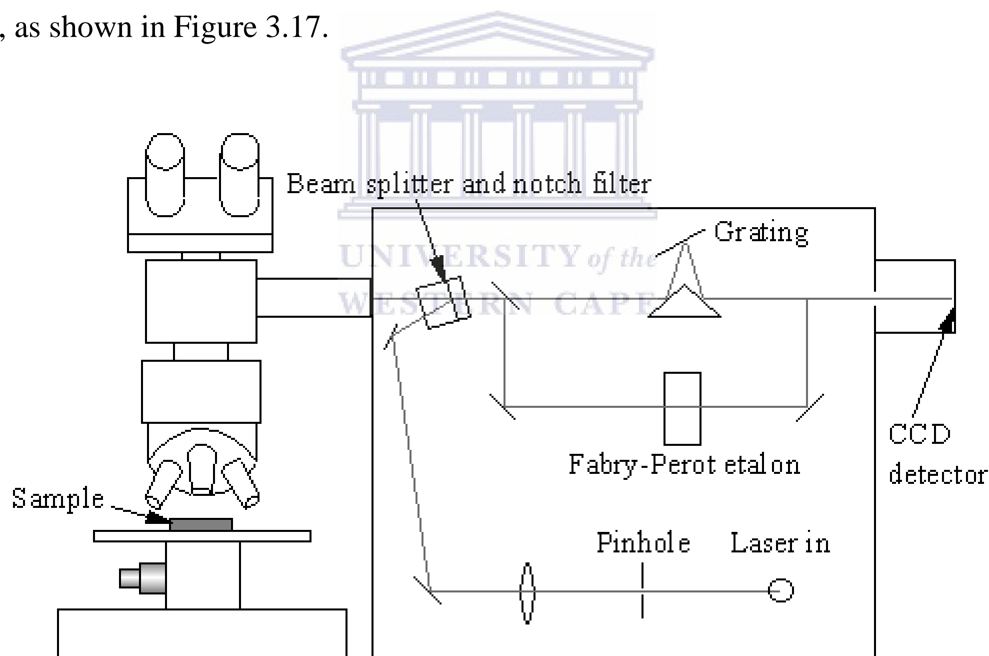

UNIVERSITY of the WESTERN CAPE

Figure 3.17: Schematic illustration of Raman spectrometer [3.6].

Raman measurements for SiNWs and bulk Si samples of size 1 x 1 cm^2 were obtained using a Jobin Yvon LabRAM HR 800 ultraviolet-visible-near-infrared Raman Spectrometer, equipped with an Olympus microscope at the CSIR, South Africa. The spectral resolution of the Raman scattering used was 0.463 cm^{-1} and the measurements were taken over the range

of 100 – 4000 cm^{-1} with excitation laser of 514 nm operating with a laser power of 1.21 mW to avoid local heating of samples.

3.6 Fourier Transform Infrared Spectroscopy

3.6.1 Introduction

Fourier transform infrared (FTIR) spectroscopy is one of the techniques suitable for the non-destructive study of nanomaterial and can provide qualitative and quantitative information about the atomic bonding. During FTIR spectroscopy, infrared radiation is used to generate a signal from the material which is converted into a spectrum that can be analysed using the mathematical method of Fourier transform. Infrared radiation is electromagnetic radiation with wavelength between 2.5 and 25 µm (1 µm = 10^{-4} cm) or wavelength reciprocal ranging between 400 and 4000 cm^{-1}. FTIR depends on the vibrational modes of atoms and thus is used to study atomic bonding in molecules during the irradiation of the samples with the infrared radiation. The transmitted or absorbed infrared gives information about the vibrational states of the molecules in the material [3.11].

UNIVERSITY of the
WESTERN CAPE

3.6.2 Theory of FTIR

Similar to Raman spectroscopy, infrared spectroscopy studies molecular vibration where the absorbed or transmitted incident infrared will leave signatures of the vibration in the form of a spectrum. The absorption of infrared radiation by a material will induce transitions between different vibrational energy levels, which require a change in dipole moment of the molecule. The absorbed radiation will have a frequency associated with energy of the transition states related by Plank's law:

$$E = hf = \frac{hc}{\lambda} \tag{3.15}$$

E is the energy and h is Plank's constant given by 6.63×10^{-34}J.s. The absorption will happen if equation (3.15) is satisfied, that means if there is a transition related to the frequency of the incident radiation by Plank's constant. The incident infrared will be

transmitted if Plank's law is not satisfied. As the vibrations are based on frequencies related to a wavelength or wavenumber (wavelength reciprocal) by equation (3.15), the intensity of the FTIR spectrum is governed by Beer-Lambert law:

$$I = I_0 e^{-\varepsilon c d} \tag{3.16}$$

where I and I_0 denote the intensities of the incident and transmitted beams, respectively, ε is the molecular absorption coefficient, c and d are the concentration and light path length of the absorbing material, respectively. If the measurements from the FTIR spectrometer are obtained in transmission mode they can easily be converted to absorption move via this relation:

$$A = \log\left(\frac{1}{T}\right) \tag{3.17}$$

derived from equation (3.16) and is used for quantitative analysis [3.11, 3.12]. Direction of the vibrational motion in FTIR gives information about the changes in bond length, known as the stretching vibration or change in bond angle known as deformation vibration. Deformation vibration is subdivided into wagging, bending, rocking and twisting modes and the stretching vibration subdivided to symmetric and asymmetric stretching.

UNIVERSITY of the
WESTERN CAPE

3.6.3 Experimental Set-up and Data Acquisition

The FTIR spectrometer employs the Michelson interferometer which consists of the beam splitter coming from the source of infrared and two flat controlling mirrors, one fixed and one movable as shown in Figure 3.18. The beam is controlled by collimators and directed towards the mirrors where the beam split into two equal intense parts by the beam splitter. The movable mirror controls the beam to interfere either constructively or destructively. From the interferometer the beam passes the sample and then directed to the detector for measurements. The beam leaves the interferometer as an interferogram, also known as time domain (intensity vs. time) and then converted into an infrared spectrum (intensity vs. frequency or frequency domain) via Fourier transformation by employing a computer. This happens when the signal leaves the detector, as shown in Figure 3.18 [3.11, 3.12].

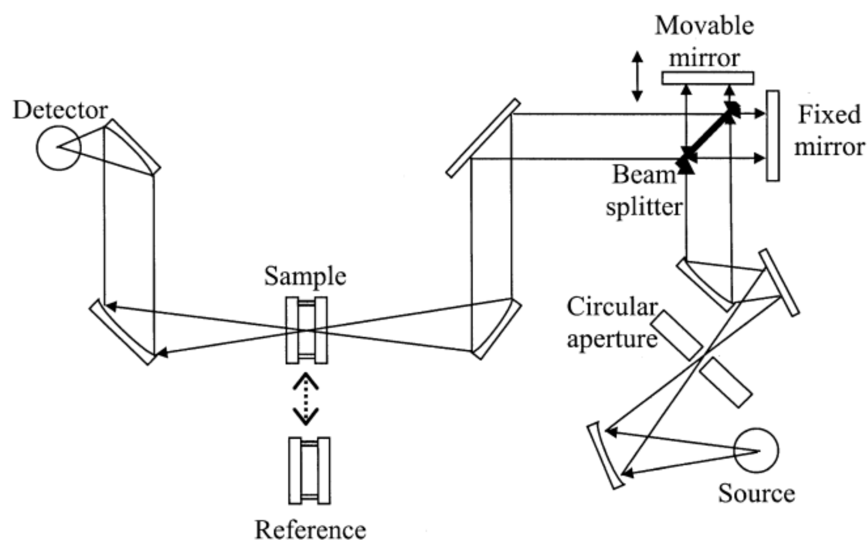

Figure 3.18: Schematic of FTIR spectrometer with Michelson interferometer [3.12].

FTIR measurements were taken using a Perkin Elmer Spectrum 100 FTIR spectrometer for SiNWs and bulk Si samples. Measurements were taken from 400 to 4000 cm^{-1} range and a resolution limit of 4 cm^{-1} for 20 scans was used at room temperature. The results were obtained at transmission mode and converted to absorption mode via equation (3.17) in which plotting and analysis was done using the Origin Pro 8 software.

UNIVERSITY of the
WESTERN CAPE

3.7 Ultraviolet-Visible Spectroscopy

3.7.1 Introduction

Ultraviolet-visible (UV-Vis) spectral range extends from 150 – 800 nm in the electromagnetic spectrum. Ultraviolet contribution to the range is between 150 and 400 nm and visible range is between 400 and 800 nm and the visible range is what human eyes detect as light. Similar to the Raman and FTIR which induce vibrations on material molecules, UV-Vis radiation induces electronic transitions in an atom. Absorption of light causes a transition from a ground state to an excited state and the relaxation of such excited states may cause emission of light referred to as luminescence. Absorption and emission of light depends on the energy of the incident light [3.12]. The UV-Vis spectral range is known to be of great importance for photovoltaic functioning in which radiation is required to be absorbed than

emitted. Materials used for solar cell manufacturing are not perfect absorbers of light as there are losses during light transmission and reflection in which reflection mostly comes as a great loss of light. Intense research has been dedicated into reducing the reflection of light on silicon based solar cells and thus characterisation of these materials requires measurements of reflection and or absorption through UV-Vis spectroscopy.

3.7.2 Theory of UV-Vis Spectroscopy

Ultraviolet and visible light propagate through space as electromagnetic radiation or as photons having frequency, f that is related to the wavelength, λ by this relation:

$$f = \frac{c}{\lambda} \tag{3.18}$$

where c is the speed of light in vacuum given by $3 \times 10^8\ m/s$ having energy E as was shown in equation (3.15). The propagation of light as electromagnetic waves is described via the equation:

$$A(\varphi) = A_0(\varphi)e^{i(\omega t-\delta)} \tag{3.19}$$

where A is the amplitude, ω is the circular frequency, δ the phase angle, and φ is the polarization angle [3.12]. The circular frequency ω is related to wavelength λ and refractive index n for non-absorbing medium by:

$$\omega = \frac{c}{\lambda n} \tag{3.20}$$

For an absorbing medium refractive index n is replaced by its complex form $n^* = n + i\kappa$ where n and κ are always positive [3.12].

When light is incident into a solid material it will be transmitted, absorbed or reflected. The transmitted light through a solid material of thickness d and concentration c is described by the ratio of the transmitted light intensity I_t to that of the incident light I_0 i.e. $T = I_t/I_0$ as shown in Figure 3.19. The relation between light intensities, the sample thickness and the concentration were shown in equation (3.16) and is known as the Beer-Lambert Law. Also

equation (3.17) showed how light transmission is related to light absorption but that does not mean measured transmission can directly be converted to absorption as there may be some reflections and scatterings.

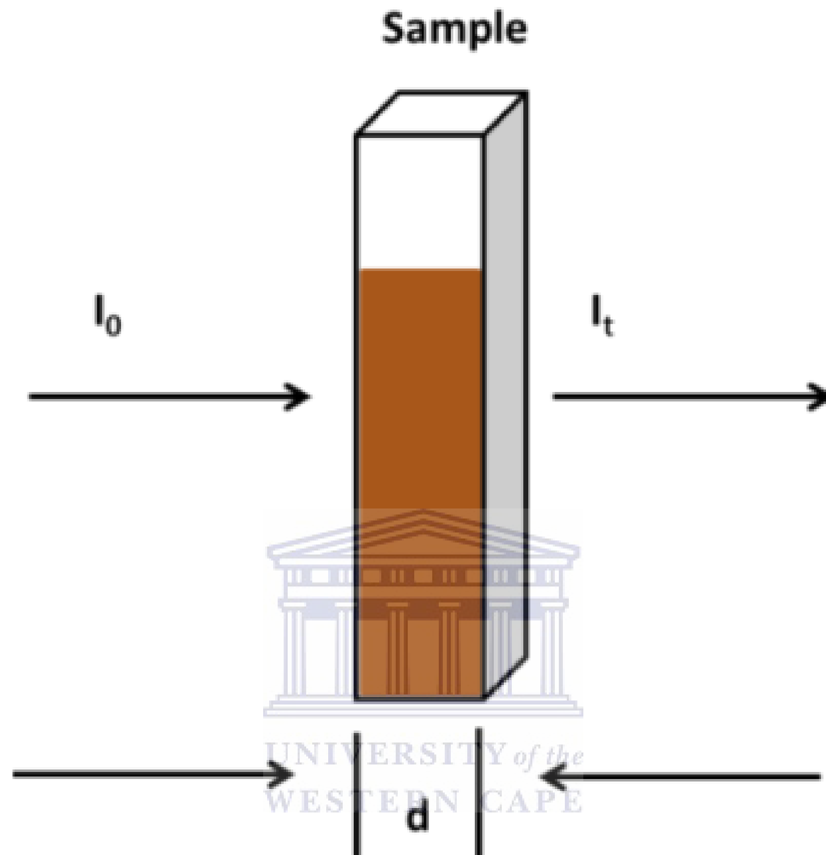

Figure 3.19: Schematic illustration of transmitted light through a sample [3.12].

3.7.3 Reflectance

Light reflection is one of the events takes place during incident interaction of light with the sample or material. Reflectance comes as a major problem when looking at the functioning principles of solar cells where maximum absorption of light is required. The reflection of light can be specular for smooth surfaces like mirrors or polished silicon substrates or diffuse in rough surfaces. Specular and diffuse reflections are illustrated in Figure 3.20. Incident and reflected light rays are always parallel to each other in specular reflection and that is completely different in diffuse reflection where rays are reflected at random directions [3.12, 3.13].

Smooth surfaces like polished c-Si substrates have texture with small particles less than the visible light wavelength and thus the surface appears continuous visible light resulting into specular reflection. If the roughness of the surface have dimensions that are larger than the wavelength of visible light (1000 nm), then light will be reflected in many directions resulting into diffuse reflection.

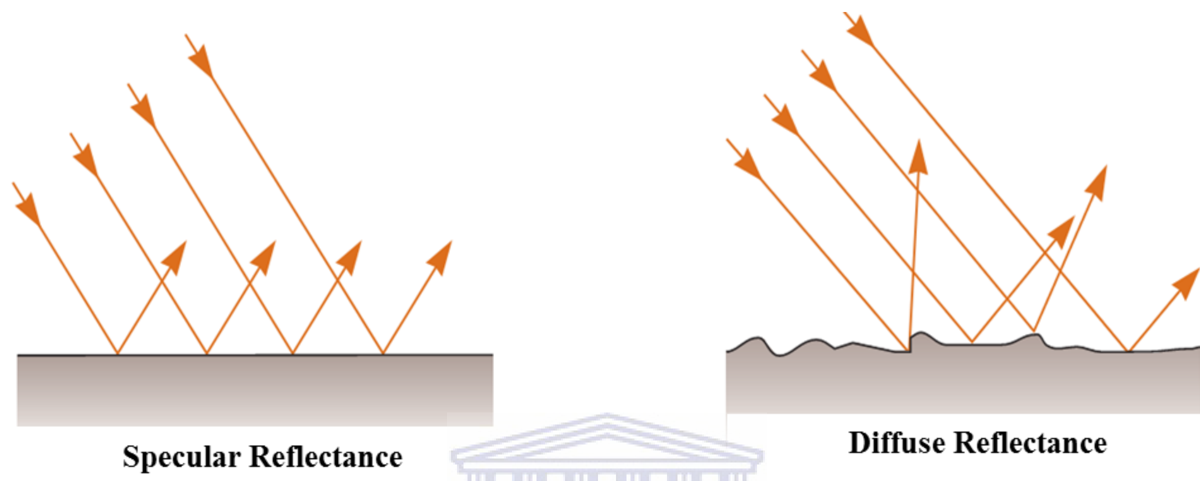

Figure 3.20: Schematic representation of specular and diffuse reflections [3.13].

UNIVERSITY of the

Another important factor to consider for the interaction of light through air and into the material of different mediums is that of refractive index "*n*". Refractive index is the ratio of the speed of light in vacuum "*c*" to the speed of light within a transparent medium "*v*" as shown below [3.13].

$$n = \frac{c}{v} \tag{3.21}$$

The refractive index describes the refraction or bending of light within a transmitting medium developed by Willebord Snell and known as Snell's law given in below [3.13]:

$$n_1 \sin\theta_1 = n_2 \sin\theta_2 \tag{3.22}$$

The refraction of light between two mediums is explained in Figure 3.21, where n_1, θ_1 and n_2, θ_2 in equation (3.22) corresponds to air (medium 1) and glass (medium 2), respectively, in the figure. Equation (3.22) and Figure 3.21 shows that light will bend towards the normal when

travel from medium of low refractive index (air) to a medium of higher refractive index (glass) with different refraction angles. This effect also happens in silicon substrate with a layer of silicon nanowires which they have different refractive index and that effect has been associated to the reduced reflection observed in samples of SiNWs as compared to bulk Si [3.14].

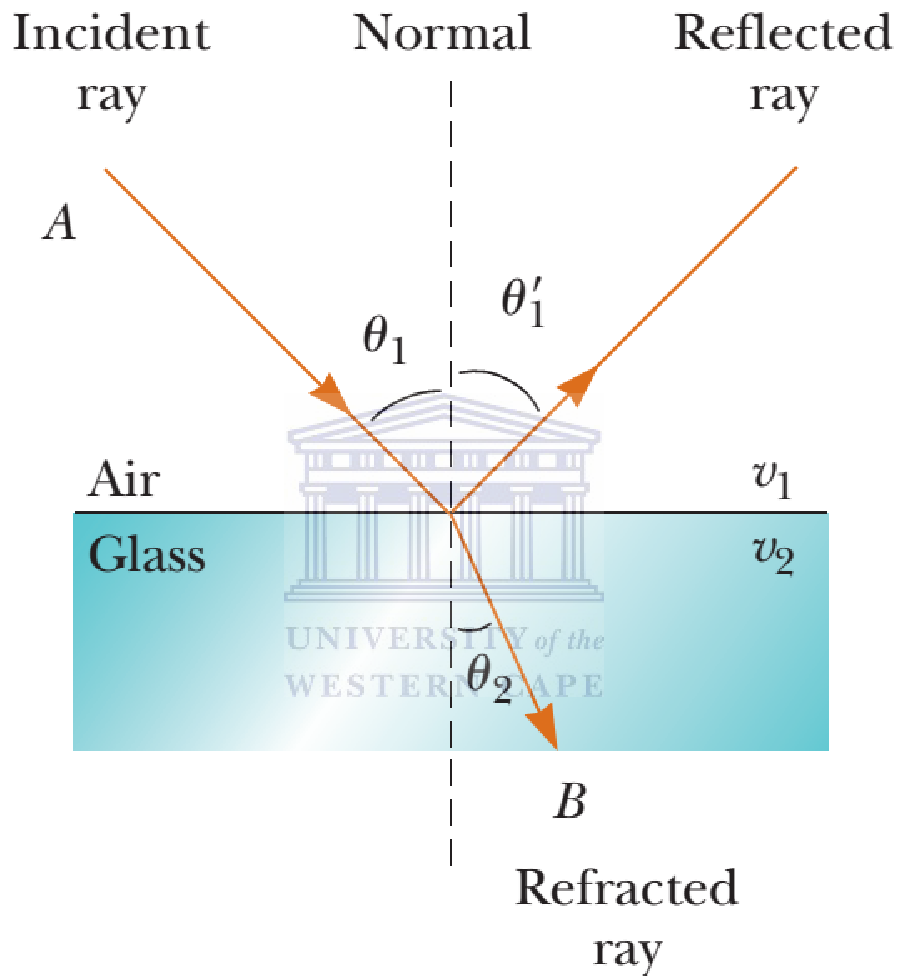

Figure 3.21: Light refraction between two mediums of different refractive indices [3.13].

3.7.4 Experimental Set-up and Data Acquisition

UV-Vis spectrometers are based on two radiation sources for the emission of ultraviolet light and visible light for the measurements of UV-Vis spectrum. Xenon or deuterium lamps are used for the emission of ultraviolet and usually tungsten and halogen lamps are used for visible radiation. These different sources are used to supply light of different wavelengths

ranges in which shorter wavelength is obtained from ultraviolet sources and longer wavelength from that of visible sources.

A conventional spectrometer contains a light source, monochromator, sample stand, detectors as shown in Figure 3.22 and finally a computer to record the data. Monochromator is used to filter the wavelength into one single wavelength before the light reaches the sample then a detector. Detectors are there to convert the electromagnetic radiation into a signal or spectrum that can be generated by a computer [3.12].

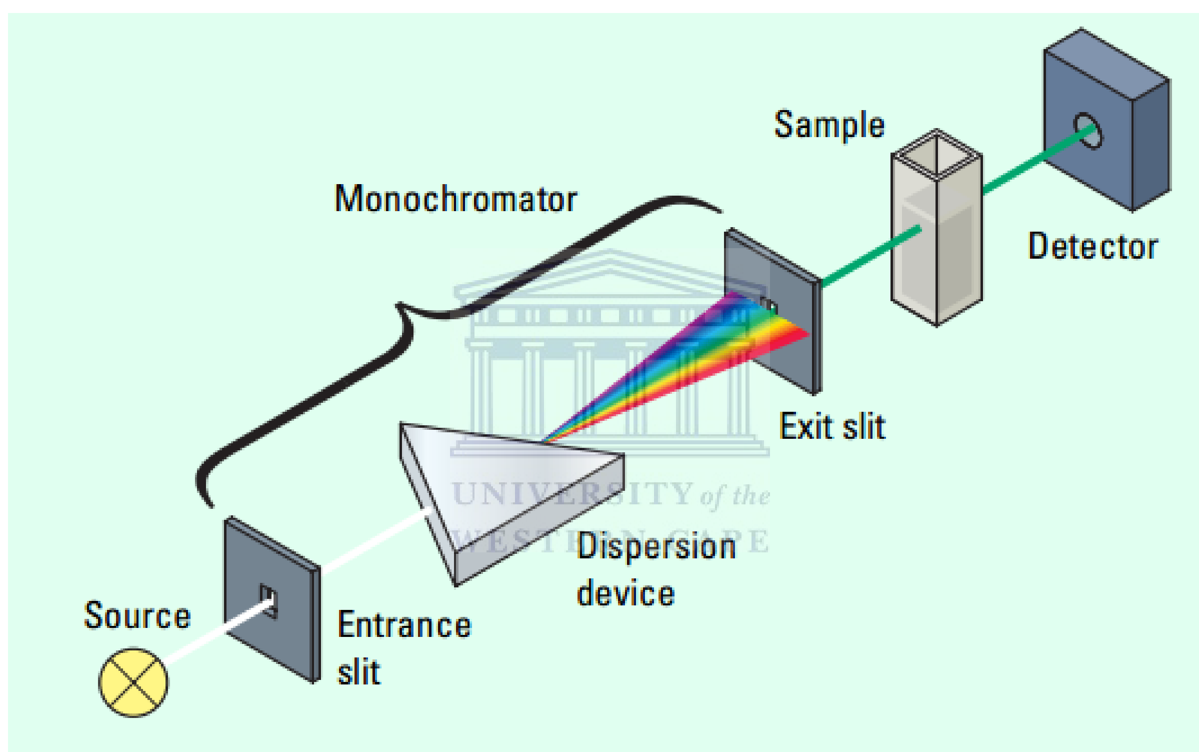

Figure 3.22: Schematic illustration of a UV-Vis spectrometer [3.12].

The reflectance measurements for specular and diffuse were taken with two different spectrometers and different procedures were followed. Specular reflectance was acquired at the range of 200 – 1000 nm with spectral resolution of 1 nm using a Semiconsoft Inc, Mbrobe Thin-film measurement system. Diffuse reflectance was taken from 200 – 900 nm with similar resolution as specular using a Cary 1 E system; both measurements were done in the physics department, UWC.

References

[3.1] P. Goodhew, J. Humphreys and R. Beanland, "*Electron Microscopy and Analysis*", 3rd Edition, Taylor & Francis, London (2001).

[3.2] I. Watt, "*The principles and Practice of Electron Microscopy"*, 2nd Edition, Cambridge University Press, Great Britain (1997).

[3.3] J. Goldstein, D. Newbury, P. Echlin, D. Joy, C, Fiori and E. Lifshin, "*Scanning Electron Microscopy and X-ray Microanalysis"*, Plenum Press, New York (1981).

[3.4] D. Williams and C. Carter, "*Transmission Electron Microscopy: A Textbook for Materials Science"*, 2nd Edition, Springer Science & Business Media, New York (2009).

[3.5] B. Cullity, "*Elements of X-ray diffraction"*, Addison-Wesley Publishing Company, Reading, Massachusetts (1978).

[3.6] E. Smith and G. Dent, "*Modern Raman Spectroscopy: A practical approach"*, John Wiley and Sons Ltd., Great Britain (2005).

[3.7] D. Long, "*The Raman Effect: A Unified Treatment of the Theory of Raman Scattering by Molecules"*, John Wiley and Sons Ltd., Chichester, West Sussex, England (2002).

[3.8] S. Piscanec, M. Cantoro and J. Robertson, Physical Review B **68** (2003) 241312 – 241315.

[3.9] S. Khachadorian, "*Vibrational properties of silicon nanowires"*, PhD Thesis, Technical University of Berlin, Germany (2011).

[3.10] C. D'Andrea, M. Lo Faro, P. Musumeci, B. Fazio, F. Iacona, G. Franzò, P. Gucciardi, F. Priolo and A. Irrera, Physics Status Solidi C (2014) 1 – 4.

[3.11] W. Lau, "*Infrared Characterisation for Microelectronics"*, World Scientific Publishing Co. Pte Ltd. (1999).

[3.12] G. Gauglitz and T. Vo-Dinh, "*Handbook of Spectroscopy"*, Wiley-VCH, Verlag GmbH & Co. KGaA, Weinheim, Germany (2003).

[3.13] R. Knight, "*Physics for Scientists and Engineers: A Strategic Approach",* 2nd Edition, Pearson Addison-Wesley, California, USA (2008).

UNIVERSITY of the
WESTERN CAPE

[3.14] Z. Guo, J. Jung, K. Zhou, Y. Xiao, S. Jee, S. Moiz and J. Lee, Proceeding of SPIE **7772** (2010) 77721C – 77727C.

CHAPTER FOUR

Results and Discussions

4.1 Introduction

In Chapter 2 the mechanism of the MaCE technique to synthesise vertically aligned SiNWs was discussed. In this chapter the morphology of the synthesised SiNWs from pre-deposited silver nanoparticles (AgNPs) and their role during the formation of the resulting nanowires will be investigated by means of SEM and EDS, which were discussed in Chapter 3. The different morphologies of AgNPs, deposited using different silver salt concentrations and deposition times, will also be presented.

To investigate the formation of the SiNWs during the MaCE technique, a parametric study was completed during which the effect of etching time and hydrogen peroxide (H_2O_2) concentration, the two most important parameters to consider, was probed. TEM studies were used to further investigate the structure of individual SiNWs. It is important to understand the crystal structure of the material prior the application and thus high resolution TEM (HR-TEM), x-ray diffraction and Raman spectroscopy were used to investigate the crystal structure of individual SiNWs as well as the bulk arrays. A further parameter to consider for application of these nanostructures in PVs is the surface passivation of the Si surface atoms as this plays a crucial role in the long term stability of the material during operation of the solar cell. To investigate this phenomenon, FTIR spectroscopy was employed, whereas UV-Vis spectroscopy was used to probe the optical reflectivity of the SiNW array.

The chapter will be summarised and conclusions made based on the discussion of all the characterisation techniques. The experimental conditions of the AgNPs and SiNW synthesis, as well as the operational conditions of the characterisation techniques were discussed in Chapters 2 and 3, respectively, therefore will not be elaborated in details in this chapter.

UNIVERSITY of the
WESTERN CAPE

4.2 Deposition of Silver Nanoparticles and their Morphology

As discussed in Chapter 2, the formation of AgNPs on the surface of crystalline Si (100) follows a process of electroless metal deposition (EMD) on a galvanic AgNPs deposition solution. To recall, the particles form from the nucleation of small Ag ions, which then grow into bigger AgNPs. As mentioned in Chapter 2.8, the resulting AgNPs obtained from three different silver salt concentrations will be discussed using SEM images and EDS measurements.

Since the AgNPs continue to be deposited on the Si substrate as long as the samples are immersed in the electrolyte solution, it should be expected that different deposition times and silver salt concentrations should lead to different AgNPs morphologies. Shown in Figure 4.1 are the SEM micrographs of AgNPs deposited using a lower concentration of 5 mM $AgNO_3$ for immersion times of 15, 60, and 300 seconds. As shown in Figure 4.1 (a) and (b), at short dipping periods interconnected architectures form, with no clear particles observed. The formation of these structures is attributed to the fact that at short deposition times, fewer Ag ions from the $AgNO_3$ solution nucleate, which then coalesce to ultimately form the observed morphology. Similar structures were observed elsewhere [e.g. 4.1]. At a longer dipping time, as shown in Figure 4.1 (c), the nanoparticles appear less dense and become isolated, diverging from the "brain-like" structures of Figure 4.1 (a) and (b), to form semi-spherical shapes.

Overall, as can be observed from the micrographs in Figure 4.1 that the particle density decreases for increasing immersion times and is accompanied by an increase in diameter of individual particles. At closer inspection it was found that the average diameters were about 75 ± 1 nm, 109 ± 3 nm, and 102 ± 2 nm for the structures of Figure 4.1 (a), (b), and (c), respectively. The increase in nanoparticle diameter with increasing immersion time in Figure 4.1 is ascribed to the transformation of nanoparticle shapes from the dense "brain-like" structures to more isolated particles. This change in shape may also have contributed to the increase in the standard deviation of the diameter distribution measurements of the AgNPs.

Another set of investigations on changes in AgNPs morphology for different deposition times but with a higher $AgNO_3$ concentration of 20 mM, was conducted. Figure 4.2 shows these

changes in morphology of AgNPs as the deposition time was increased from 15 seconds to 300 seconds. The nanoparticles obtained after 15 seconds averaged at about 99.4 ± 0.7 nm in diameter, which is about the same diameter as the nanoparticles obtained from longer deposition time, at lower silver salt concentration, shown in Figure 4.1 (b) and (c). AgNPs deposited for 60 seconds in 20 mM concentration shows even bigger diameters of about 154 ± 4 nm, as shown in Figure 4.2 (b), with more spaces between the nanoparticles. The AgNPs in Figure 4.2 (b) shows a wide range of diameters, unlike the ones of shorter deposition time (Figure 4.2 (a)), where the bigger nanoparticles appearing on top of the smaller ones. This trend makes sense because the nucleation starts at the substrate-solution interface and proceeds outwards on top of the previously formed nanoparticles.

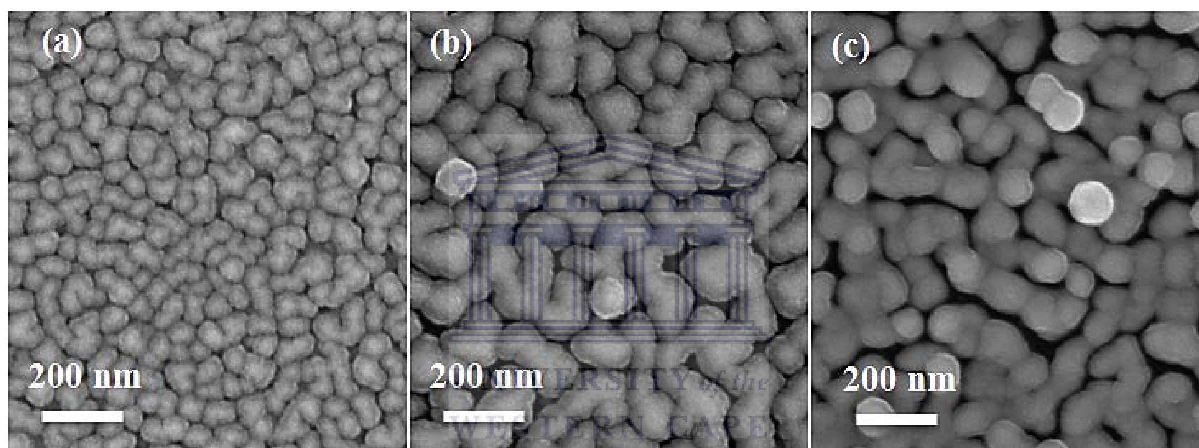

Figure 4.1: Silver nanoparticles deposited at different times using low $AgNO_3$ concentration (5mM). (a) for 15 seconds, (b) for 60 seconds, and (c) for 300 seconds.

So with more Ag ions present in the solution and longer immersion time for the growth means particles grow larger and with faster rate. This fast growth is also shown in Figure 4.2 (c) and (d) where different structure or morphologies of AgNPs were observed at longer deposition time of 300 seconds. On average the nanoparticles on this sample were found to be less than that for 60 seconds of immersion and had average diameter of 141 ± 4 nm. Shown in Figure 4.2 (d) is the lower magnification of the micrograph in (c) where particles formed tree-like structures, better known as dendrite structures [4.2, 4.3]. The formation of these dendrite structures might give evidence of the bigger and shapeless nanoparticles in Figure 4.2 (b) where it shows the initialisation of such structures but lacking enough time for the

formation to be complete. It is again showed that by controlling the deposition time for a certain concentration of $AgNO_3$, nanoparticles of certain morphology could be achieved.

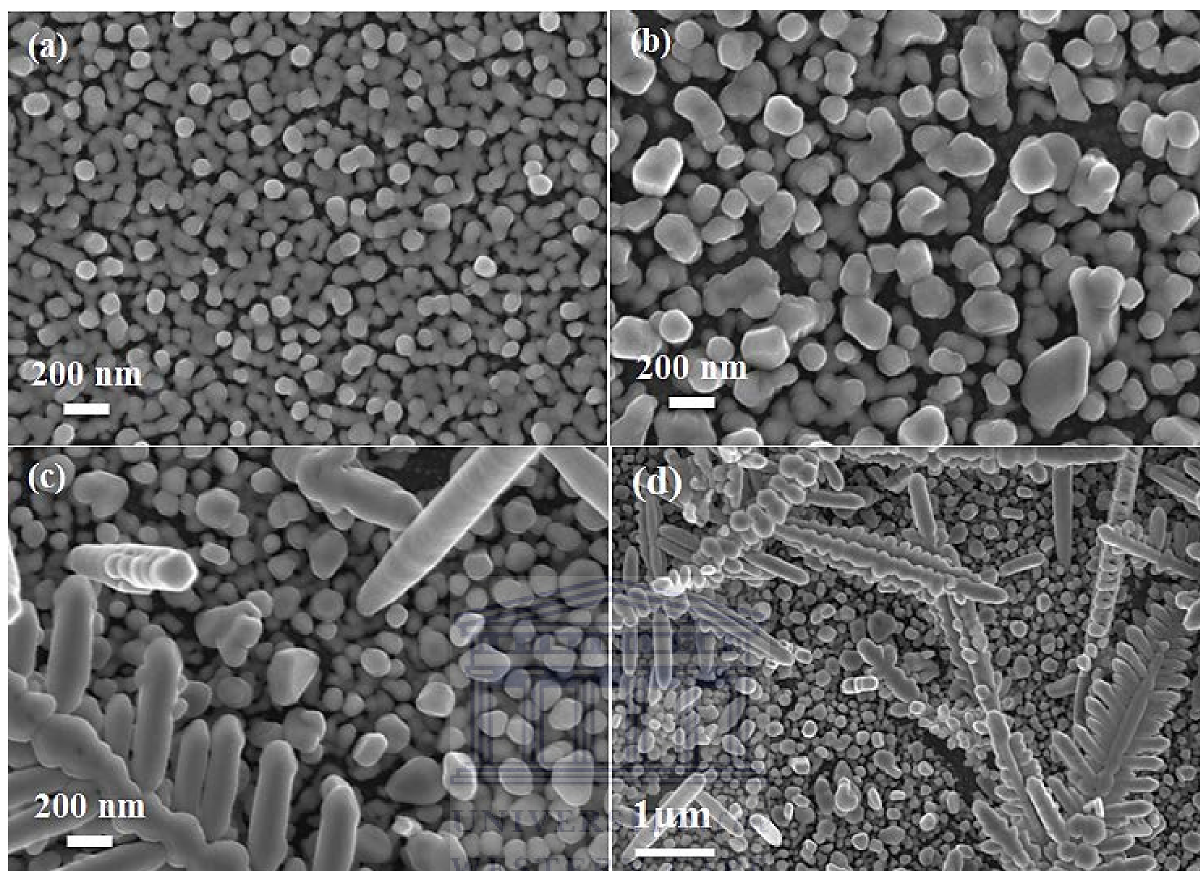

Figure 4.2: AgNPs obtained from the AgNO3 concentration of 20 mM, deposited from different immersion times. (a) deposited for 15 seconds, (b) 60 seconds, (c) for 300 seconds and (d) is the low magnification of the image in (c).

Further increasing the $AgNO_3$ concentration to 50 mM resulted in bigger nanoparticles with an average diameter of 170 ± 4 nm for the shortest deposition time of 15 seconds, as shown in Figure 4.3 (a), while an increase in the deposition time showed more dendrite structure formation for deposition times of 60 and 300 seconds, Figure 4.3 (b) and (c). The diameters of these particles did not deviate that much compared to the 15 seconds deposited sample. Low magnifications shown in Figure 4.3 (d) and (e) reveal different morphologies of these dendrite structures, where in (d) they are widely separated and in (e) are densely packed in a small area, which eventually grow into a big cluster. This can also be correlated in the mechanism formation of AgNPs where Ag ions get deposited onto previously formed small

nuclei and the particle grows larger in diameter. With high concentration and longer deposition time this leads into bigger nanoparticles and eventually dendrite structures.

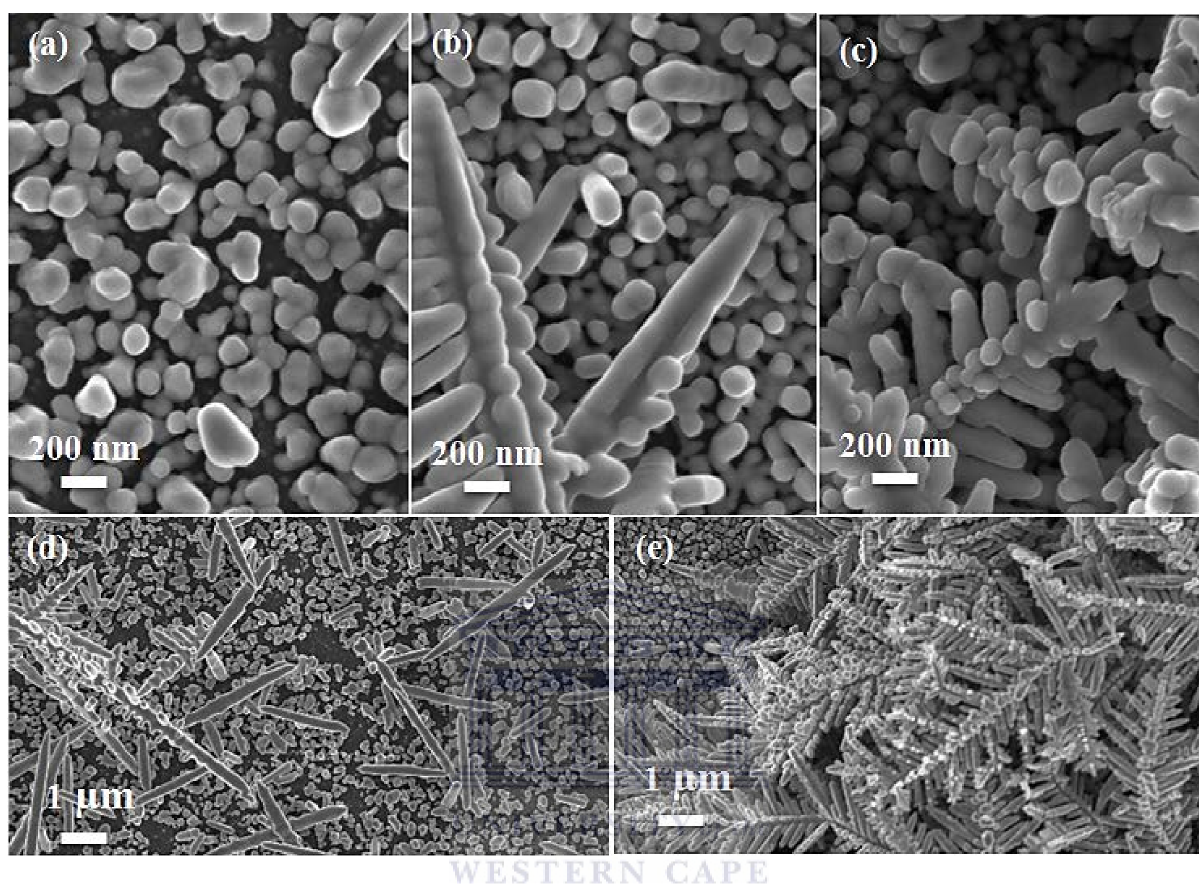

WESTERN CAPE

Figure 4.3: AgNPs obtained from the highest silver salt concentration of 50 mM. (a), (b), and (c) from deposition times of 15, 60, and 300 seconds, respectively, (d) and (e) are the lower magnification of dendrite structures.

Based on the findings of the above sets of experiments another experiment was designed for a deposition of 30 seconds using a 20 mM $AgNO_3$ concentration which gave more spherical and uniformly distributed AgNPs, as shown in Figure 4.4. The particles had diameters averaging 114 ± 2 nm, which are between the diameters mentioned for nanoparticles obtained from the same concentration at deposition times of 15 and 60 seconds. This condition of nanoparticle deposition was used almost throughout the study during the silicon nanowires synthesis based on their good distribution in terms of density and uniformity. Figure 4.4 (b) shows a larger scale of the distribution obtained using a lower magnification of the micrograph in Figure 4.4 (a).

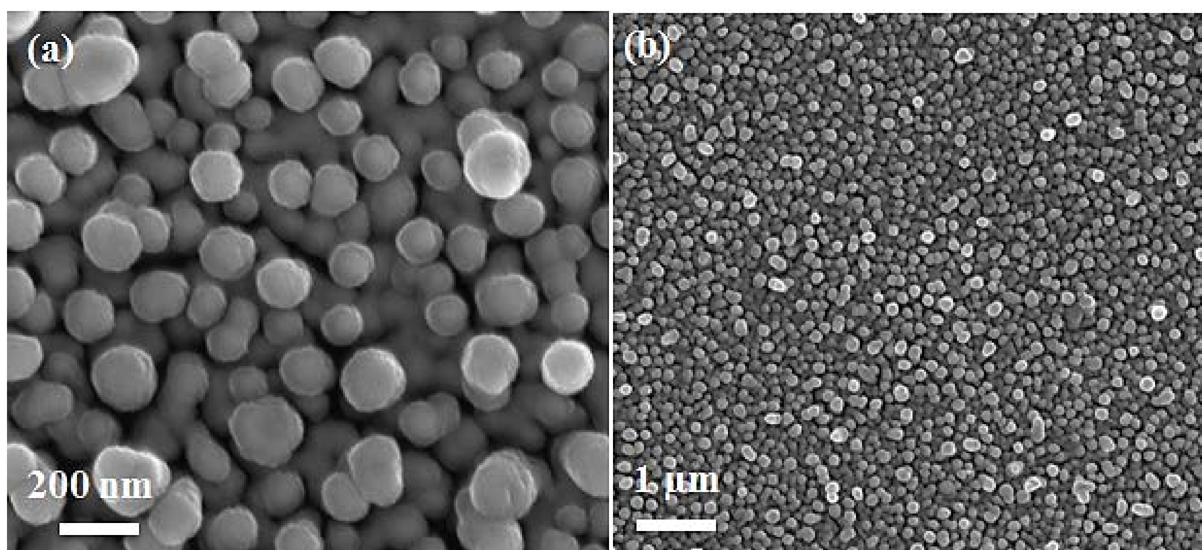

Figure 4.4: Nanoparticles obtained from 30 seconds deposition time from 20 mM $AgNO_3$ concentration (a), lower magnification in (b).

It was verified by EDS that the structures appearing are really made of silver. Those results are shown in Figure 4.5, where Figure 4.5 (a) shows the EDS spectrum and spot in which the EDS measurements were taken is shown in Figure 4.5 (b). These results reveal that indeed the nanoparticles were deposited on top of the Si substrate in which that is shown by peak intensities of Si and Ag at different energies.

UNIVERSITY of the
WESTERN CAPE

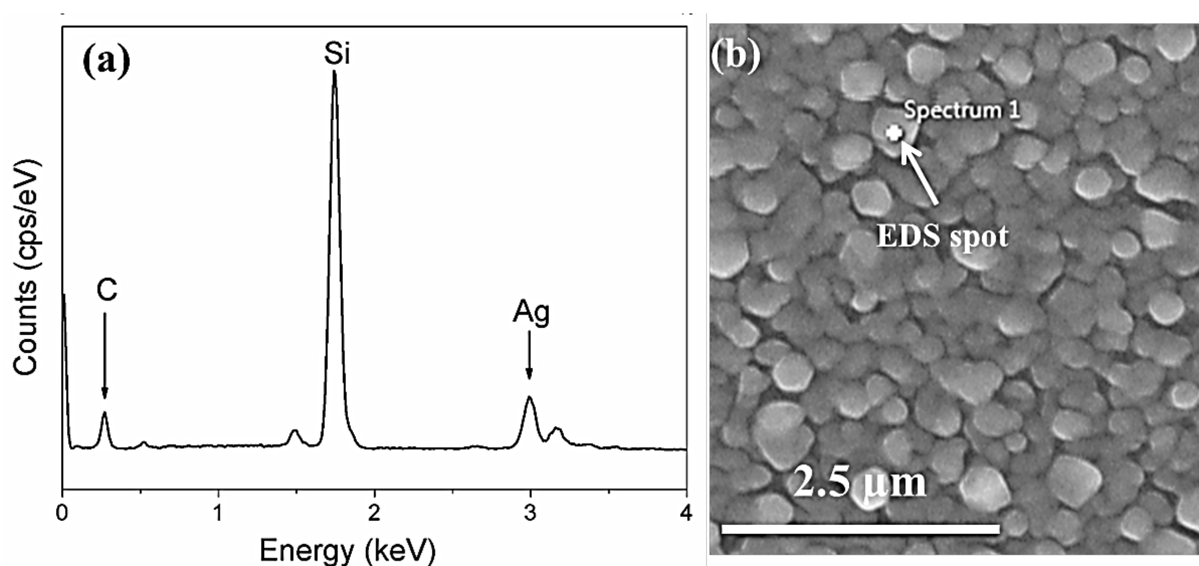

Figure 4.5: EDS measurements for AgNPs. EDS spectrum in (a) and (b) is the image showing the position in which the EDS measurements were taken.

4.3 Synthesis of Vertically Aligned Silicon Nanowires and their Properties

4.3.1 Investigation of the Morphology of SiNWs

4.3.1.1 Effect of Etching Time on SiNW Formation

As discussed in Chapter 2, pits form underneath the deposited AgNPs during the first few seconds of AgNPs formation due to oxidation-dissolution of silicon. These pits initialise the synthesis of silicon nanowires when the AgNPs coated samples are immersed in the etching solution. During the MaCE synthesis of SiNWs, the Si/AgNPs substrates turned rough black indicating the formation of the nanowires; these morphologies were further investigated with scanning electron microscopy.

Figure 4.6 (a) shows a cross-sectional SEM micrograph of a Si/AgNPs substrate etched for 30 seconds in a HF + H_2O_2 + H_2O (5 M HF and 0.5 M H_2O_2) where it can be observed that the Ag metal nanoparticles appear at the bottom of SiNWs (at Si/SiNWs interface). Evidence for that will be discussed below as the presence of Ag at the bottom of nanowires was confirmed with EDS measurements. The SiNWs shown in Figure 4.6 (a) had an average length of about 130 ± 5 nm. Figure 4.6 (b) shows the top view of the substrate etched at 30 seconds, where the Ag mesh was observed on the top surface as it sank into the substrate, leaving un-etched regions which form the resulting nanowires. The observed Ag mesh depicts that the synthesis was still in the initial stages, as it will also be shown later that Ag does not appear in the top view of longer nanowires.

UNIVERSITY of the
WESTERN CAPE

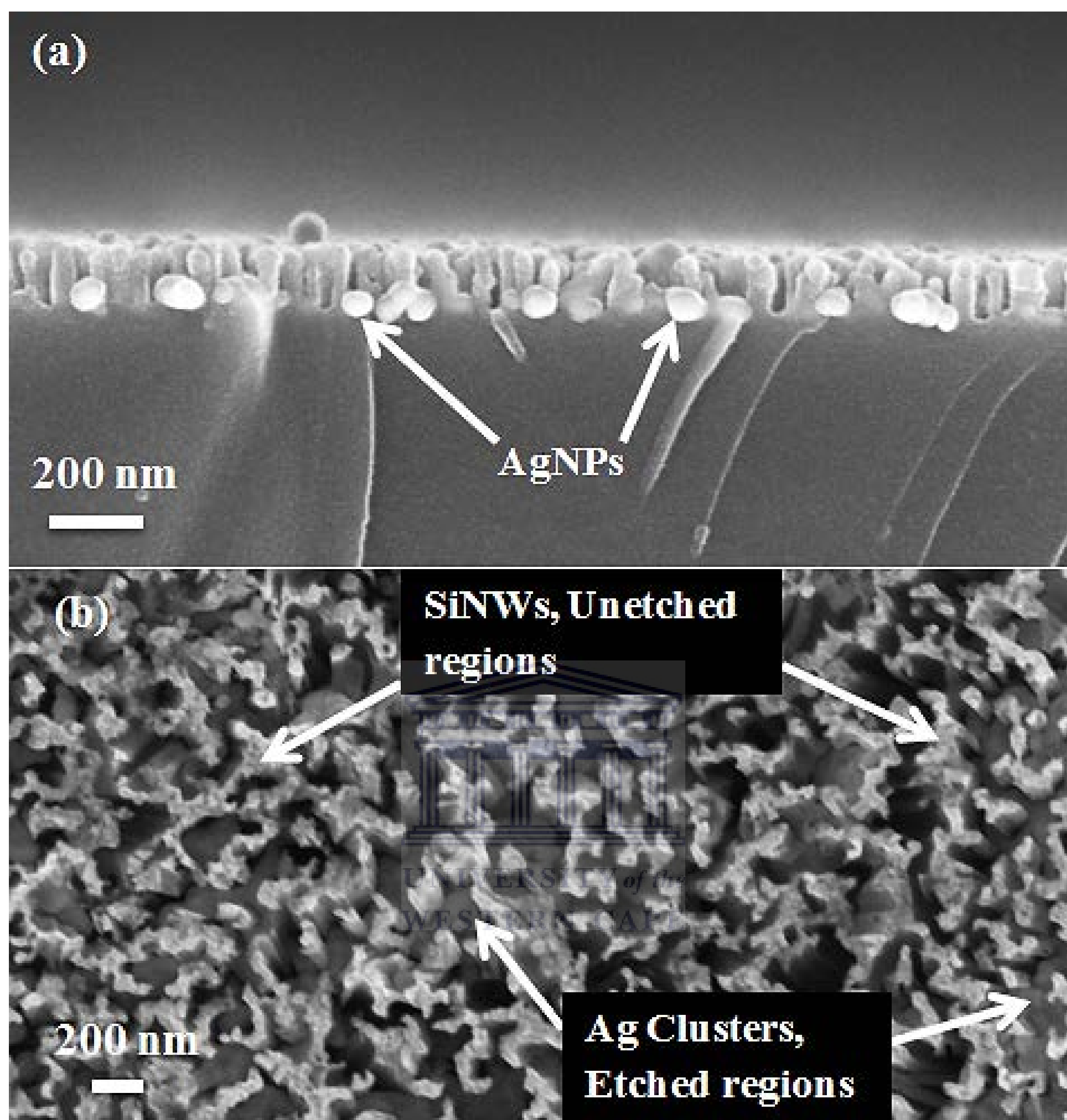

Figure 4.6: SEM cross section (a) and top view (b) of SiNWs after 30 seconds of etching showing the presence of Ag.

After few minutes of etching, remnants of silver nanoparticles were observed sitting at the SiNWs/Si interface. Figure 4.7 (a) and (b) shows SEM micrographs of SiNWs with and without AgNPs and the evidence for the presence and absence of these nanoparticles was confirmed with EDS measurements Figure 4.7 (e) and (f), respectively. AgNPs were dissolved into concentrated nitric acid (HNO_3) by dipping the samples for about 15 minutes, and no damages were observed from the nanowires after the nanoparticle dissolving step.

Those SEM micrographs shows longer nanowires than the ones in Figure 4.6 and that shows even for longer nanowires AgNPs remain at the bottom. This gives ideas about the growth mechanism where the motion of the particles or even the Ag mesh determines the resulting morphology of the nanowires.

The presence of AgNPs at the bottom of SiNWs shows that all the regions on the bare Si substrate covered with AgNPs during the nanoparticle deposition step will be etched. This is in accordance with literature which suggests that the etching is local at AgNPs/Si interface [4.4, 4.5]. The result of Figure 4.6 emphasises that only the regions of the substrate where there are AgNPs would be etched and that the regions where there are no nanoparticles would be left as SiNWs, which then again gives evidence that AgNPs determines the nanowire structure, in terms of diameter and density. Based on the measurements of the diameters of the Ag nanoparticles post SiNW synthesis, no reduction in the average particle diameter was observed. This implies that even though AgNPs assist during etching, their sizes do not change significantly during SiNW formation. It can then also be said that no significant changes were noticeable on the diameters of the nanowires, which were ranging between 50 and 200 nm as measured from different samples. Because of difficulties in measuring the diameters from the SEM micrographs no further discussion will be done on the nanowires diameters in this subsection.

UNIVERSITY of the
WESTERN CAPE

Figure 4.6 showed the initial stages of SiNW formation from metal nanoparticles, it is thus interesting to see what happens to these nanoparticles and the resulting nanowires as the etching given more time to proceed. Silicon nanowires synthesis mechanism explain that as long as there is still oxidant in the solution to reduce AgNPs forming more Ag^+ and injection of holes in the valence band of Si causing oxidation of silicon and there is enough HF in the solution to dissolve the formed SiO_2, then the SiNWs should continue to grow [4.4, 4.6]. SiNWs grew longer axially upon elongated etching time duration and there were no noticeable changes in diameter. It is believed that longer time offers the synthesis mechanism enough time to proceed as explained above, i.e. oxidation-dissolution process.

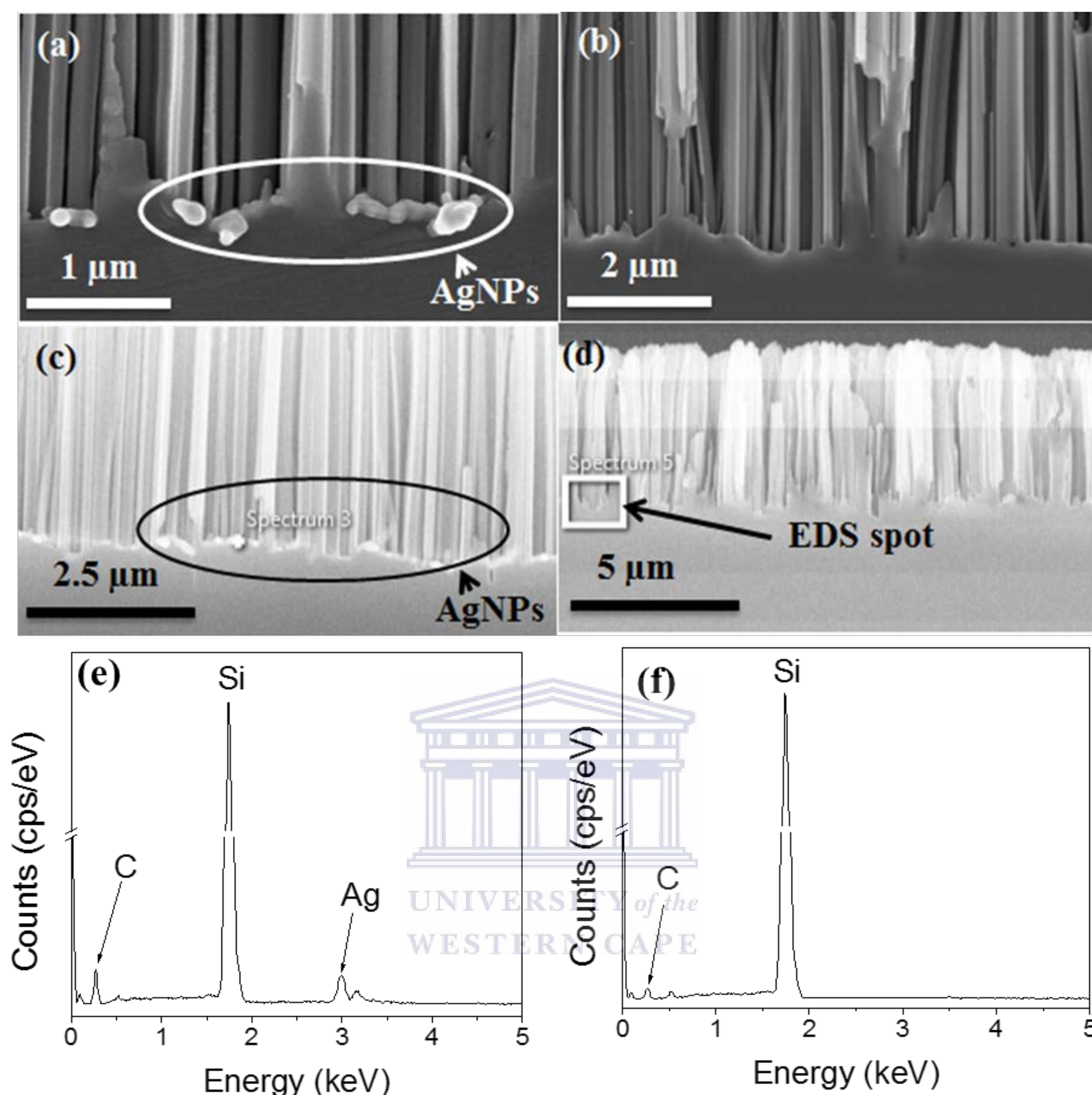

Figure 4.7: SiNWs with and without AgNPs in their bottoms, accompanied by EDS measurements. (a), (c) and (e) are the SEM micrograph, the EDS spot and the EDS pattern all depicting the presence of AgNPs, respectively. In (b), (d) and (f) are the results showing the absence of AgNPs.

Figure 4.8 illustrates the evolution of the nanowires after different etching times with cross section and top views of the morphology. Figure 4.8 (a) and (c) show nanowires with lengths of about 650 ± 7 nm obtained after 3 minutes of etching and in Figure 4.8 (b) and (d) SiNWs with lengths of about 920 ± 11 nm after etching time duration of 5 minutes. The presence of some AgNPs could still be observed at the bottom of nanowires in the cross sectional micrographs but nothing appeared in the top views, which is different from that observed for

shorter nanowires in Figure 4.6 where nanoparticles could clearly be observed in the top view image.

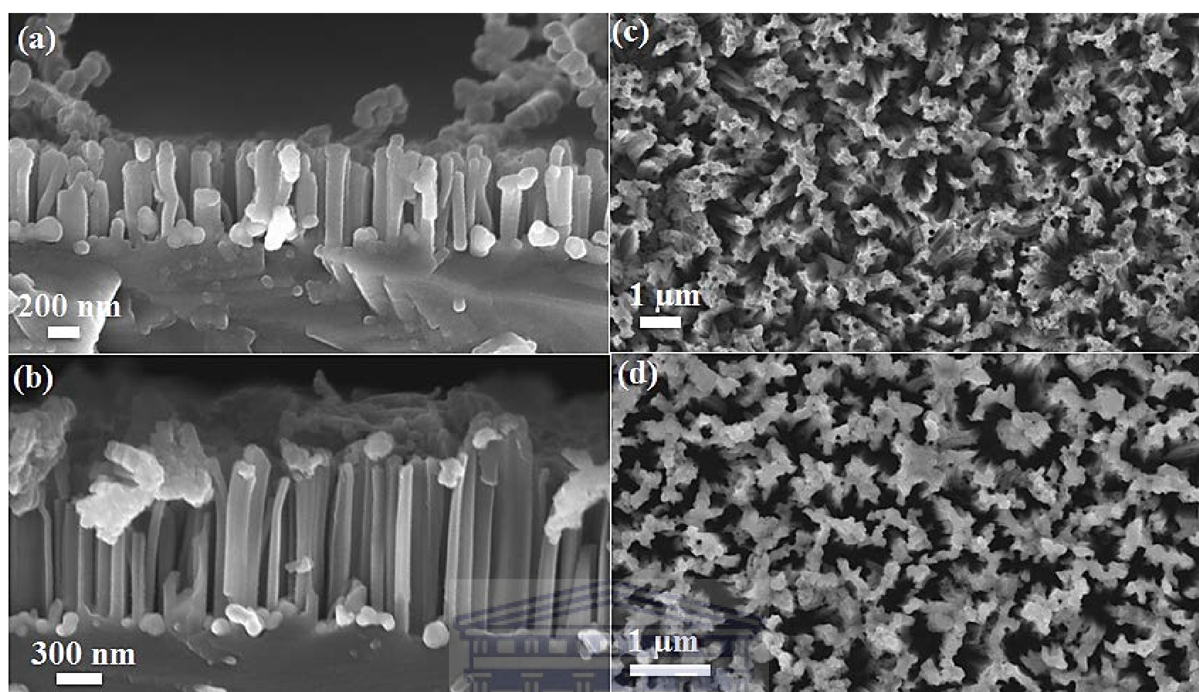

Figure 4.8: SEM micrographs of SiNWs synthesised for different times. (a) and (b) are the cross section views of the nanowires obtained after 3 and 5 minutes with their corresponding top view images (c) and (d), respectively.

UNIVERSITY of the
WESTERN CAPE

Further increase in etching time resulted into even longer SiNWs. As shown in Figure 4.9 (a) and (c), SiNWs with lengths of about 3.20 ± 0.05 µm are obtained after 15 minutes of etching, whereas 30 minutes yielded SiNWs with lengths of about 6.42 ± 0.07 µm, see Figure 4.9 (b) and (d). The SiNWs appear rougher in the top view micrographs demonstrating their longer lengths as compared to those in Figure 4.8. The top view also shows an interesting morphology, especially in Figure 4.9 (d) where the nanowires form bundles at their tips.

The possible reasons behind this conglomeration was discussed by Zhang *et al*. [4.7], where they ascribed the bundling to the fact that for longer nanowires strong forces, caused by dangling bonds and electrostatic charges, result into mutual attractions between the nanowires. Bai *et al.* [4.8] mentioned that the influence of Van de Waals forces may also play a role, causing the wires to congregate at their tops, forming bundles. The micrograph in Figure 4.9 (a) and its inset from a lower magnification shows a darker contrast of the image,

which is another sign of longer nanowires going deep into the substrate. A similar trend has been observed in nanowires synthesised via MaCE combined with lithography patterning, during which the nanowires did not bend as much but a weak conglomeration was observed [4.9, 4.10]. This was because in patterning the position of AgNPs is completely controlled together with their diameters and shapes so the resulting nanowires are vertically straight on the substrate with equal space between them, and thus the conglomeration can only be due to those inter-nanowire forces.

These bundled structures can also be as a result of the way AgNPs sink during etching as the observed conglomeration is more than what has been observed in lithography patterned nanowires. The spaces between the AgNPs leave vertical nanowires as un-etched regions as seen in the top view of Figure 4.6. These un-etched regions for longer SiNWs can appear as the bundled structures depicted in Figure 4.9 (c) and (d). Thus this fact combined with the inter-nanowire forces might be the reasons behind the conglomeration or the bundled nanowires.

UNIVERSITY of the WESTERN CAPE

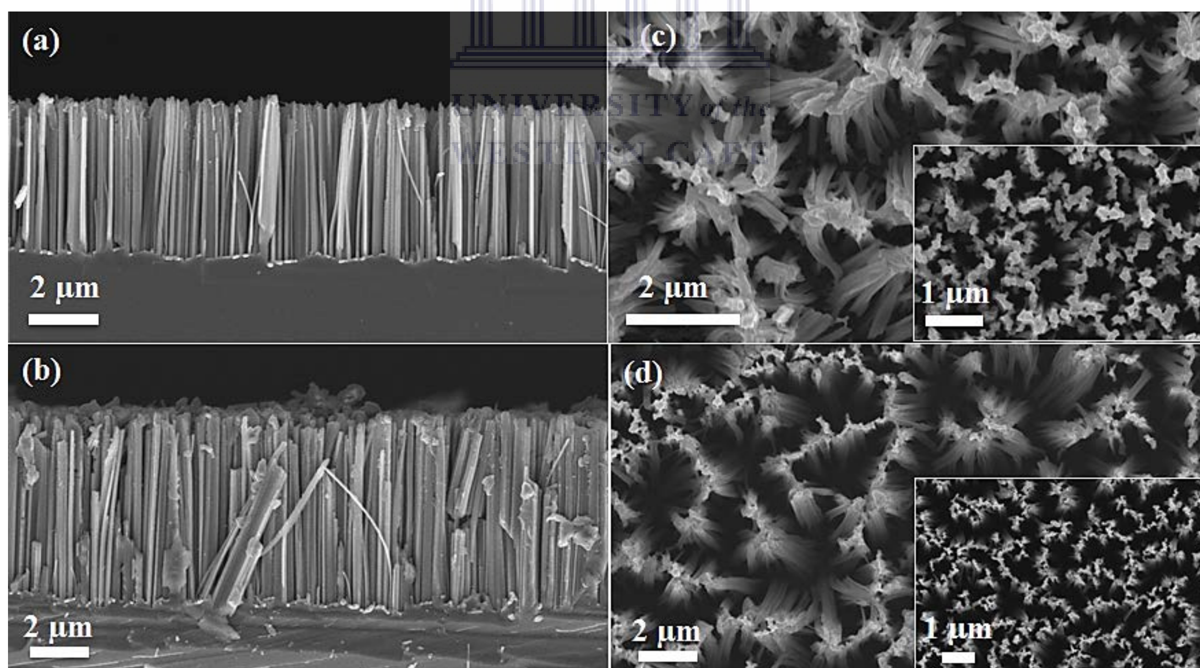

Figure 4.9: SEM micrographs of longer SiNWs after longer etching time durations. (a) after 15 minutes etching time, and (b) after 30 minutes cross sectional views, with (c) and (d) the corresponding top view images, respectively, with their low magnification as insets.

Figure 4.10 (a) and (b) show nanowires with lengths of about 11.2 ± 0.15 and 15.8 ± 0.20 μm synthesised after 50 and 80 minutes etching, respectively. These cross sectional images once more show (as observed in Figure 4.9 (b)) that the longer nanowires are not well separated at their bottoms as they cluster together, unlike the shorter nanowires, which were well separated from top to bottom. This might be due to the weakening of the H_2O_2 (oxidant) concentration in the solution during etching, resulting into some parts of the sample oxidising and some parts not. Another reason would be that during longer etching times, dense AgNPs formed small and well separated nanoparticles which left bigger spaces in-between them resulting into nanowires not well separated in their bottoms.

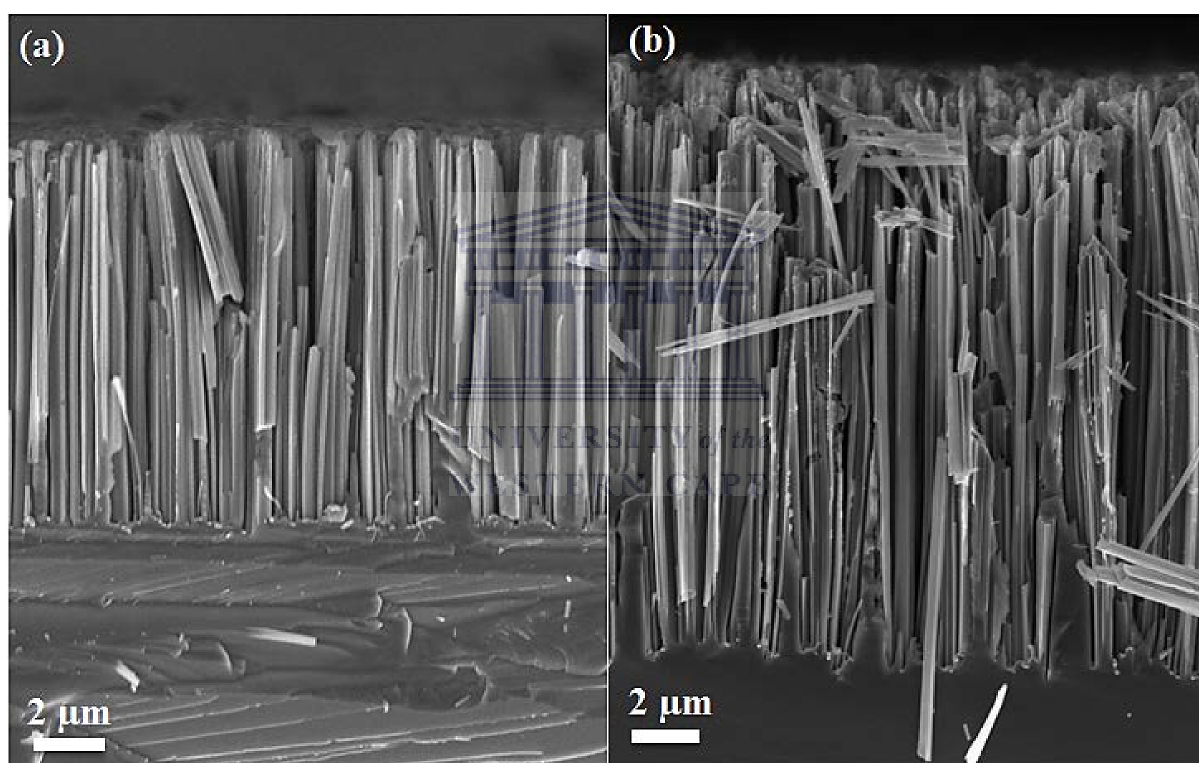

Figure 4.10: SEM cross section micrographs for longer SiNWs obtained after (a) 50 minutes and (b) 80 minutes etching time durations.

It was observed from these SEM micrographs that the lengths of SiNWs synthesised by metal assisted chemical etching increased from about 120 nm after 30 seconds to over 15 μm after 80 minutes of etching. The nanowires were observed to be linearly increasing with etching time as shown in Figure 4.11, with an etching rate of about 206 nm/min. This linear relation has been also observed in literature but with different etching rates [4.11, 4.12]. SiNWs grew longer with an increase in etching time because the etching was given enough time to proceed

and the solution had enough oxidising species to oxidise and dissolve the formed SiO_2. However, this concentration does not remain the constant in the solution and thus doubling the time would not necessary double the length. So considering the chosen time range, the relation looks linear but if the time could be increased to more than 80 minutes the curve would look rather exponential with high etching rate at the beginning and slows down after longer etching times. The etching time scale was not kept constant as to intentionally not double the times from one point to another as can also be seen from the graph points in Figure 4.11.

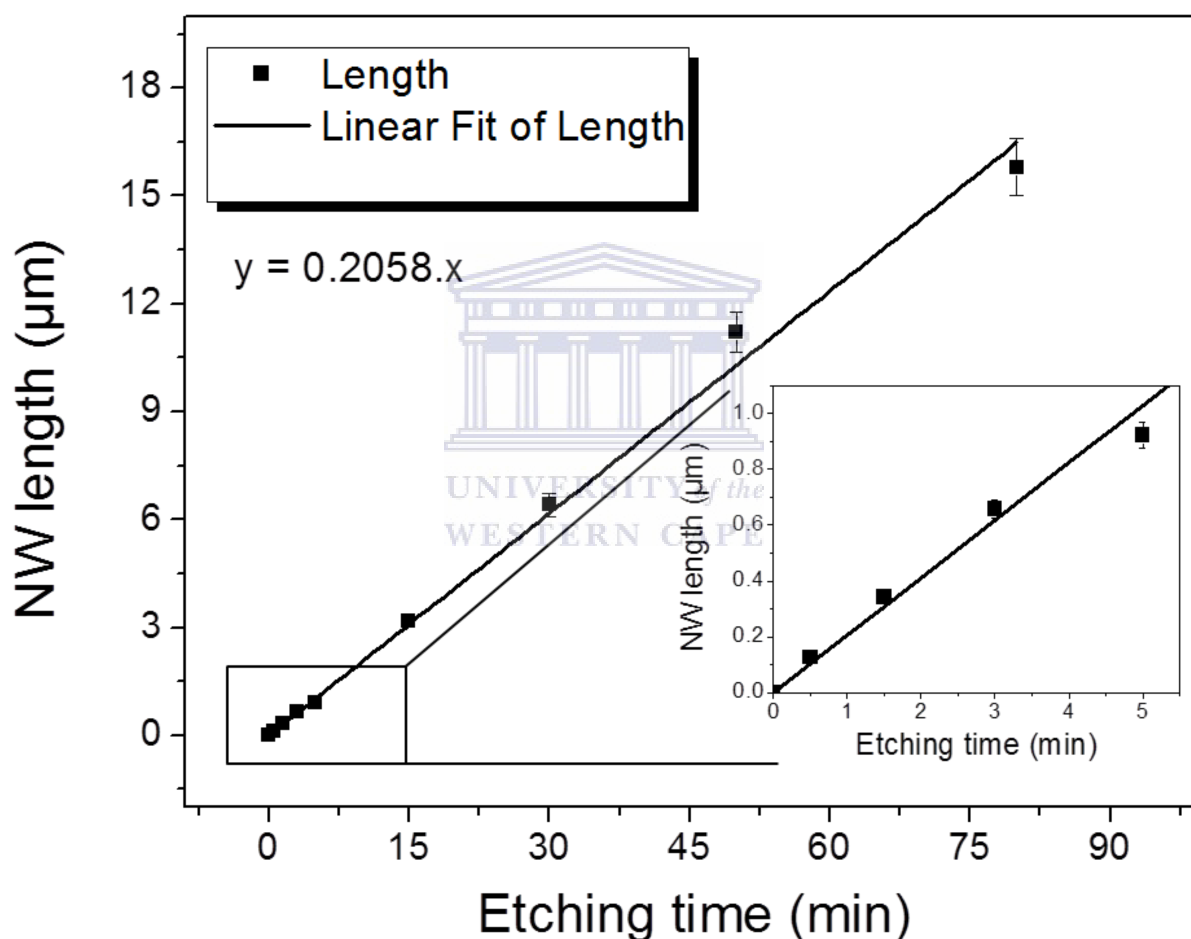

Figure 4.11: Relation between silicon nanowires length and etching time from 30 seconds to 80 minutes, the insert shows the confined points from shorter etching time durations.

The silicon nanowires have rough surfaces at their tips, especially the structures obtained after extended etching times. The tips referred to here are the top regions of the nanowires

where the etching begins. Figure 4.12 (a) shows the SEM micrograph of these rough-edged SiNW tips, obtained after 30 minutes of etching, whereas Figure 4.12 (b) shows the structures after 60 minutes etching. The roughness does not vary significantly between the two samples but for the 60 minutes etched sample the roughness proceeds axially down the nanowires unlike the 30 minutes nanowires, which appear smooth towards the bottom regions. Diameters measured for these nanowires were averaging at 105 ± 4 nm taken over both samples and there are no significant diameter variations within the nanowires length.

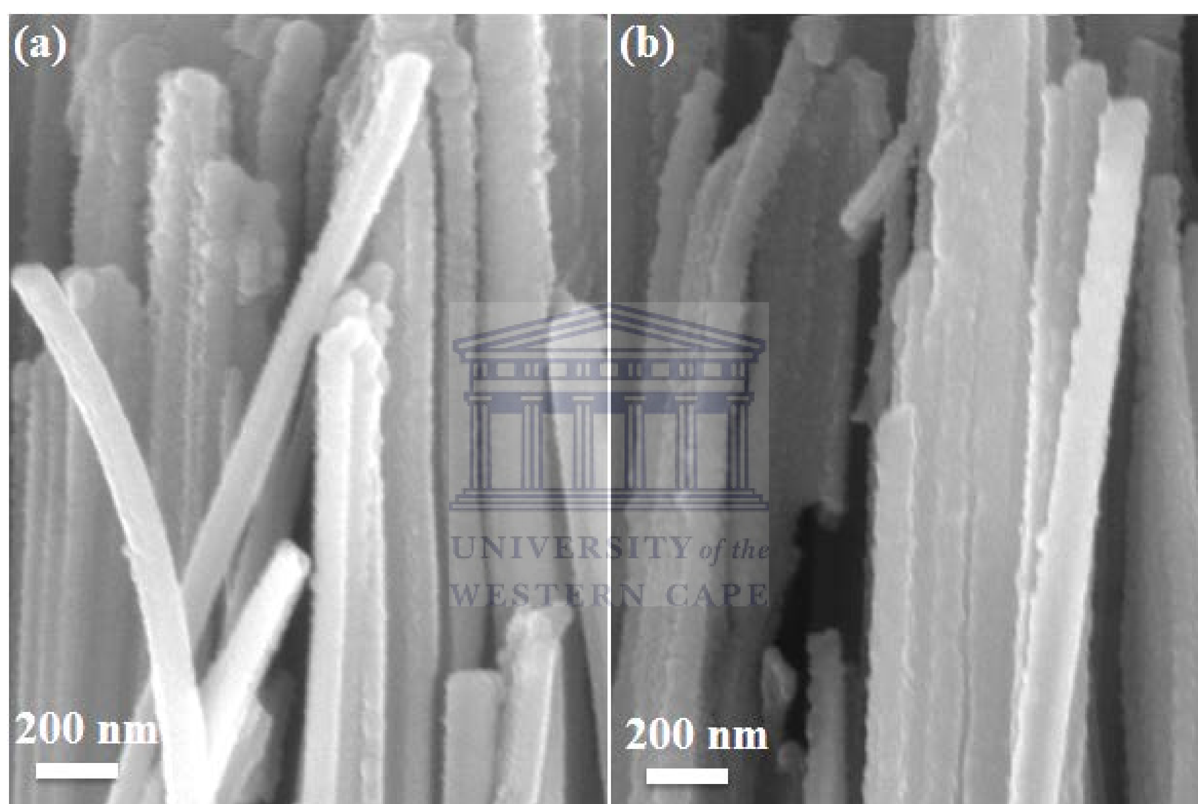

UNIVERSITY of the
WESTERN CAPE

Figure 4. 12: SEM micrographs of rough SiNWs tips, (a) after 30 minutes etching and (b) 60 minutes of etching time duration.

Transmission electron microscopy studies were also carried out to study the structure of individual nanowires. Figure 4.13 shows TEM micrographs of rough-edged tips of individual nanowires obtained after 60 minutes of etching. The roughness of the SiNWs has been reported in literature and is regarded as nano-pores, caused by long immersion times in the etching solution or high concentration of the oxidant [4.6, 4.12, 4.13]. During longer etching times or high oxidant concentrations, the AgNPs produce extra Ag ions (Ag^+) in the presence of H_2O_2 with some diffusing up the nanowire length and starting new nucleation centres on

the sidewalls of individual nanowires [4.6]. These rough structures are believed to be the centres of quantum confinement effects due to their small dimensions and they have effect on light trapping, which reduces reflection of light.

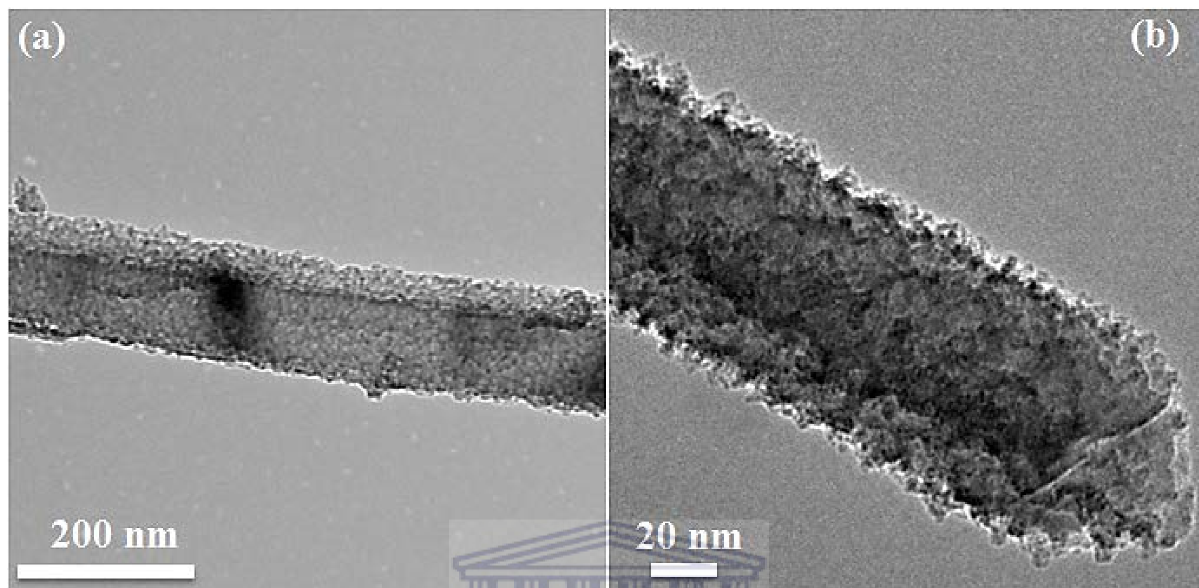

Figure 4.13: TEM micrographs for rough nanowires obtained after 60 minutes of etching, low magnification (a) and higher magnification (b).

UNIVERSITY of the
WESTERN CAPE

4.3.1.2 Effect of Oxidant Concentration on SiNW Formation

Shown in Figure 4.14 are the SEM micrographs of SiNWs synthesised from different H_2O_2 concentrations. A slight increase in nanowire length with an increase in oxidant concentration was observed, which saturated at very high concentrations. This relationship is plotted in Figure 4.15 with the line to aid eye added. Concentrations used were, as shown from Figure 4.14: (a) 0.1, (b) 0.5, (c) 1.5, (d) 2.5, (e) 3.5, and (f) 5 M. These concentrations produced nanowires lengths of about 1.3 ± 0.2, 2.4 ± 0.1, 3.3 ± 0.1, 2.5 ± 0.2, 2.6 ± 0.2, and 2.7 ± 0.3 µm, respectively. The HF concentration and etching time were kept constant at 5 M and 15 minutes, respectively, during this series of investigation.

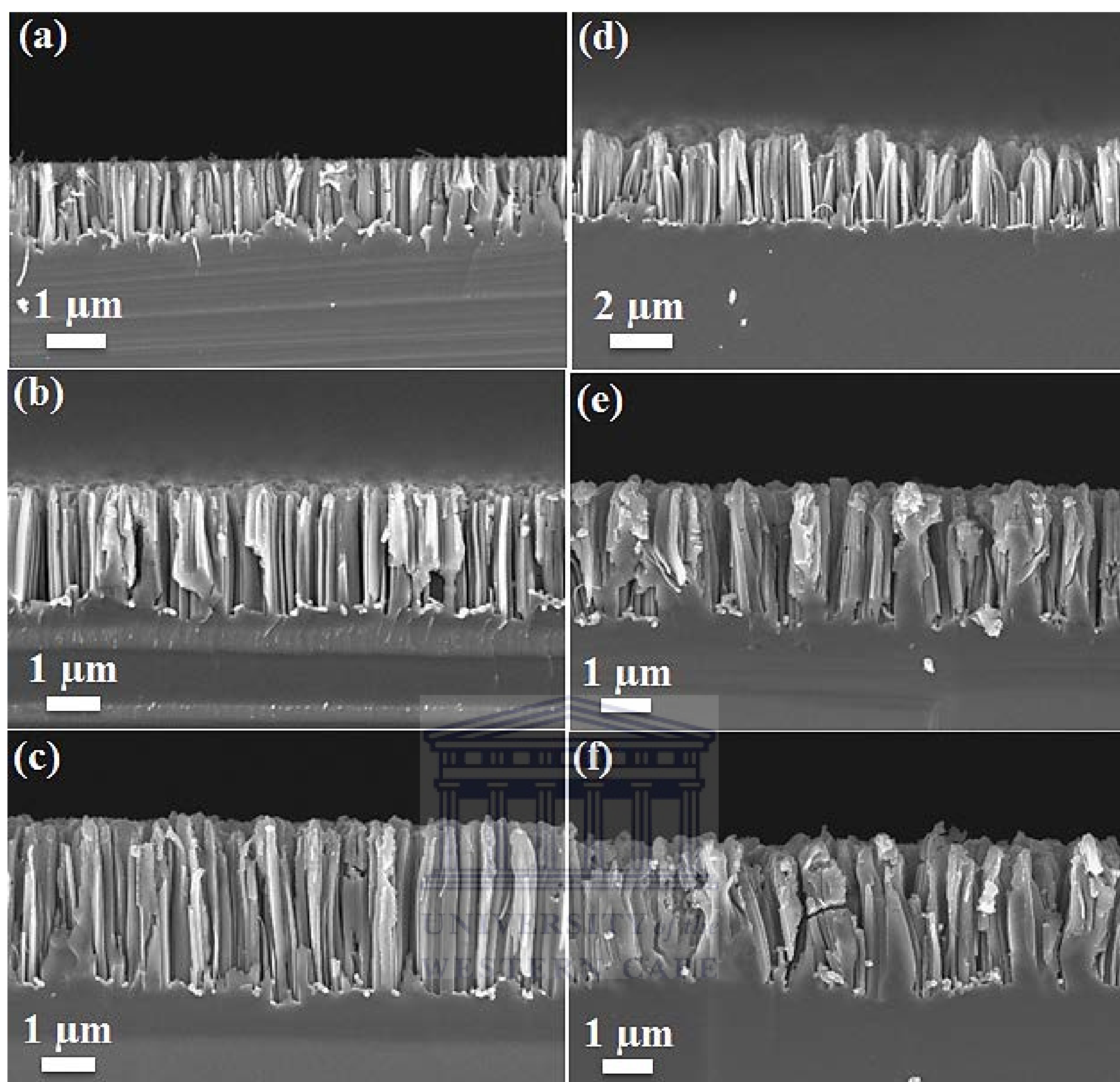

UNIVERSITY of the
WESTERN CAPE

Figure 4.14: SEM micrographs of silicon nanowires synthesised from different oxidant (H_2O_2) concentration. From (a) – (f) are the concentrations 0.1, 0.5, 1.5, 2.5, 3.5 and 5 M.

As shown in Figure 4.15, there was an increase in the etching rate for lower oxidant concentrations (0.1 – 1.5 M), however at greater concentrations the rate decreases. These changes in etching rates can be attributed to etching conditions where there is competition between oxidation of silicon and the dissolution of SiO_2 by HF.

The only scenario that can explain the observed curve in Figure 4.15 is based on the oxidation-dissolution differences. At low H_2O_2 concentration, oxidation of the Si to form SiO_2 occurs at a much slower rate due to the minuscule H_2O_2 species, whereas dissolution of

the formed oxide occurs at a much faster rate. As discussed in Chapter 2, the slow rate of SiO_2 formation, which is required for etching by the Ag to form the Si nanowire structure, in addition to the high dissolution of SiO_2 rate, combines to cause a breakdown in the nanowire formation and explains the nanowire length of 1.3 µm at a H_2O_2 concentration of 0.1 M. Conversely, when the oxidant concentration was increased significantly to 5 M, the oxidation proceeded a rate that the dissolution could not compete with; once again this results in a breakdown of the nanowire etch rate, which explains the structures observed in Figure 4.14 (f). It was thus found that a balanced concentration of HF (5 M) and H_2O_2 (1.5 M) provided a maximum oxidation-dissolution rate, producing longer nanowires.

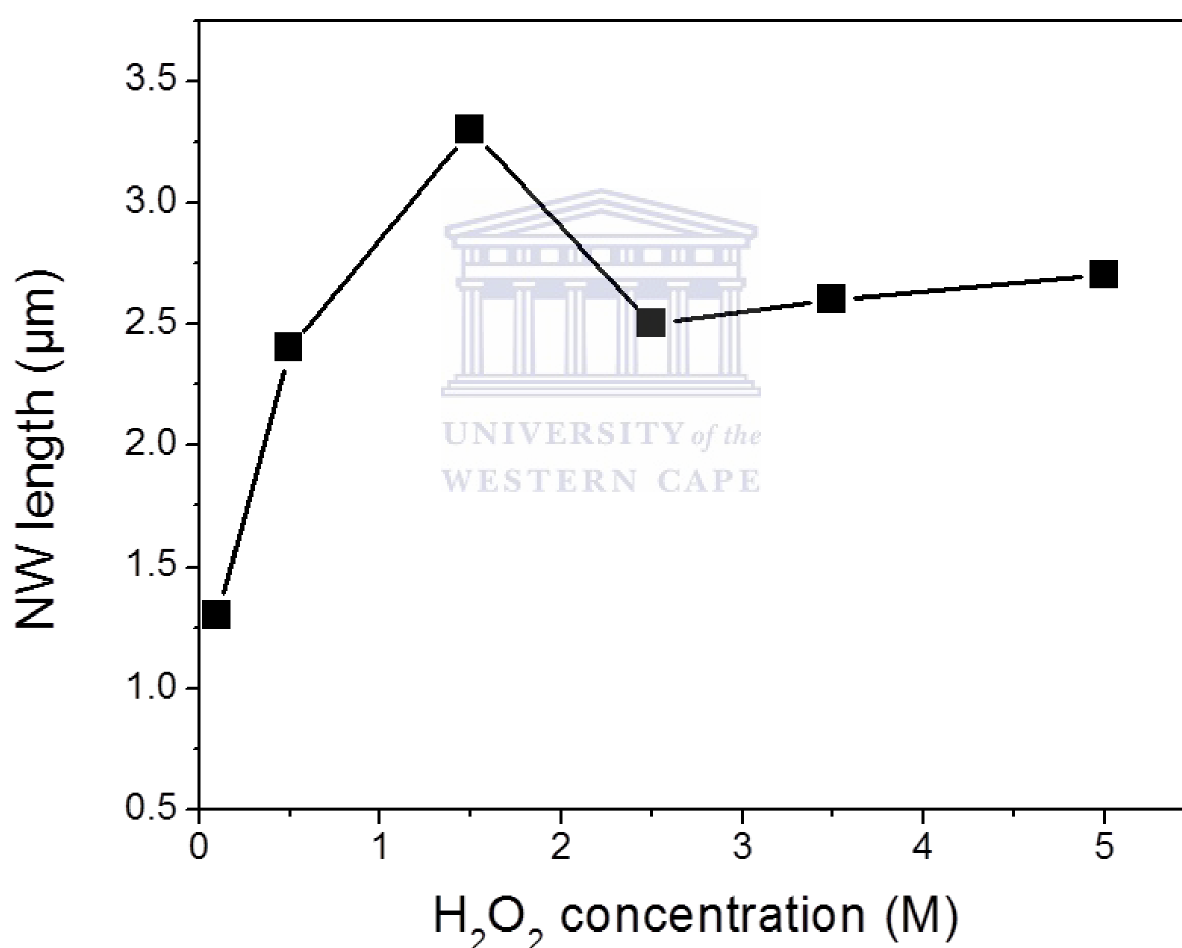

UNIVERSITY of the
WESTERN CAPE

Figure 4.15: Relationship between silicon nanowires length and the oxidant concentration.

A more linear relation was reported by Lin *et al*. [4.12] between the nanowires length and the oxidant concentration even though they used lower concentrations (0.1 – 0.5 M) of oxidant [4.4. 4.12]. In this study the synthesis seemed to stop when the concentration was increased

beyond 1.5 M based on the insignificant changes between concentrations of 2.5 and 5 M (2.5, 2.6, and 2.7 µm). The purpose here was to investigate the effect of H_2O_2 on the nanowires length upon increasing it and it seems like one has to find the balance between H_2O_2 and HF concentration as to obtain a balanced oxidation-dissolution which may yield longer nanowires. From these results it suffices to say that changing H_2O_2 concentration might not give control over the resulting morphology, unlike changing the etching time. These results also show that there is a threshold of synthesis when high concentrations of H_2O_2 are used whereas for etching time that threshold might be reached after long hours of etching as was discussed above in this section.

The SiNWs shown in Figure 4.14 appear to have larger bottoms than tops, and are densely packed, with small or no spaces in-between. A similar morphology was observed for nanowires obtained after long etching times of 50 and 80 minutes shown in Figure 4.10. These observations are even more dominant for SiNWs obtained from higher oxidant concentrations, Figure 4.14 (e) and (f). The reasons for the densely packed nanowires in Figure 4.14 may hence be similar to that discussed when obtaining dense structures at extended etching periods, i.e. the AgNPs sink down into branches or bundles instead of separate nanoparticles. The observed features might be due to different etched regions, in which some regions were probably etched faster than others, subsequently leading to the bigger AgNPs sinking at once in those specific regions and leaving bigger nanowires in between. These observations are valid because the Ag deposition was not patterned and thus the etching was self-selective and could not be perfectly controlled.

4.3.2 Crystal Structure of MaCE Synthesised SiNWs

The synthesised silicon nanowires were studied with high resolution transmission electron microscopy and x-ray diffraction during the investigation of their crystal evolution from bulk silicon. Figure 4.16 (a) shows a HR-TEM micrograph of a SiNW obtained after 30 minutes etching, depicting the planes along ⟨111⟩ direction based on interplanar spacing (d-spacing) which was found to be 0.341 nm. There is a disordered amorphous structure on the edge as shown in the image (selected area) and was due to natural oxidation of the nanowires and thus the amorphous layer can be of SiO_x form [4.7, 4.14]. These visible planes are not perpendicular to the axial direction of the nanowire (they are diagonal) which shows they are not possibly along the growth direction. Figure 4.16 (a) together with the selected area

UNIVERSITY of the WESTERN CAPE

electron diffraction pattern in Figure 4.16 (b) confirm that the SiNWs are single crystalline with a crystal growth direction along the ⟨111⟩ direction and a diamond cubic structure.

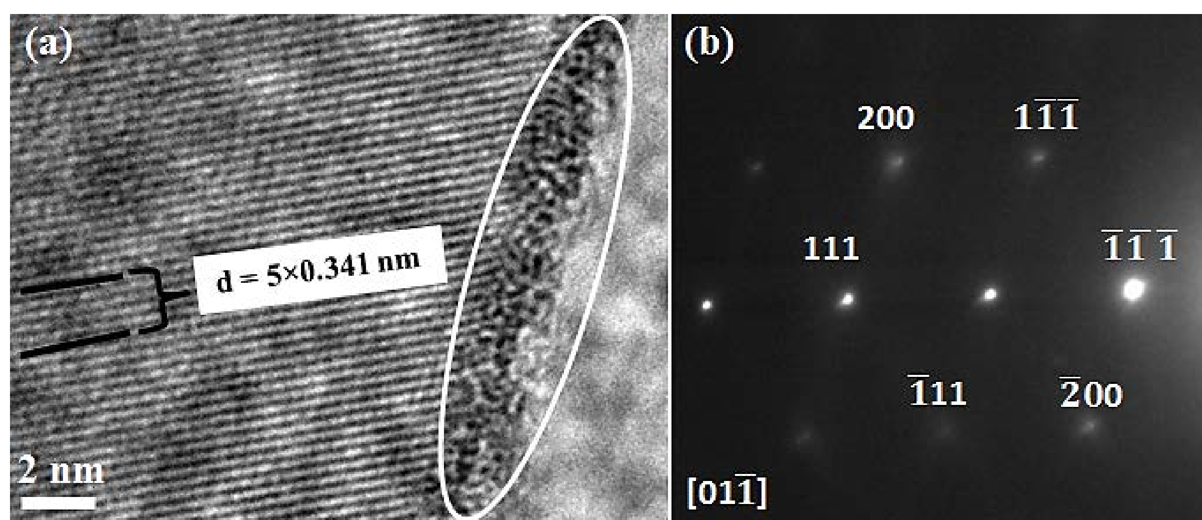

Figure 4.16: Single crystal silicon nanowire with planes along ⟨111⟩ in (a) and SAED pattern with zone axis along $[01\bar{1}]$ direction (b).

UNIVERSITY of the
WESTERN CAPE

The crystallinity of single silicon nanowires compared to the bulk array of wires was studied using XRD. Figure 4.17 shows XRD patterns of SiNWs versus that of the bare Si substrate prior to Ag deposition or etching. An intense peak can be observed at about 2θ ~ 69° attributed to Si (400) and is related to Si (100) substrate, as shown in Figure 4.17 (a). There was not much of a difference between different nanowires samples, however high peak intensity was observed for nanowires sample as compared to bulk Si. The peak intensity variations, as can be clearly seen on the Si (200) peak situated at 2θ ~ 33°, suggest high quality crystalline nanowires [4.15, 4.16].

This high intensity might also be depicting that for nanostructures the x-ray beam interacts differently as it does to the bulk substrate due to reduced dimensions. The high intensity peaks led to some speculation regarding the broad hump observed around 10 – 40° 2θ angles, mostly clear in the pattern of the SiNWs samples and had previously been related to amorphous silicon [4.17]. However, this feature is regarded as speculation because the amorphous matrix peaks usually appear prominent at 2θ between 10 – 20°, whereas in Figure 4.17 (b) it starts appearing at 2θ approximately 40°, which could be due to instrumental broadening. Even though these results are unclear they can also be related to what was

observed on the HR-TEM micrographs where an amorphous layer was observed around the fringes of the single SiNWs.

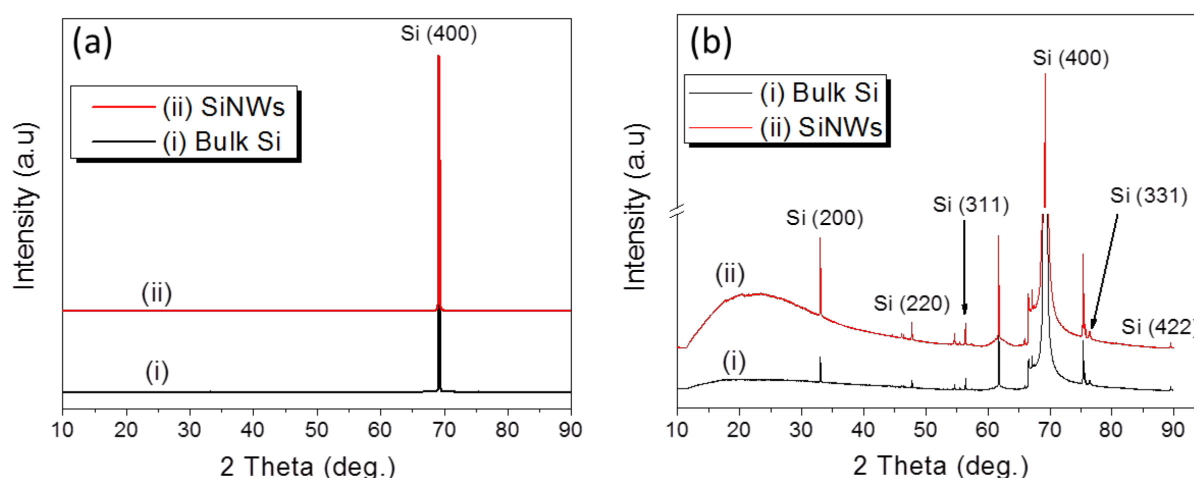

Figure 4.17: X-ray diffraction patterns for silicon nanowires and bulk Si. At (a) is the intense Si peak and (b) are other low intense peaks depicting a varying intensity from the Si (200) diffraction peak.

Raman scattering (RS) studies also show the high quality crystallinity of the SiNWs synthesised via MaCE with the intense c-Si peak at 520 cm^{-1} noticeable; see Figure 4.18. RS is one of the techniques used to non-destructively study the structural properties of materials [4.18]. The measurements were done for SiNWs samples and compared to that of the bulk, bare Si substrate. Figure 4.18 (a) shows high the intensity first order phonon peak at 520 cm^{-1} for silicon nanowires synthesised for 15 and 60 minutes and is compared to that of bulk Si. As can be seen in Figure 4.18 (a), there is an increase in the intensity of the 520 cm^{-1} peak, which is related to good crystallinity. Again 2 samples of silicon nanowires are discussed as no significant changes were observed when analysing specimens synthesised from different oxidant concentrations or various etching times. As can also be observed in Figure 4.18 (b) the Raman spectrum for the SiNWs etched for 60 minutes show a bump at about 430 cm^{-1} which is related to amorphous Si [4.19]. This small hump as compared to high intense c-Si peak shows that the SiNWs have a crystalline core with probable a thin layer of amorphous SiO_x in agreement with what was observed in the TEM micrograph of Figure 4.16 (a).

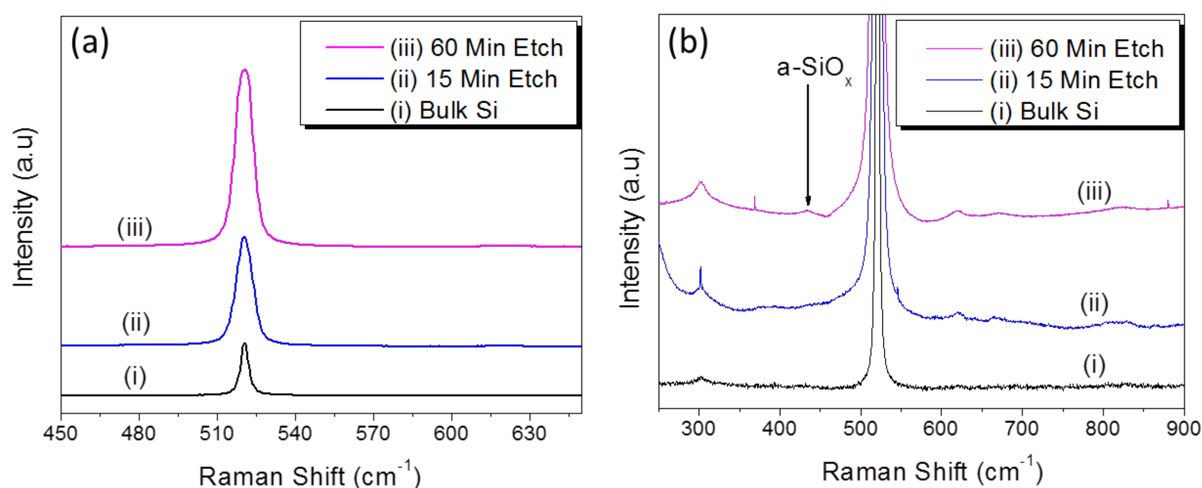

Figure 4.18: Raman scattering spectra of SiNWs as compared to that of bulk Si. (a) shows a c-Si peak at 520 cm^{-1} for SiNWs and bulk Si and (b) shows an amorphous SiO_x present on the nanowires, sample (iii).

There RS peak intensity was also related to light localisation effect (light trapping) in SiNWs as compared to bulk Si [4.20]. The high intensity of the c-Si Raman peak shows that SiNWs have good light trapping ability due to their reduced dimensions and vertical alignment, which result in multiple light scattering. It can also be observed in the Raman spectra that the 520 cm^{-1} peak broadens with an increase in etching time, as shown in Figure 4.18 (a) and broadens asymmetrically towards lower frequency as depicted in Figure 4.18 (b). Summary of the peak position and FWHM are shown in Table 4.1 for different SiNWs samples compared to that of bulk Si.

UNIVERSITY of the
WESTERN CAPE

Table 4.1: Peak position and FWHM of bulk Si and the SiNW samples synthesised at different etching times. Results from Gaussian peak fitting information.

Sample type	peak position (cm^{-1})	FWHM (cm^{-1})
Bulk Si	520.4 ± 0.03	3.6
15 minutes	520.5 ± 0.01	7.4
60 minutes	520.3 ± 0.02	7.8

There are different reasons for the observed features, including local heating induced by the Raman laser during measurements, tensile stresses due to an oxide layer [4.21] and phonon confinement [4.18]. Heating is only noticeable if laser power used is more than 2.5 mW

[4.22] and during these nanowires Raman measurements 1.21 mW was used, so this effect cannot be accountable for the peak broadening. The effect of phonon confinement as probed by Raman scattering also is not supposed to be observed in SiNWs with diameters greater than 20 nm [4.18]. As mentioned previously, the nanowires discussed here had diameters of 50 nm or more, however, even though the synthesised SiNWs have diameters beyond the phonon confinement regime, they do possess roughness (or porosity) with nanocrystals of 10 nm or less as was shown by the TEM micrographs in Figure 4.13, which could be phonon confinement centres. As such, this effect together with the thin native oxide layer could be the dominating reasons behind the observed asymmetric peak broadening of the first order optical phonon peak at 520 cm^{-1}.

4.3.3 Surface Passivation of MaCE Synthesised SiNWs

It was discussed in Chapter 2 metal assisted chemical etching involves the breaking of silicon back bonds which might be along the (100) planes if the starting wafer is Si (100). Breaking of bonds might leave free dangling bonds on the surface of these silicon nanowires, which can easily oxidise if not passivated. Fourier transform infrared spectroscopy was used to study the surface bonding with observations supported by the studies done during EDS measurements in the electron microscopy. FTIR measurements were taken from 400 – 4000 cm^{-1} but only the region with prominent peak will be discussed. All the samples were dipped into dilute (5%) aqueous HF solution prior silicon nanowire synthesis including the bulk silicon wafer to remove the native oxide layer on the surface and terminate the dangling bonds with hydrogen (H-termination) [4.23]. All samples were dipped for the same time before FTIR measurements to keep equal exposure duration in air for both bulk Si and SiNWs.

UNIVERSITY of the WESTERN CAPE

Figure 4.19 (a) shows FTIR spectra of SiNWs sample together with that of bulk Si for comparison. The spectra shows three intense peaks at 610, 665, and 1106 cm^{-1} assigned to Si-Si stretching [4.24], Si-H_2 wagging [4.25], and Si-O-Si asymmetric stretching bond vibrations [4.26], respectively. There are differences in the two spectra (bulk Si and SiNWs) and also variations between peaks of the same sample. The Si-Si peak obviously shows the bonding of Si atoms which are present in the samples, the Si-H_2 shows the presence of hydrogen on the surface due to H-termination step and lastly the Si-O-Si shows the presence of oxygen bonded to Si due to natural oxidation.

Due to the removal of the native oxide layer on the samples the Si-H_2 was visible but the Si-O-Si on the bulk Si sample was observed to be low. The sample of SiNWs had a high intense and broad Si-O-Si peak showing a different degree of oxidation compared to bulk Si which might be due to etched structures where dangling bonds easily trap oxygen from air. It was reported by Sun *et al*. [4.27] that even though SiNWs were terminated with hydrogen they started oxidising after few days (about 3 days after) depicting that hydrogen passivation was not a long term solution.

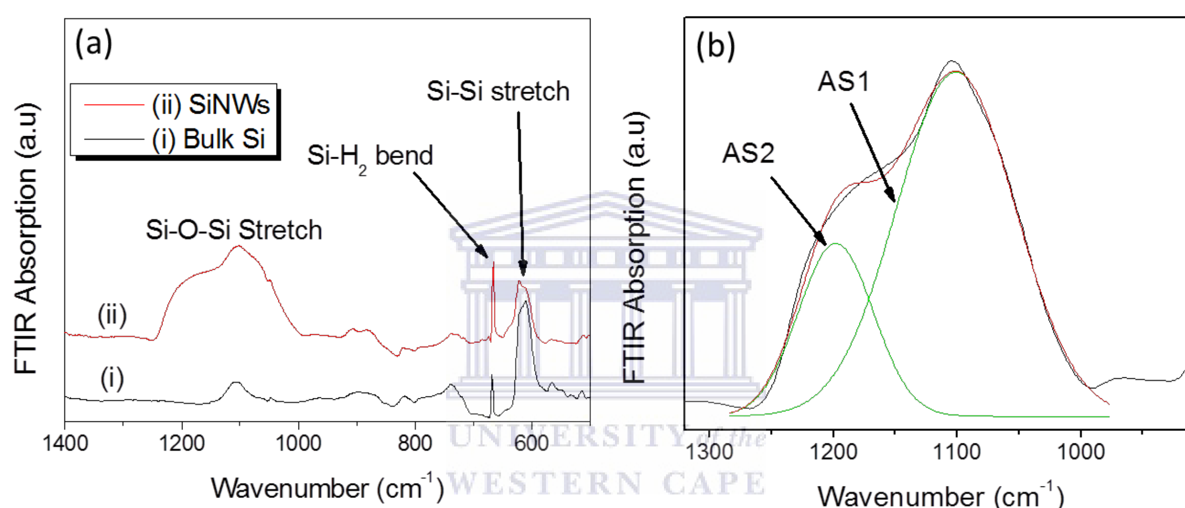

UNIVERSITY of the
WESTERN CAPE

Figure 4.19: FTIR spectra of SiNWs together with bulk Si. (a) shows full spectra with intense peaks assigned to the labelled vibrations, (b) shows a deconvolution of the Si-O-Si asymmetric stretching vibration peak.

Figure 4.19 (b) shows a deconvolution of the Si-O-Si peak with two peaks, one centred at about 1106 cm^{-1} and the other at about 1200 cm^{-1} attributed to asymmetric stretching (AS) vibrations of Si-O-Si bonds. These two peaks are separated into asymmetric stretching 1 (AS1) at lower wavenumber (1106 cm^{-1}) and asymmetric stretching 2 (AS2) at higher wavenumber (1200 cm^{-1}) in which the oxygen atom execute different motions of vibration. During the asymmetric stretching vibration the oxygen atom moves back and forth between the two silicon atoms parallel to the line of bonding axis. AS1 results from the motion of the adjacent oxygen atoms moving in phase with one another and at AS2 the oxygen atoms move

180° out of phase with one another [4.21]. The AS2 broadening is only present in SiNWs which showed changes in oxidation degree as compared to bulk Si. This type of oxidation can be related to the amorphous silicon oxide (a-SiO_x, x = 1 to 2) matrix embedded in the surface of crystalline SiNWs observed in HR-TEM. The existence of the a-SiO_x was also confirmed during the x-ray diffraction and Raman scattering studies of silicon nanowires where amorphous features were observed and only realised to be of SiO_x structure.

Similar peak shapes have been observed previously on SiO_2 glasses and thin films [4.21]. Disordered amorphous (long, or short range) structure of SiO_x (x = 1 or 2) could reduce carrier lifetimes due high surface states defects resulting to non-radiative recombination and lead to bad conduction in solar cell applications [4.15]. Stable surface passivation is thus required for SiNWs as to make them good candidate for solar cells. There was nothing observed at higher wavenumber (around 2000 – 2100 cm^{-1}) where high intensity peaks had been reported attributed to Si-H_x (x = 1, 2, or 3) [4.28].

Further results confirming that the oxidation of these nanowires was due to air exposure were observed during EDS measurements. EDS results showed that the oxygen amount was high on the SiNWs tips compared the bottom (SiNWs/Si interface) depicting that oxidation did not occur during the synthesis. Figures 4.20 (a) and (b) show SEM micrographs where the EDS was taken and (c) and (d) shows the EDS spectra. It was observed that the oxygen amount increased towards the nanowires tips in which, if the oxidation was due to synthesis there would be more oxygen at the bottom than top or it would be the same everywhere. However, that cannot be the case because the formed SiO_2 during synthesis get dissolved by HF. It was reported by Lin *et al*. [4.12] that dipping the samples in nitric acid (HNO_3) induces oxidation, which was the case in this study for effective removal of the AgNPs post SiNW etching. However, if HNO_3 did induce oxidation it would be the same along nanowires length, which is not the case in this work as shown by the EDS results, which suggests that HNO_3 does not induce much with the only source of oxidation being air exposure.

UNIVERSITY of the
WESTERN CAPE

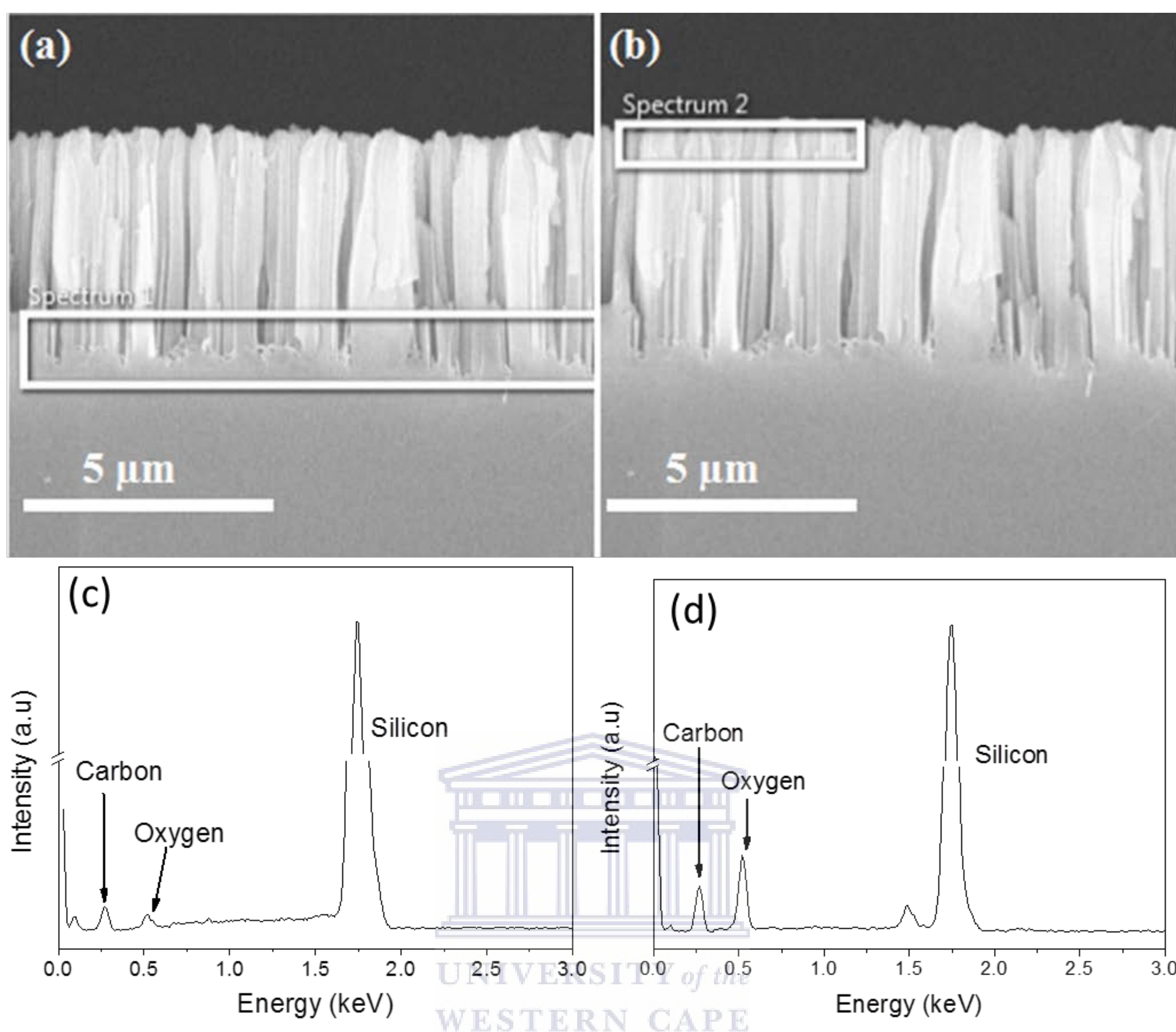

Figure 4.20: EDS results showing varying amount of oxygen with SiNWs. (a) and (b) are the SEM micrographs with EDS spots and (c) and (d) are the corresponding spectra.

An elemental composition of an individual nanowire was done using scanning transmission electron microscopy coupled with high-angular annular dark-field (STEM-HAADF) imaging, which mapped the nanowire according to its elemental composition. Figure 4.21 (a) shows a STEM-HAADF micrograph together with three most noticeable mapped elements which were present in the SiNWs. Figure 4.21 (b) shows the obvious element silicon which was also observed with high peak intensity in the EDS spectra.

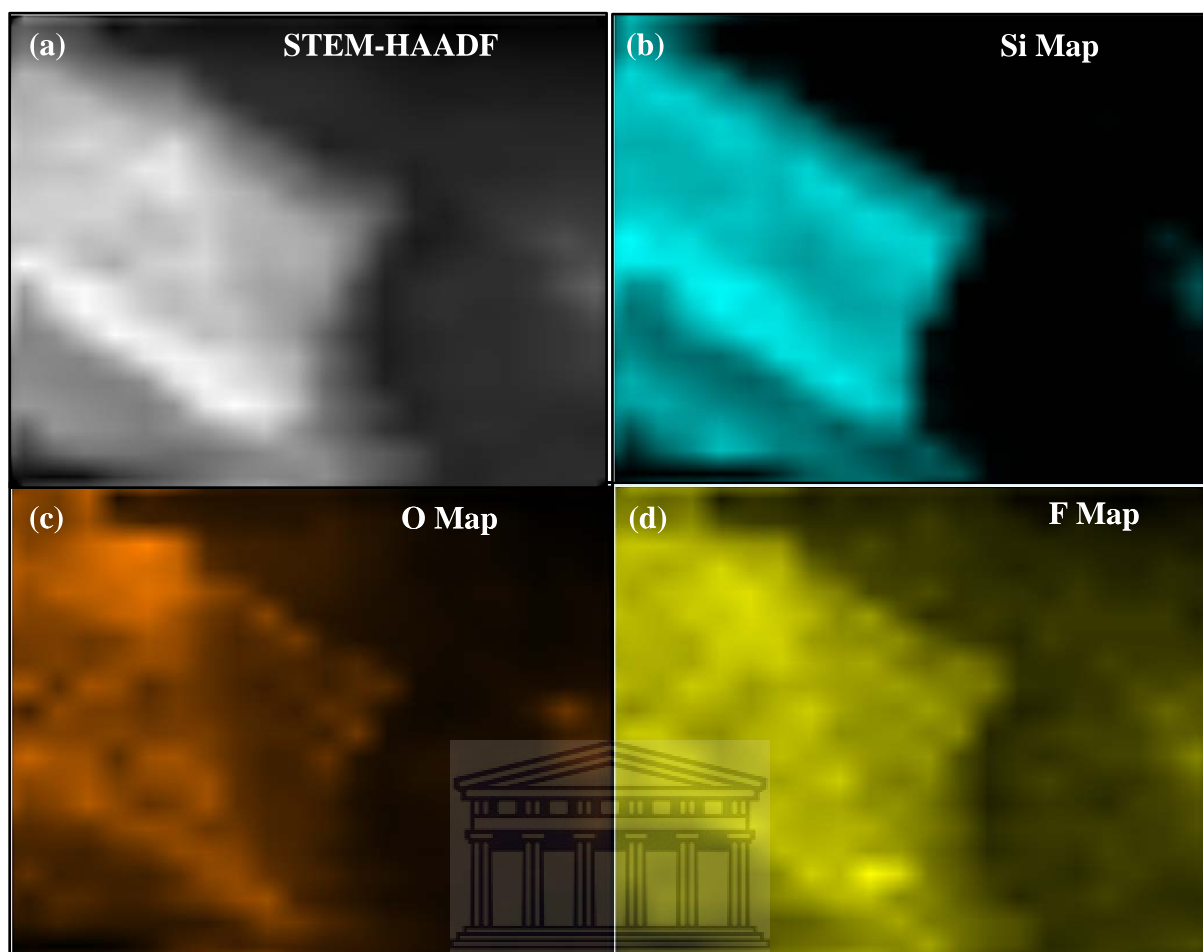

UNIVERSITY of the
WESTERN CAPE

Figure 4.21: Element mapping of an individual nanowire. (a) is the STEM-HAADF micrograph, (b) silicon map, (c) oxygen map, and (d) is the fluoride map, all showing elementary variation within the nanowire.

Oxygen and fluoride maps were also collected as shown in Figure 4.21 (c) and (d), respectively. Silicon map is clearer because the nanowires are from etched Si substrates, traces of fluoride are also clearly visible and that is due to the fluoride species available in HF and maybe the sample was not thoroughly rinsed with water after SiNW synthesis. The oxygen map was found to be fainter than the two mentioned elements and the presence of it adds to the idea of oxidation that the nanowires suffer during post synthesis. These results again depict the partial oxidation of these nanowires as the ratio of oxygen to silicon seems very low as seen from these maps and the EDS spectra.

4.3.1 Optical Reflectance of MaCE Synthesised SiNWs

As synthesised silicon nanowires by metal assisted chemical etching showed a black appearance from naked eye observations with a rough texture as compared to shiny polished silicon substrates. These characteristics form part of the motivation towards the intense research in SiNWs as antireflection layers for photovoltaic applications. SiNWs synthesised through MaCE have morphologies similar to sub-wavelength structures (SWS) used as antireflection layers in thin film solar cells [4.29] because they possess diameters of 50 – 200 nm and are less than the wavelength of incident light ranging between 300 and 800 nm.

UV-Vis spectroscopy measurements on silicon nanowires were taken in comparison with bulk silicon to cover the entire visible light range, from 200 to 1000 nm wavelength. The results were only plotted from 350 to 900 as to study the reflection properties of the nanowires in that range. It is known that crystalline silicon substrates transmit insignificant light in the visible range (300 – 900 nm) and the measured total reflection can be converted into absorption [4.15, 4.30]. However, specular and diffuse reflection measurements were done separately in this study and thus the reflection measurements could not be directly converted to absorption. The discussion of results below will look at the obtained reflection.

UNIVERSITY of the
WESTERN CAPE

Figure 4.22 shows a specular reflection curve of SiNWs synthesised at different etching times compared to bulk c-Si. The nanowires show well reduced reflection with average reflection below 10% as compared to their bulk counterparts which have reflections above 30%. Bulk Si has a shiny surface and thus reflects light specular while rough nanowires attain low specular reflection. The roughness of SiNWs was shown during morphology discussions earlier in this chapter and that can be related to the low reflection showed by longer nanowires (15 minutes etched) compared to shorter nanowires (5 minutes etched). Reflections of about 1.3% was measured at 500 nm for a 15 minutes etched sample compared to 4.3% measured for 5 minutes etched and about 38% for bulk Si at the same wavelength. These results show that longer and rougher SiNWs specular reflect the least amount of light, which was also observed during measurements of even longer nanowires (30 minutes etched) where no results were obtained due to the low signal, depicting almost zero specular reflection. Reflection started increasing towards near infrared (900 nm) even more for 5 minutes etched sample. This can be related to the decrease in reflection observed for the bulk

Si substrate towards near infrared showing changes in specular reflection towards longer wavelength.

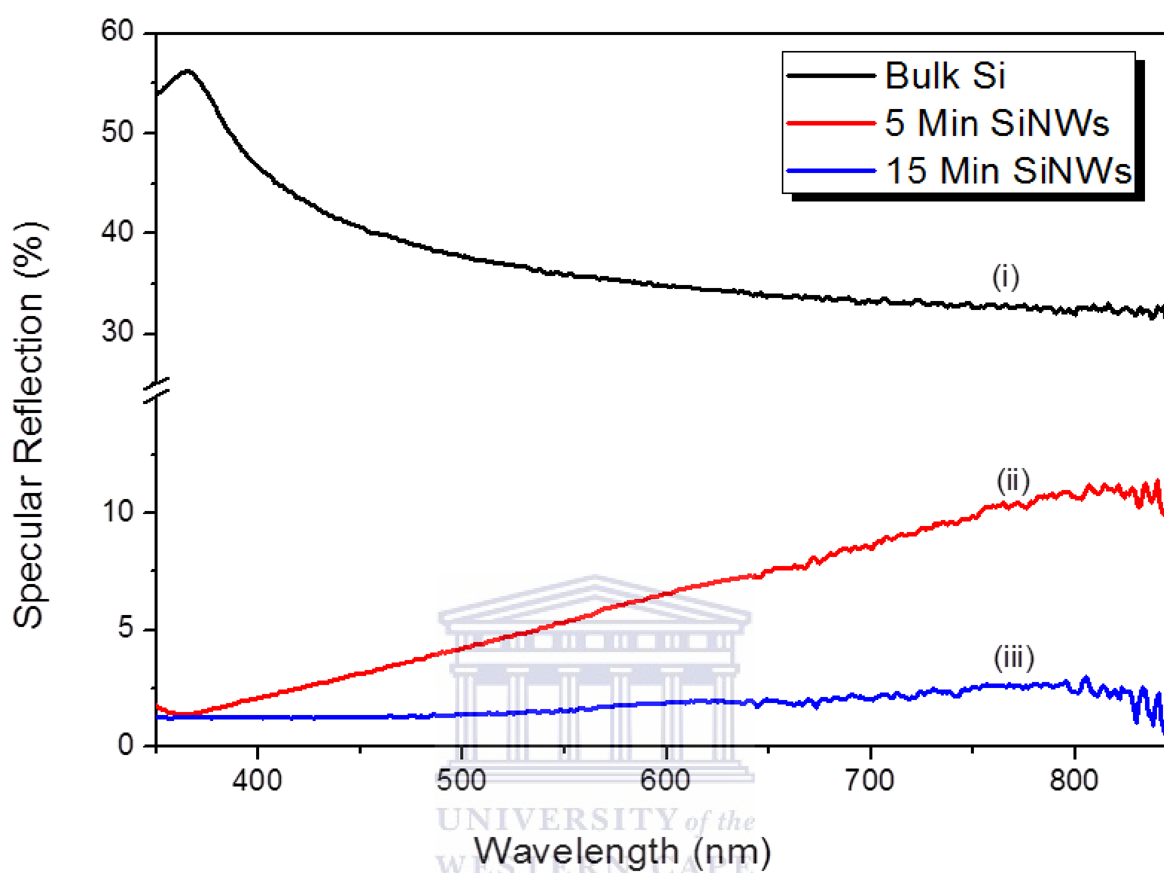

Figure 4.22: Specular reflection for SiNWs compared to that from bulk silicon over the visible wavelength range.

Diffuse reflection measurements were conducted and shown in Figure 4.23 for the low diffuse reflecting shorter SiNWs (15 minutes etched) compared to longer nanowires (30 minutes etched). Low light reflection of less than 10% was also observed even though the surface of the nanowires was rougher a characteristic feature of a diffuse reflecting surface than specular reflection. The fact that the rough surface has high diffuse reflection was confirmed by high light reflection in longer nanowires with reflection of about 7.4% at 500 nm wavelength compared to 5.9% for shorter nanowires at the same wavelength. The shape of the curve in Figure 4.23 was found to be different from that of the specular reflection and peaked at about 550 nm but started decreasing towards longer wavelengths. This shape was

observed by Liu *et al*. [4.31] and could be due to how light interaction with the nanowires at that range of wavelength due to reduced dimensions of SiNWs.

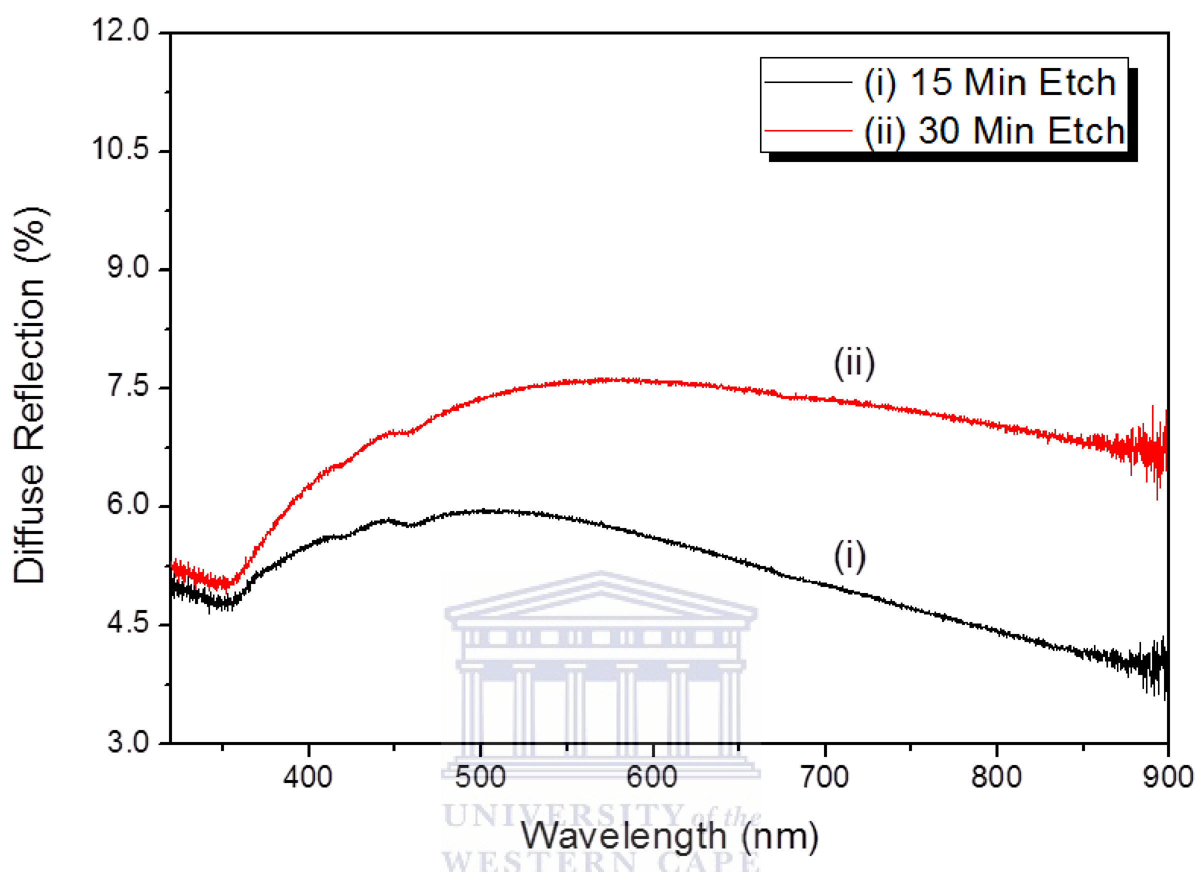

UNIVERSITY of the
WESTERN CAPE

Figure 4.23: Diffuse reflection measurements taken for SiNWs synthesised from 15 and 30 minutes etching.

There are a few factors responsible for the reduced reflection of SiNWs compared to bulk Si, with the reflection usually discussed in the context of total reflection in literature. It was mentioned earlier in this section that the silicon nanowires are similar to subwavelength structure due to the reduced dimensions and their morphology (vertical and rough). Rough and longer SiNWs causes multiple light scattering events during incident light interaction with SiNWs. This strong light scattering ability results in intense light absorption [4.29]. SiNWs also have strong light trapping ability due to the effective path travelled by light when incident on the array of nanowires. This path length was also observed to be more than that found for thin films of the same thickness [4.32, 4.33]. The effective path length travelled by light within nanowires could be one of the reasons longer SiNWs possesses enhanced absorption compared to shorter wires. The effect of light localisation (light trapping) was also

observed during Raman scattering studies of SiNWs where the Raman scattering intensity was found very high for samples of SiNWs as compared to bulk Si.

During the synthesis of SiNWs through MaCE the silicon wafer is etched which means some parts of the solid silicon will be dissolved into an etching solution leaving free standing SiNWs on top of bulk Si. This means that the atomic density per unit area on the silicon nanowires layer will be less than that of bulk silicon in which these possess the same crystallinity (as found during XRD results), thus light will interact within the two layers differently. It was reported in literature that the refractive index "n" of SiNWs is less than that of bulk Si, ($n \approx 1.26$ for SiNWs and $n \approx 3.5$ for bulk Si [4.34]), which also depict different layers of different structures. Silicon nanowire's refractive index act as a medium between air ($n \approx 1$) and bulk Si in which the transition of refractive index from air to bulk Si causes the reduced reflection in SiNWs compared to bulk Si [4.34]. Due to the graded refractive index in SiNWs these structures have the ability to act as antireflective layers, improving light absorption in crystalline silicon.

It was observed during SEM studies that these nanowires have porous surfaces in which the porosity increased for nanowires obtained from longer etching times and was even higher on the nanowire's tip (Figure 4.12). Changes in porosity of these nanowires from top to bottom causes a high quality refractive index layer where the refractive index increases with decreasing porosity resulting in high absorption of light [4.29], therefore this novel, graded refractive index of the SiNWs layer provides the basis for the reduced reflection of light which can be related to good light absorption.

UNIVERSITY of the
WESTERN CAPE

4.4 Conclusion

Silver nanoparticles were deposited at various deposition times and $AgNO_3$ concentrations. It was observed that the shape and diameter of AgNPs change upon changing the deposition conditions with the shape changing from brain like shapes to semi-spherical and spherical and finally dendritic structures at high $AgNO_3$ concentrations. The diameters were ranging from about 75 nm when low concentrations were used to about 170 nm at high concentrations. Diameters of AgNPs were also changing for different deposition times. The

increase in diameter was attributed to the high concentration of Ag^+ ions at higher silver nitrate concentrations and longer deposition times allowed more of these ions to be deposited on previously formed silver nuclei during nucleation of AgNPs and that led to those nanoparticles growing large. Finally, AgNPs deposited for 30 seconds at 20 mM concentration provided spherical and densely packed nanoparticles and that condition was used to synthesise SiNWs.

The AgNPs coated samples were immersed in an etching solution containing HF + H_2O_2 + H_2O for the synthesis of silicon nanowire. Different etching conditions were investigated, i.e. etching time duration and different oxidant (H_2O_2) concentrations. SiNWs grew longer with etching time and a more linear relation was observed at an etching rate of 206 nm/min and the length increased from 130 nm after 30 seconds to over 25 µm after 80 minutes. The linear increase was caused by more time provided for the oxidation-dissolution of the silicon underneath AgNPs. Different oxidant concentrations also resulted in an increase in nanowire length but higher concentrations resulted into shorter nanowires. Diameter of these nanowires was ranging between 50 and 200 nm with diameter modulation along the nanowires axial direction. AgNPs were observed lying at the SiNWs/Si interface depicting the synthesis mechanism of MaCE.

UNIVERSITY of the
WESTERN CAPE

The nanowires remained single crystalline covered by a thin layer of amorphous Si on the nanowire walls. The thin amorphous layer could be of SiO_x (x = 1 or 2) based on the observed surface passivation results where it was observed that these nanowires were mostly passivated with oxygen more than hydrogen. It was also observed that the oxidation was high on the surface of nanowires than it was at the bottom (near SiNWs/Si interface) showing that it did not happen during synthesis. Reduced reflectivity was observed for the nanowires with reflectivity of less than 10% over the entire visible range compared to the bulk Si which has a reflectivity of over 30% in the same range.

Reference

[4.1] L. Zeng, X. Yu and D. Yang, Journals of Nanomaterials **2012** (2012) 156986 – 156992.

[4.2] K. Tomsia, F. Xie and E. Goldys, Journals of Physical Chemistry C **114** (2010) 1562 – 1569.

[4.3] Z. Smith, R. Smith and S. Collins, Electrochimica Acta **92** (2013) 139 – 147.

[4.4] K. Peng, R. Zhang and S. Lee, Advanced Functional Material **18** (2008) 3026 – 3035.

[4.5] H. Fang, Y. Wu, J. Zhao and J. Zhu, Nanotechnology **17** (2006) 3768 – 3774.

[4.6] Y. Qu, L. Liao, Y. Li, H. Zhang and X. Duan, Nano Letters **9** (2009) 4539 – 4543.

[4.7] M. Zhang, K. Peng, X. Fan, J. Jie, R. Zhang, S. Lee and N. Wong, Journals of Physical Chemistry C **112** (2008) 4444 – 4450.

[4.8] F. Bai, M. Li, D. Song, H. Yu, B. Jiang and Y. Li, Journals of Solid State Chemistry **196** (2012) 596 – 600.

[4.9] D. Wang, R. Ji, A. Albrecht and P. Schaaf, Nanoscale Research Letters **8** (2013) 42 – 51.

UNIVERSITY of the
WESTERN CAPE

[4.10] K. Morton, G. Nieberg and S. Chou, Nanotechnology **19** (2008) 345301 – 345306.

[4.11] C. Chartier, S. Bastide and C. Clement, Electrochimica Acta **53** (2008) 5509 – 5516.

[4.12] L. Lin, S. Guo, J. Feng and Y. Wang, Nanoscale Research Letters **5** (2010) 1822 – 1828.

[4.13] S. Wu, T. Zhang, R. Zheng and G. Cheng, Applied Surface Science **258** (2012) 9792 – 9799.

[4.14] W. Chern, K. Hsu, I. Chun, B. De Azeredo, N. Ahmed, K. Kim, J. Zuo, N. Fang, P. Ferreira and X. Li, Nano Letters **10** (2010) 1582 – 1588.

[4.15] S. Razek, M. Swillam and N. Allam, Journal of Applied Physics 115 (2014) 194305 – 194313.

[4.16] A. Hochbaum, D. Gargas, Y. Hwang and P. Yang, Nano Letters **9** (2009) 3550 – 3554.

[4.17] K. Surana, H. Lepage, J. Lebrun, B. Doisneau, D. Bellet, L. Vandroux, G. Carval, M. Baudrit, P. Thony and P. Mur, Nanotechnology **23** (2012) 105401 – 105407.

[4.18] S. Piscanec, M. Cantoro, A. Ferrari, J. Zapien, Y. Lifshitz, S. Lee, S. Hofmann and J. Robertson, Physical Review B **68** (2003) 241312 – 241315.

[4.19] I. Iatsunskyi, S. Jurga, V. Smyntyna, M. Pavlenko, V. Myndrul and A. Zaleska, Proceedings of SPIE **9132** (2014) 913217 – 913223.

[4.20] V. Timoshenko, K. Gonchar, L. Golovan, A. Efimova, V. Sivakov, A. Dellith and S. Christiansen, Journal of Nanoelectronics and Optoelectronics **6** (2011) 519 – 524.

[4.21] S. Toda, T. Oishi, T. Yoshioka and T. Okuno, Japanese Journal of Applied Physics **49** (2010) 095002 – 095008.

[4.22] R. Wang, G. Zhou, S. Pan and Z. Zhang, Physical Review B **61** (2000) 16827 – 16832.

[4.23] J. Song, Y. Nam, M. Park, S. Shin, R. Wehrspohn and J. Lee, RSC Advances **5** (2015) 39177 – 39181.

[4.24] D. Mawhinney, J. Glass Jr. and J. Yates Jr, Journal of Physical Chemistry B **101** (1997) 1202 – 1206.

[4.25] I. Leontis, A. Othonos and A. Nassiopoulou, Nanoscale Research Letters **8** (2013) 383 – 389.

[4.26] C. Kirk, Physical Review B **38** (1988) 1255 – 1273.

[4.27] X. Sun, S. Wang, D. Ma and S. Lee, Inorganic Chemistry **42** (2003) 2398 – 2404.

[4.28] W. Salcedo, F. Fernandez and E. Galeazzo, Brazilian Journal of Physics **27** (1997) 158 – 161.

[4.29] S. Srivastava, D. Kumar, P. Singh, M. Kar, V. Kumar and M. Husain, Solar Energy Materials & Solar Cells **94** (2010) 1506 – 1511.

[4.30] K. Liu, S. Qu, X. Zhang and Z. Wang, Nanoscale Research Letters **8** (2013) 88 – 93.

[4.31] Y. Liu, X. Liang, Z. Zuo and Y Shi, Nanoscale Research Letters **7** (2012) 663 – 671.

[4.32] T. Pei, S. Thiyagu and Z. Pei, Applied Physics Letters **99** (2011) 153108 – 153110.

[4.33] L. Tsakalakos, J. Balch, J. Fronheiser, M. Shih, S. LeBoeuf, M. Pietrzykowski and U. Rapol, Journal of Nanophotonics **1** (2007) 013552 – 013562.

UNIVERSITY of the
WESTERN CAPE

[4.34] Z. Guo, J. Jung, K. Zhou, Y. Xiao, S. Jee, S. Moiz and J. Lee, Proceeding of SPIE **7772** (2010) 77721C – 77727C.

CHAPTER FIVE

Conclusion and Recommendations

This study was carried out to investigate the mechanism formation of silicon nanowires during metal assisted chemical etching. This technique involves a deposition of metal nanoparticles and then the samples coated with nanoparticles are immersed into an etching solution containing an oxidant (H_2O_2). These one-dimensional nanostructures were investigated due to the potential promise they show for the application in photovoltaic technology which is the direct conversion of radiant energy to electrical energy. The study was conducted through electron microscopy (SEM and TEM), x-ray diffraction, Raman, infrared, and UV-Vis spectroscopy in which all the techniques aimed at investigating different aspects of the SiNWs. The results and discussions were delivered in Chapter Four and thus this conclusion extends from the one given in the previous chapter.

UNIVERSITY of the
WESTERN CAPE

Silver nanoparticles were successfully deposited on the substrate of silicon through the mechanism of electroless metal deposition during the immersion of cleaned Si substrates onto a solution of $HF/AgNO_3/H_2O$. The deposition continued until the silicon samples were removed from the solutions and rinsed with deionised water. Morphologies of the particles revealed that their growth depended entirely on the deposition time and $AgNO_3$ concentrations. Different diameters of these AgNPs were realised as deposited using different $AgNO_3$ concentrations and deposition time durations.

Diameters of 75 ± 1, 109 ± 3, and 102 ± 2 nm for immersion times of 15, 60, and 300 seconds, respectively, for a concentration of 5 mM were measured. Longer deposition times resulted into bigger AgNPs because longer deposition time provided more Ag^+ to be deposited on the surface of the already formed small Ag nuclei during the nucleation of AgNPs. Densely packed brain like nanoparticles obtained from shorter deposition times transformed into isolated semi-spherical shaped nanoparticles realised after longer deposition times and the transformation resulted into reduced nanoparticle diameters for 60 and 300 seconds deposition times.

An increase in $AgNO_3$ concentration resulted into an increase in AgNPs diameters with values averaging at 99.4 ± 0.7, 154 ± 4, and 141 ± 4 nm for a concentration of 20 mM with similar deposition times as for 5 mM. A change in morphology was observed again in these conditions where particles developed dendrite tree like structures after longer deposition time. These dendrite structures were observed to be on top of smaller nanoparticles and thus smaller diameter AgNPs were measured for longer time. Deposition time of 15 seconds in 20 mM concentration showed diameters that were almost the same as that of nanoparticles obtained from lower concentration but longer time depicting that an increase in both time and concentration resulted into an increase in nanoparticles diameter. These are both due to the high availability of Ag^+ ions and longer time for their deposition leading to bigger nanoparticles.

Higher $AgNO_3$ concentration of 50 mM resulted into even bigger nanoparticles and more tree like dendrite structures were observed covering the surface after longer deposition times. These AgNPs had average diameters of 170 ± 4 nm for 15 seconds deposition time and that did not deviate much from longer time deposited nanoparticles due to more dendrite structures. Further growth on the nanoparticles was halted because all the incoming Ag^+ ions got deposited on the dendrite structures which led to their fast growth due to longer deposition time and high Ag^+ ion concentration, this was shown by big bunches of dendrite structures.

UNIVERSITY of the WESTERN CAPE

However, densely packed and spherical AgNPs were obtained from 30 seconds deposition time and 20 mM concentration. These nanoparticles had diameters of 114 ± 2 nm and were used as condition for SiNWs synthesis. The presence of Ag on the surface of silicon was also confirmed during EDS measurements.

Silicon nanowires were synthesised with an assistance of AgNPs where these nanoparticles sank on the substrate of Si during the immersion of AgNPs coated samples onto an etching solution composed of HF (5 M), H_2O_2 (0.5 M) and H_2O. Different etching times and oxidant concentrations (H_2O_2) effects on the morphology of SiNWs were investigated. AgNPs were observed lying at the bottom of SiNWs (SiNWs/Si interface) and their appearance was confirmed with EDS measurements. It was observed that the regions covered with Ag were etched and spaces between AgNPs (un-etched areas) were left as SiNWs confirmed from top

view SEM micrographs. Morphology of the nanowires (density and position of individual nanowire) in that way depended mainly on the deposited AgNPs.

The nanowires length was observed to increase with prolonged etching times varied from 30 seconds to 80 minutes. A more linear curve was observed for an increasing nanowires length from about 126 ± 5 nm to over 15 ± 0.2 μm with increased etching time. Growth rate of 206 nm/min was obtained from linear fit of the curve. This increase in length was due to more time allowed for the oxidation-dissolution to take place resulting in longer nanowires during etching. The oxidation-dissolution also depended on the balanced amount of HF and H_2O_2 as these were the two fuels behind the etching mechanism assisted by AgNPs. No trend was observed on the nanowires diameter with changed etching time and diameters were ranging between 50 and 200 nm as measured for different samples also confirmed from few TEM micrographs.

An increase in oxidant concentration showed a similar trend of increasing length for SiNWs but it collapsed when oxidant concentration was increased beyond 1.5 M. This was attributed to an in-balance in the concentration of HF and H_2O_2 because high concentrations of H_2O_2 provided high oxidation rate but the concentration of HF was not enough to satisfy the dissolution required rate and thus nanowires could not grow any longer. SiNWs were not as isolated as they formed big bunches on their bottoms and that was also observed in nanowires obtained after longer etching times. That was probable due to how AgNPs sank into the substrate in which they formed networks at the bottom leaving other regions un-etched due to slow etching rate at bottom than at top.

UNIVERSITY of the
WESTERN CAPE

Longer nanowires tend to form congregated bundles on top which might be due to the movement of AgNPs down the substrate. AgNPs that formed networks sank at once leaving big un-etched regions in between and if those networks split into individual nanoparticles during etching then isolated nanowires would form leaving bundled tips. These congregated bundles were attributed to strong forces due to dangling bonds on the surface of longer nanowires in which these induces mutual attraction between the nanowires. These longer SiNWs were also observed to be porous or rough on their surfaces mostly on the tips and the roughness reduced towards bottom. The roughness was attributed to longer immersion time into an etching solution and that caused new nucleation of AgNPs from diffused Ag^+ ions which led into an etching of nanowire sidewalls.

Individual SiNWs were observed to be single crystalline covered with a thin amorphous SiO_x layer as probed by HR-TEM and visible planes were along ⟨111⟩ direction with d-spacing of 3.41 Å. These nanowires are believed to be growing along the ⟨100⟩ as they are perpendicular to the substrate and the observed planes (111) are not perpendicular to the axial direction of the nanowires in which it would be the case if they were along the growth direction of the SiNWs. The crystallinity was confirmed with XRD and Raman scattering where XRD revealed similar crystallinity as the starting Si wafer with an intense peak of Si (400) related to the orientation of Si (100). Raman scattering also showed a c-Si peak at 520 cm^{-1} a first order phonon crystalline silicon peak and there was a bump observed at 430 cm^{-1} related to amorphous Si and these amorphous features were observed from XRD results. The good crystallinity of these nanowires provide advantage for SiNWs to be applied in Si solar cells as amorphous Si induce high concentration of defect states which leads into high possibility of non-radiative recombination.

Nanowires were mostly passivated with oxygen due to natural oxidation as studied by FTIR with an intense peak from 1000 – 1250 cm^{-1} attributed to asymmetric stretching vibration of Si-O-Si bonds. The shape of the peak showed an enhanced oxidation degree as compared to the bulk wafer due to easy oxidation caused by etched structures. This different degree of oxidation was showed by a second peak at 1200 cm^{-1} for SiNWs in addition to the peak at 1106 cm^{-1} which was observed for bulk Si, the second peak has been observed in SiO_2 glasses. However, the traces of hydrogen termination appeared with a peak at about 665 cm^{-1} attributed to Si-H_2 wagging vibration and was due to pre-synthesis treatment of samples in diluted HF. There is usually an intense peak at about 2100 cm^{-1} for H-terminated samples and that was not observed here confirming that the samples were mostly passivated with oxygen. This oxidation was observed to be high towards the top of nanowires and low in the bottom as shown by the EDS measurements confirming that it was not due to synthesis but natural. It could not be concluded whether the observed amorphous layer covering the crystalline core SiNWs was of SiO_2 or not but the Si-O-Si peak showed it was of SiO_x where x = 1, 2, or 3.

UNIVERSITY of the
WESTERN CAPE

Well reduced light reflections were observed from both specular and diffused reflection measurements for SiNWs compared to their bulk counterparts. Specular reflections of below 10% over the entire visible range of wavelengths were observed for nanowires compared to more than 30% reflection for bulk Si. Specular reflections were observed to decrease with increased nanowires lengths and no results were obtained for SiNWs obtained after 30

minutes of etching (6.4 ± 7 μm length) showing an almost zero light reflection. Diffuse reflection also showed reflections of less than 10% for all SiNWs samples. These reduced reflections are due to elongated one dimensional structure of nanowires resulting into multiple scattering of light during interaction. Graded refractive index which played a role of intermediate medium between air and Si substrate adds to the reduction of light reflection in SiNWs samples. The low light reflections serve as an important property for SiNWs to be applied as antireflective layers for Si solar cells.

Based on the results the recommendations would be to build a solar cell in which I-V curve can be measured and then the efficiency can be calculated. The solar cell would require a doping as to obtain a p-n junction. Instead of some expensive ways of doping via dopant-implantation and dopant-diffusion a cheaper method can be used such as the coating of n-type nanowires with a p-type-like conducting polymer poly(3,4-ethylene-dioxythiophene) : poly-styrene-sulfonate, shortly known as (PEDOT:PSS) to form a p-n junction.

UNIVERSITY of the
WESTERN CAPE

There might be problems in the loss of generated charges due to the natural oxidation of the nanowires and therefore effective ways of surface passivation will be required. Etching of SiNWs into diluted HF as to terminate the dangling bonds with hydrogen is a temporary solution as the SiNWs may oxidise after few days and therefore not an effective solution. A deposition or coating with a thin film might be effective such as thin amorphous layer of silicon nitride thin film.